1-1-2011

The core collapse supernova rate in the sdss-ii supernova survey

Matthew Frederick Taylor
Wayne State University,

THE CORE COLLAPSE SUPERNOVA RATE IN THE SDSS-II SUPERNOVA SURVEY

by

MATTHEW F. TAYLOR

DISSERTATION

Submitted to the Graduate School

of Wayne State University,

Detroit, Michigan

in partial fulfillment of the requirements

for the degree of

DOCTOR OF PHILOSOPHY

2011

MAJOR: Physics

Approved by:

_____

Advisor Date

_____

_____

_____

ACKNOWLEDGEMENTS

In addition to thanking Prof. Cinabro for his steady guidance and near infinite patience, my thanks go to Prof. Sean Gavin, Prof. Ratna Naik, and the WSU Dept. of Physics and Astronomy as a whole for helping me develop as a student, researcher and teacher. I also would like to thank Rick Kessler, Joshua Frieman, Ben Dilday, Masao Sako, and other members of the SDSS-II SN Survey Collaboration for many fruitful discussions and assistance with data analysis.

TABLE OF CONTENTS

Acknowledgments ii

List of Figures v

List of Tables viii

1 Introduction **1**

1.1 Overview 1

1.2 History of Supernova Observation 2

1.3 Observational Characteristics of Supernovae 4

1.4 Current Physical Theory of Supernovae 8

1.5 Star Formation and Stellar Evolution 12

1.6 Motivation for Measuring Core Collapse Rates 15

1.7 Previous Supernova Rate Measurements 16

2 The SDSS-II Supernova Survey **17**

2.1 Astronomical Surveys 17

2.2 A Brief History of SDSS 18

2.3 The SDSS-II Supernova Search Program 20

2.4 SDSS-II Type Ia Supernova Rate Results 23

2.5 BOSS Object Identifications and Redshift Measurements 25

3 Rate Measurement Technique **26**

3.1 Candidate Selection 26

3.2 Phenomenological Light Curve Fitting 30
3.3 Removal of Core Collapse Impostors 36
3.4 Luminosity, Distance and Volume Measurement 44
3.5 Supernova Time and Luminosity 47
3.6 Supernova Detection Efficiency Model 48
3.7 Host Galaxy Extinction Model 53

4 Results **55**

4.1 Supernova Count 55
4.2 Corrections 59
4.3 Sources of Error 61
4.4 Division by Survey Time and Volume 62

5 Conclusion **64**

5.1 Comparison with Prior Measurements 64
5.2 Implications for Star Formation 66
5.3 The CCSN Luminosity Function 68
5.4 Potential for Future Measurements 70

Appendix A: Rate Sample Light Curves **73**

Appendix B: Rate Sample Candidates **85**

Bibliography 89
Abstract 92
Autobiographical Statement 93

LIST OF FIGURES

1.1 Supernova light curves are shown for various supernova types [4] 5

1.2 Supernova spectra are shown for various supernova types [4] 6

1.3 Supernova types are defined by absorption features in their spectra 7

1.4 This mosaic image of the Crab Nebula was taken by HST [8] 9

2.1 The progression of historical astronomical surveys is shown, along with projections for one future survey, LSST. The y coordinate represents the spatial volume over which each survey reliably detected stars or galaxies. 18

2.2 SDSS photometric filter transmission curves are compared to spectra of several celestial objects by L. Girardi et al (2002). [19] 19

2.3 The Hubble Diagram is shown, including the first year of SDSS-II SN data [21]. 22

2.4 The SN Ia Rate from Dilday et al. [23] and previous work is shown. 24

3.1 Stripe 82, the SDSS-II Supernova Survey region, is shaded in red 27

3.2 False color composites of images submitted to human visual scan, including an accepted supernova and some rejected images, are displayed in the SDSS-II scanning guide [28]. 29

3.3 The SDSS-II Supernova Survey data analysis pipeline condenses raw telescope data into supernova candidate light curves. 30

3.4 Model light curve functions are compared when varying a single parameter at a time. 32

3.5 SDSS-II SN candidate light curves are shown for which the light curve model did not converge to a best fit. 34
3.6 SDSS-II SN candidate light curves are shown for which the light curve model did not converge to a best fit. 35
3.7 Flatness score distribution is shown for all candidates, for confirmed supernovae, and for confirmed AGN. 37
3.8 Above are examples of confirmed AGN light curves, with the best model fit plotted in green and the trivial, constant flux fit in blue. All these candidates were excluded by the flatness requirement. 39
3.9 Above are examples of confirmed AGN light curves. All were excluded by the flatness requirement. 40
3.10 Above are examples from the accepted core collapse supernova rate sample. 42
3.11 Above are examples from the accepted core collapse supernova rate sample . 43
3.12 The redshift distribution of the raw CCSN rate sample is shown. 45
3.13 The supernova count is plotted versus limiting apparent magnitude. 50
3.14 The model supernova detection efficiency is shown. 51
3.15 The redshift distribution of the CCSN rate sample is shown, subluminous candidates excluded, before and after the efficiency correction. 52

4.1 Peak time distribution is shown for all candidates within the time and angle constraints discussed in the text. A peak magnitude requirement shows that systematic time bias primarily affects very dim objects. 57
4.2 The peak apparent magnitude distribution, in SDSS r band, is shown for SN candidates excluded from the rate sample for lack of redshift information. . 58

5.1 The CCSN rate measurement from this work is shown with previous CCSN rate measurements in the literature, as given by Horiuchi et al. [40] The solid line is the best fit to $\rho = \rho_0(1+z)^a$, with dashed lines indicating uncertainty. The blue shaded region and nearby points represent the star formation rate estimated primarily from the UV galaxy luminosity data of Baldry et al. [41]. 67

5.2 Historical CCSN rate and star formation rate measurements, from Horiuchi *et al.* [40], are updated with results from this work. 69

5.3 A CCSN luminosity function is derived for the rate sample in this work, plus candidates excluded only because they were faint or too near Earth. 71

LIST OF TABLES

4.1 SNIa Removed from CCSN Rate Sample, by Identification Method, as defined by Sako *et al.* [31] 59

4.2 Candidates Removed from CCSN Rate Sample, by Status and Redshift . . . 60

4.3 Corrections to the CCSN Rate Sample Size, by Reason 60

4.4 Sources of Error in the CCSN Rate 62

4.5 Survey Time Ranges Included in CCSN Rate Measurement 63

5.1 Polynomial Expansion of CCSN Rate vs. Redshift 66

Chapter 1

Introduction

1.1 Overview

I begin this thesis with a brief history of supernova observation, and the gradual accumulation of scientific understanding up to the contemporary state of supernova science. I describe the two major observational classes of supernovae, core collapse and thermonuclear, along with the current physical model for each as a consequence of stellar evolution. From this, I relate the observed rate of core collapse supernova events to star formation, and to other astrophysical phenomena of interest to science. I finish this first section with a summary of core collapse supernova surveys from the literature, highlighting the additional contribution from the present work.

Next, I present an overview of the Sloan Digital Sky Survey, focusing on the second generation of the Sloan survey (SDSS-II) and on the SDSS-II Supernova Survey (SDSS-II SN) collaboration within the overall project. I review major results of SDSS-II SN, including cosmology measurements and thermonuclear (type Ia) supernova rate measurements.

In the third chapter, I describe how core collapse supernova (CCSN) candidates were extracted from the full SDSS-II SN sample. I fit a phenomenological supernova light curve model to the data, per the method developed by the SNLS collaboration [1]. I apply cuts to

remove objects deemed unlikely to be supernovae, and develop an efficiency model to correct for supernovae undetected due to systematic observational constraints.

In the fourth section, I limit the supernova sample to a single volume-limited bin, from redshift 0.03 to 0.09. In this redshift range, I can reliably identify core collapse events by the lack of good fit to type Ia supernova light curve models.

I compare the present results with previous CCSN rate measurements, confirming the trend predicted by the most recent of those studies. I explore conclusions from the combined present and previous work, including cosmic star formation history and the supernova luminosity distribution. Finally, I offer opportunities for future research building on this work.

1.2 History of Supernova Observation

Since ancient times, observers of the heavens have known that most stars are unchanging in brightness and relative position, at least on human time scales. However, there are notable exceptions. Five "wandering stars" visible with the naked eye were named planets, a word derived from the Greek "planes" (to wander), since they appear to wander among the other, fixed stars in cyclic patterns on the sky. Today we know these to be the five nearest planets in our own solar system.

Another exception to the fixed, unchanging nature of the heavens are occasional "guest stars", stars fixed in position relative to the other stars, but appearing where no star was previously observed, then diminishing with time. The earliest recorded guest star is described on Chinese bone engravings dated to 1300 BC, describing a bright new star appearing near Antares [2].

An even brighter new star was observed in 1006 AD, in the southern constellation of Lupus. The Egyptian astronomer Ali b. Ridwan wrote that the object was visibly round in shape and size, appearing more than twice as large as Venus, bright enough to light

the horizon and shine more than a quarter as bright as the moon. References to the 1006 event are also found in other Arab writings of the period, along with Chinese, Japanese and European records. Additional guest stars were recorded in 1054 AD near the constellation of Taurus, and in 1181 AD near the constellation of Cassiopeia.

The first guest star for which we have a reliable, quantitative record occurred in 1572 AD in the constellation of Cassiopeia. This object was made famous by Tycho Brahe in his work "De Stella Nova" (Latin for "On the New Star"); this work popularized the term "stella nova", later shortened to "nova", when referring to new stars. Brahe's precise measurements showed that the nova had no detectable parallax and no proper motion relative to other stars, thus it must lie at a much greater distance than the planets. Brahe's student, Johannes Kepler, reached the same conclusion measuring a second nova in 1604 AD.

Another half-dozen or so novae were recorded by European astronomers in the 17th and 18th century, aided by the invention of the telescope. In the 19th century, the rate of nova discovery greatly increased; more than 30 novae were found between 1840 and 1901 [3]. One such event, Nova Persei 1901, occurred in a nebula of gas and dust, such that the nova's "light echo" could be seen propagating through the nebula. By measuring the echo's angular rate of change as seen from Earth, astronomers deduced that the nova occurred about 500 light years away.

This posed a challenge for the emerging theory of "spiral nebulae" as galaxies beyond the Milky Way. An earlier nova, S Andromedae, was observed in the year 1885, and it was apparently located inside the M31 spiral nebula. If this spiral nebula were a distant galaxy, it would imply that S Andromedae had more than 10,000 times the intrinsic luminosity of other novae like Nova Persei 1901. Of course, later evidence from many sources confirmed that indeed the spiral nebulae are distant galaxies, implying that S Andromedae was an exceptionally bright event, in a separate class from ordinary novae. In 1931, Fritz Zwicky coined the term "super-novae" to refer to these stellar explosions, and by 1938 the hyphen had been dropped. Astronomers have referred to this class of exceptionally bright new stars

as "supernovae" ever since.

1.3 Observational Characteristics of Supernovae

Supernovae are defined by their intense luminosity, which distinguishes them from ordinary novae. Even the brightest novae are more than 600 times less luminous than a typical supernova. A supernova's brightness is usually quantified by its peak magnitude, a logarithmic scale for the energy flux observed from the supernovae at the moment of maximum luminosity. Magnitude is formally defined as:

$$m = -2.5 log_{10}(\frac{F}{F_0}) \tag{1.1}$$

where F is the object's observed flux in Janskys ($1\text{Jy} = 10^{-26}\text{W}/(\text{m}^2\text{Hz})$), F_0 is the flux of a reference star (usually Vega) in the same units, and m is the resulting magnitude. Note that brighter objects have lower magnitude, somewhat contrary to intuition.

Supernovae are also rather infrequent, occurring in a galaxy about once per 100 years, on average. In our own Milky Way galaxy, it is believed that the bright "guest stars" of 1300 BC, 1066 AD, 1054 AD and 1181 AD were all supernovae, along with the "stella nova" studied by Brahe and Kepler. Unfortunately for modern astronomers, no supernova has been observed in our galaxy since the 17th century, though some may have occurred in regions of our galaxy obscured from Earth by interstellar dust.

A supernova's observable characteristics can be summarized by two functions, its spectrum and its light curve. The spectrum shows the intensity of supernova light as a function of wavelength, and can reveal elements present in the supernova according to their spectral emission and absorption lines. The light curve shows the intensity of supernova light as a function of time, and is usually limited to the light passing through a particular transmission filter. In general, a supernova's spectrum is more difficult to obtain than its light curve, because spectroscopy requires a stronger photon flux than mere imaging, to produce definitive

measurements. Figures 1.1 and 1.2 show a collection of typical light curves and spectra for supernovae of various types.

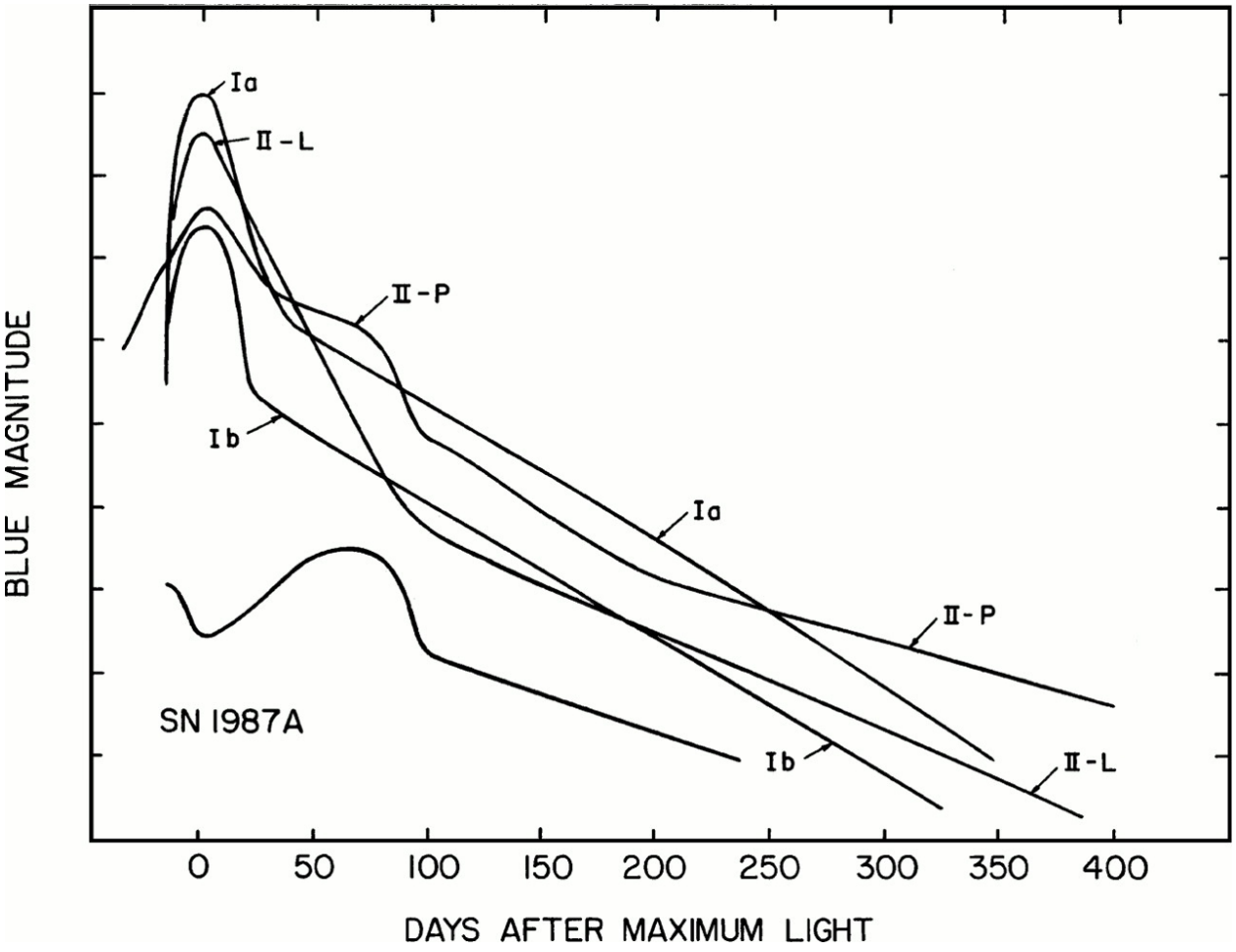

Figure 1.1: Supernova light curves are shown for various supernova types [4]

Soon after supernovae were recognized as a distinct phenomenon, astronomers noticed that there were two primary supernova types. The first type, designated type I, tend to be brighter and less frequent, and can be observed growing brighter over a few days, before gradually dimming. The second type, designated type II, is dimmer and more frequent, and tends to appear suddenly at its peak brightness. Type II supernovae are also identified with hydrogen emission lines in their spectra near peak brightness, which is not present in the spectra of type I supernovae.

Among the type I supernovae, spectroscopy can further distinguish three subtypes. Type

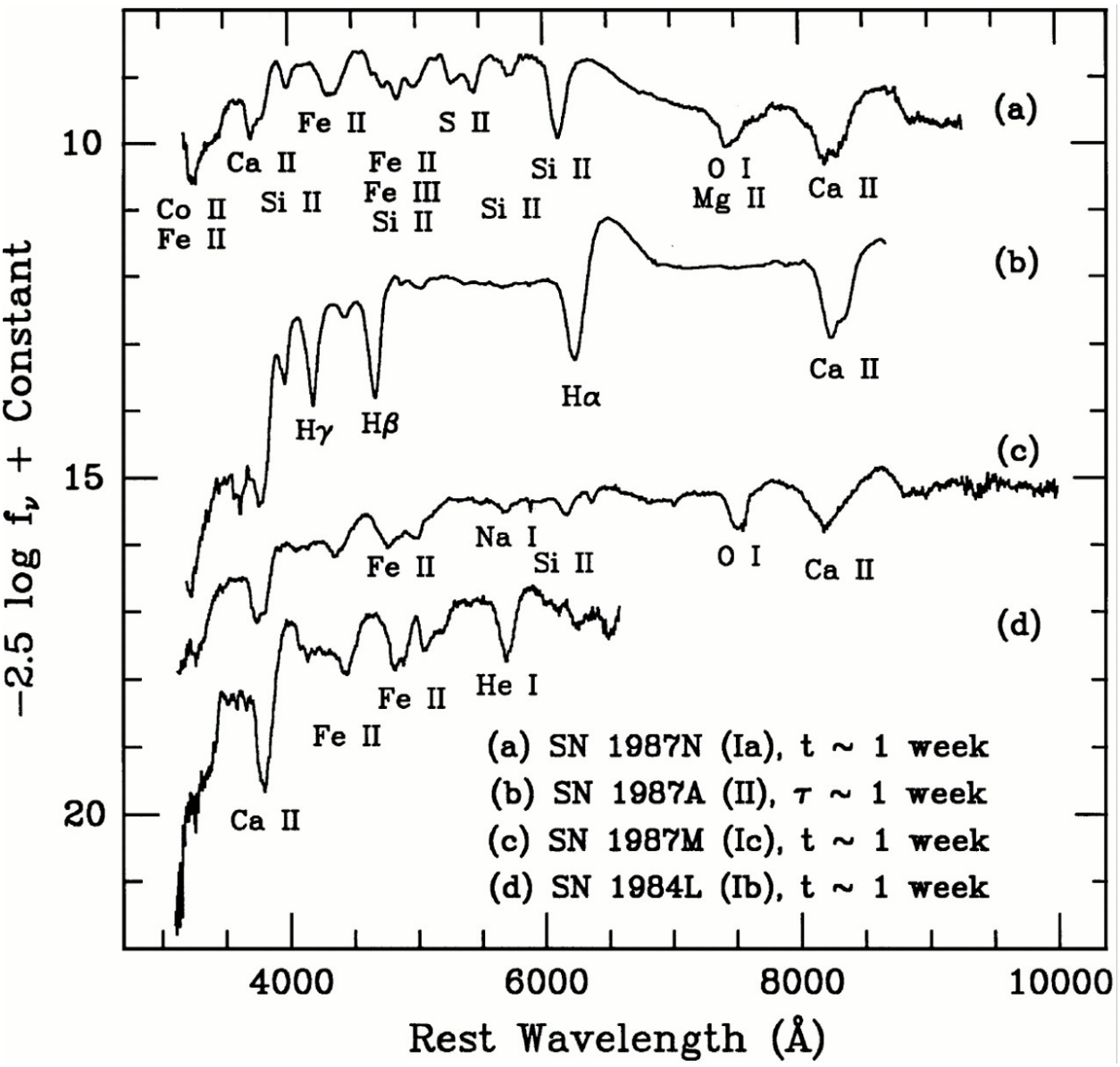

Figure 1.2: Supernova spectra are shown for various supernova types [4]

Ia supernovae show a strong absorption line at $\lambda = 615.0$nm near peak luminosity, corresponding to singly ionized silicon (Si II). Type Ib show no silicon absorption, but do exhibit a neutral helium absorption line at $\lambda = 587.6$nm. The remainder, showing neither silicon nor helium absorption lines, are identified as type Ic.

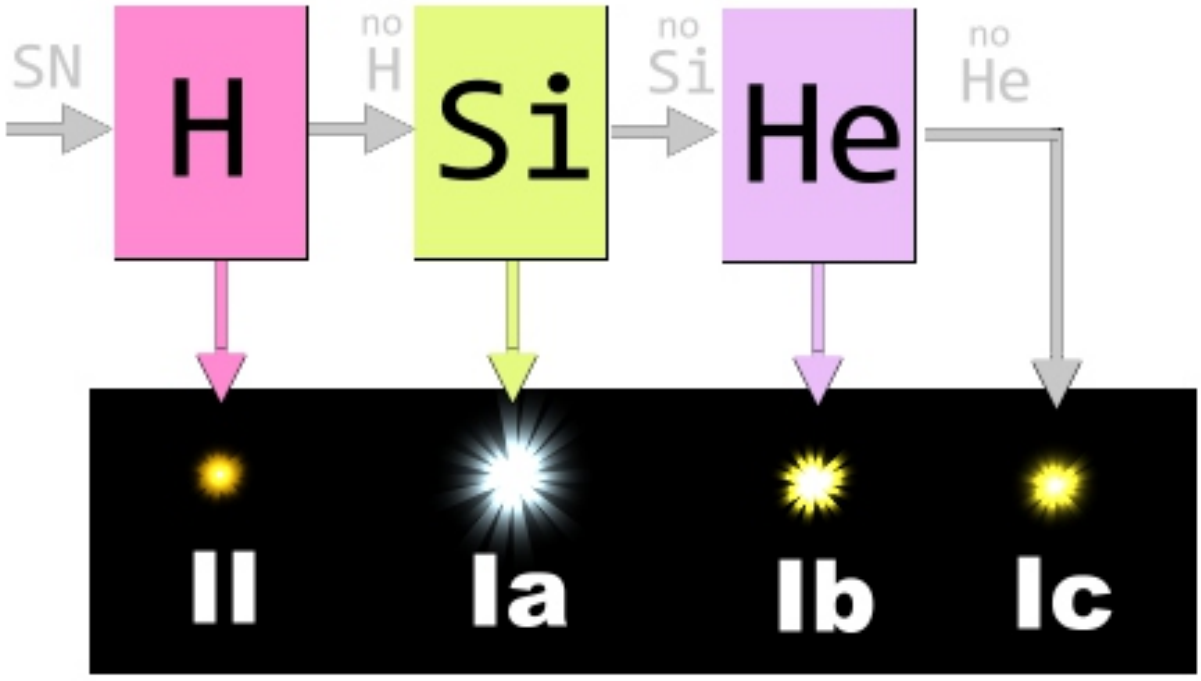

Figure 1.3: Supernova types are defined by absorption features in their spectra

Type II supernovae have been further classified as well. The most common subtypes are II-P, characterized by a plateau of roughly constant brightness in the light curve just after peak, and II-L, which lacks a plateau and whose magnitude decays linearly with time. More exotic subtypes include IIn, with exceptionally narrow absorption lines in their spectra, and IIb, an apparent hybrid of type II and type Ib attributes. A number of unique type II

supernovae defy any of these classification schemes, and are simply called "type II peculiar", abbreviated "IIpec".

A third class of supernovae has been proposed to include a handful of objects such as SN2002bj that do not fit well into either type I or type II [5]. These dim supernovae, dubbed "type .Ia", have spectra similar to type IIn but evolve much more quickly than either type I or type II supernovae. Since these events are relatively rare, more observation will be required to better understand them.

1.4 Current Physical Theory of Supernovae

The current consensus is that the observational supernova classes derive from two distinct physical events. Type Ia corresponds to thermonuclear supernovae, thought to occur when a white dwarf star acquires sufficient mass from a companion star to exceed the Chandrasekhar mass. The other supernova types (II, Ib and Ic) are core collapse supernovae, when the core of a massive star makes a sudden transition to neutron star density, causing an explosive rebound shock that tears apart the star's outer layers. [6]

The physical nature of supernovae is perhaps best elucidated by the "guest star" of 1054 C.E., and the clues it has left behind. Chinese and Arab records of the event were precise enough that its position can be located in the constellation of Taurus, and observed through modern telescopes. There we find two remarkable objects, the Crab Nebula and the Crab Pulsar.

The Crab Nebula is a great cloud of gas, approximately 11 light years across. Time series images of the nebula reveal that it is expanding at about 1500 kilometers per second; extrapolating this expansion backward in time, we conclude that the nebula began expanding from a compact, central region in the mid-11th century. Due to the strong coincidence in time and position, it appears, therefore, that the Crab Nebula is a remnant of the event observed on Earth in 1054 AD.

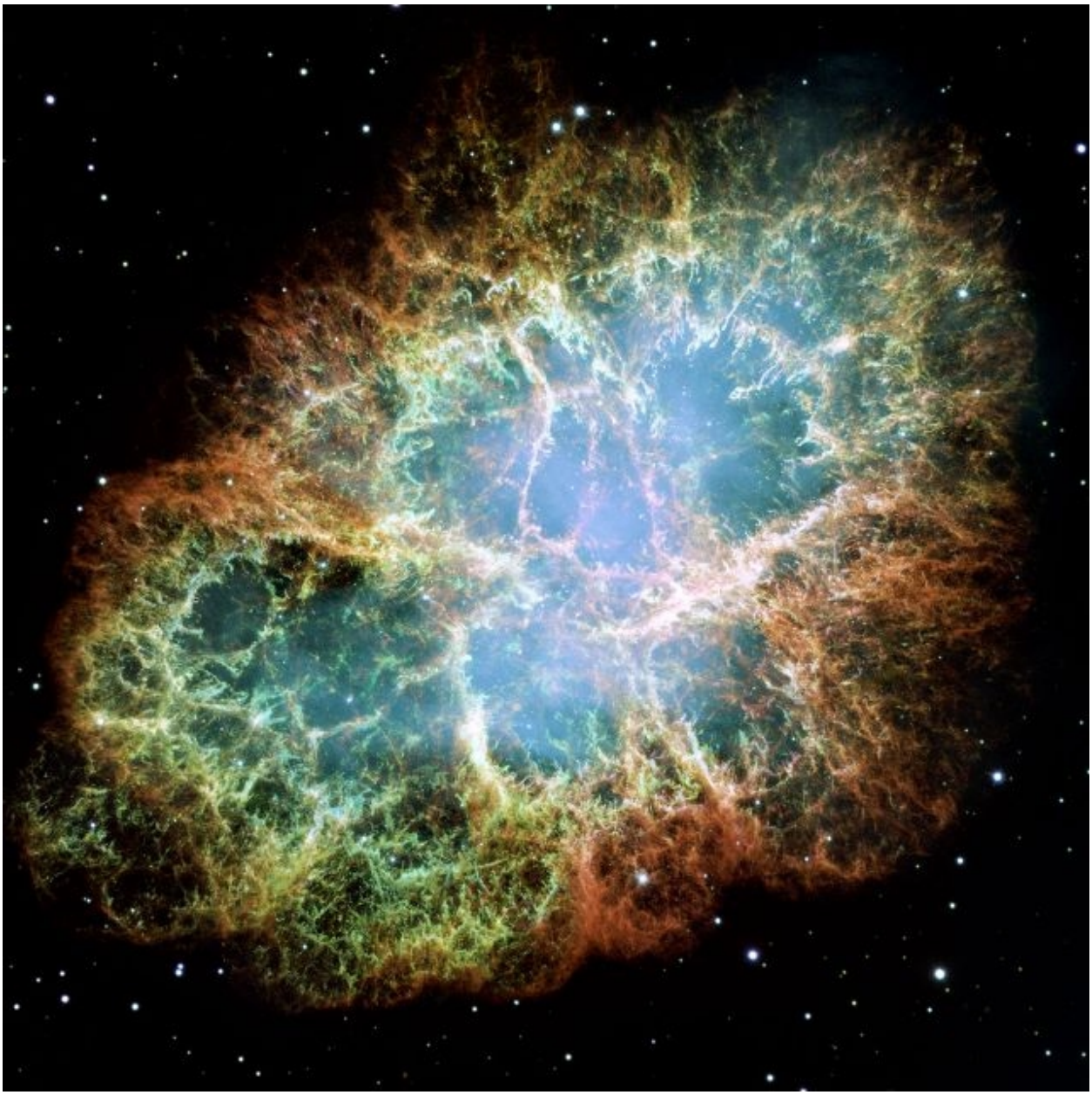

Figure 1.4: This mosaic image of the Crab Nebula was taken by HST [8]

Because the Crab Nebula is expanding in all directions, we infer that its speed of lateral expansion is equal to its rate of radial expansion, measurable by the blue shift of spectral lines. Dividing the nebula's observed angular rate of expansion into the inferred actual speed of expansion, the distance from Earth to the Crab Nebula can be calculated as about 6500 light years. To produce the bright light source described in historical records at such a great distance, the 1054 AD event must have been a supernova.

The Crab Pulsar, discovered in 1965 [9], is a compact object located at the origin of the Crab Nebula's expansion. It is an optical pulsar, pulsating once every 33 milliseconds, and also emits radiation at wavelengths ranging from radio to gamma rays. The pulsar is particularly bright in x-ray wavelengths. The very rapid changes in the pulsar's luminosity require that it must be very compact, since light can only traverse about 10,000 kilometers in one pulsation period, the source can be no larger.

Some thirty years before the Crab Pulsar's discovery, a theory of stellar collapse was proposed, predicting that massive stars would end their lives in supernovae [10]. According to the theory, after a star has exhausted most of its hydrogen fuel, it lacks the heat and radiation pressure to support its weight against gravitational collapse. For stars of ordinary mass, the collapse is halted by the pressure of electron degeneracy, resulting in a white dwarf star.

However, in more massive stars, electron degeneracy pressure is not strong enough to resist gravity; electrons are under such intense gravitational pressure that they recombine with protons to form neutrons, the inverse of nuclear beta decay. Removal of electrons due to recombination lets the stellar core contract further, accelerating the recombination process in a runaway chain reaction. In a matter of seconds, all the core's electrons are consumed, and the remaining core nucleons collapse in near free fall, followed by the outer layers of the star.

The collapse continues until the stellar core approaches the density of nuclear matter, at which time neutron degeneracy pressure becomes the dominant force. Once the core collapse

is halted, infalling matter from the outer layers of the star strikes the core and rebounds, creating an outward shock wave of enormous energy. This rebound shock propagates outward, accelerating nearly all the mass of the star to escape velocity, leaving only the bare, neutron core [10]. The energetic shockwave, and the radiation it produces, appear as a supernova to distant observers.

The core collapse theory accounts for many features of the Crab Nebula. The initial explosion corresponds to the supernova observed in 1054 AD, and the nebula is the expanding remnant of the expelled outer layers of the star. The Crab Pulsar is then explained as the remaining neutron star, pulsing due to its extremely rapid rotation. Such rapid rotation is expected when a stellar core of typical angular momentum contracts to an object only a few kilometers across.

Since the Crab Pulsar's discovery, many other pulsars have been identified, many surrounded by expanding, gaseous nebulae. The core collapse theory of supernovae is well supported by evidence, though it does not fit well with one particular class of supernovae, those of type Ia (SNIa). First, no pulsar is found in the remnant of any SNIa. Second, some SNIa occur in galaxies which have had little to no star formation activity for billions of years. Because massive stars have short lifetimes, around 50 million years or less, the core collapse theory cannot explain why so many SNIa are observed in galaxies where star formation is long dormant.

The leading theory explaining type Ia supernova is the accretion of matter onto a white dwarf from a nearby companion star. As more mass accumulates on the white dwarf, its gravitational pressure eventually exceeds the electron degeneracy pressure. The white dwarf collapses, raising its internal temperature and density enough to ignite nuclear fusion of carbon and heavier elements. The heat released further increases the temperature and accelerates fusion, resulting in an explosive, runaway nuclear burning of the entire star. The burning of carbon and oxygen produces a large quantity of unstable ^{56}Ni, the subsequent radioactive decay of which governs the supernova's declining luminosity. [11].

1.5 Star Formation and Stellar Evolution

The bulk of star formation is thought to occur in cold molecular clouds, collections of interstellar gas and dust light years across, ranging from only a few solar masses to millions of solar masses. They are called molecular clouds because much of their hydrogen is bound up in H_2 molecules. Many such clouds have been observed in the Milky Way, and in other nearby galaxies, often with newly formed and still-forming stars embedded within.

The processes by which molecular clouds form, and by which stars nucleate within the clouds, are not well understood. A number of competing star formation theories have been formulated, however more data is required to test them. In particular, the stellar initial mass function (IMF) is of key importance. The IMF specifies the probability density of initial stellar masses; it is well measured for stars of ordinary mass, but not for stars of exceptionally high or low mass. Low mass stars are very faint, whereas high mass stars have very short lifetimes. Star surveys, therefore, tend to have very low statistics in both categories, confounding attempts to accurately measure the IMF at either extreme.

Stellar evolution is better understood than star formation, and is well modeled by relatively simple numerical simulations. Once a star has become sufficiently compact due to self-gravity, hydrogen fusion ignites and the star rapidly moves to the main sequence, a regime in which the star's mass almost completely determines its temperature, luminosity and internal structure. Most stars visible in the sky are in the main sequence phase of their life, and their mass can be reliably inferred from the color of starlight we observe.

Low mass stars have relatively low core temperature and density, and therefore burn their hydrogen fuel very slowly. Stars with mass less than about 0.87 $M_\odot$ burn hydrogen so slowly that none have had time to exhaust their core hydrogen supply within the current age of the universe.

More massive stars exhaust their core hydrogen more rapidly, so that their main sequence lifetime is approximately as follows [6]:

$$\tau_{ms} = (\frac{M}{M_\odot})^{-2.5} \times 10^{10} yr \tag{1.2}$$

Once a star's core hydrogen is exhausted, it enters a period of instability powered by fusion of helium and heavier elements, and by hydrogen outside the core. Stars in this phase undergo drastic changes in their equilibrium size, including the giant and supergiant stellar classes, and can undergo pulsations in which a large fraction of the stellar envelope is ejected into space. For stars of approximately $8M_\odot$ and lower, these convulsions continue until the star has ejected and/or burned enough matter that nuclear fusion cannot be sustained, neither for hydrogen nor heavier elements. In the absence of fusion-generated heat and radiation pressure, the star collapses under gravity to extreme density. The collapse is finally halted by electron degeneracy pressure, when it becomes so dense that all the electron quantum states in its gravitational potential well are occupied. These extremely compact and hot stellar remnants are known as white dwarfs.

Stars with initial mass more than approximately $8M_\odot$ have a different fate. Even after ejecting much of its mass in the later phases of life, the steller core is able to sustain fusion of helium and heavier elements. The star first burns the carbon produced by helium fusion to make oxygen, then burns the oxygen to make silicon, and finally burns the silicon to make iron.

The formation of iron represents an end point in the thermonuclear synthesis of elements. When two nuclei fuse to form an element lighter than iron, the binding energy of the system increases, due to the attractive nuclear strong force between nucleons. According to the liquid drop model of the nucleus, the fused nucleus has high binding energy because it has less total surface area than the original two nuclei, analogous to surface tension in classical liquids [7].

For larger nuclei, the coulomb repulsion of nuclear protons must be taken into account, reducing the nuclear binding energy by a term proportional to Z^2, where Z is the atomic number. At $Z = 26$ (iron), the coulomb term in the nuclear binding energy overwhelms the

surface area contribution given by the liquid drop model, so the fusion of iron with other nuclei does not increase nuclear binding energy [7]. Thus when iron accumulates in the innermost regions of the core, it is unable to burn, *i.e.* it cannot undergo any exothermic nuclear reaction either through fusion or fission.

If gravitational pressure is sufficient, however, the iron core does become susceptible to an endothermic nuclear reaction, the recombination of electrons and protons to form neutrons, producing neutrinos as a byproduct. Once this reaction begins, the consumption of electrons begins reducing the degeneracy pressure that supports the star. This allows the star to contract, increasing gravitational pressure in the core and accelerating the recombination process. The result is a runaway reaction, consuming all available electrons in the course of a few seconds. The sudden recombination of electrons and protons produces a concentrated burst of neutrinos; a core collapse supernova is actually more luminous in neutrinos than in photons, though of course the neutrino radiation is far more difficult to detect. Hence core collapse supernovae are less optically luminous than thermonuclear supernovae, even though the total energy emitted is comparable for both supernova types.

The remaining core, now consisting entirely of neutrons, collapses under gravity until halted by neutron degeneracy pressure, at which point it has reached the density of an atomic nucleus. The surrounding stellar material first falls inward, then rebounds from the neutron core when the collapse is halting, resulting in an outward propagating shock wave. Once the shock breaks the visible surface of the star, a core collapse supernova has begun. Over the course of the next few weeks, the expanding stellar envelope expands, first becoming orders of magnitude brighter than the progenitor star, then gradually dimming as the ejecta cools to interstellar temperatures.

1.6 Motivation for Measuring Core Collapse Rates

CCSN progenitors, stars massive enough to produce core collapse supernovae, have very brief lives on astronomical time scales. At the lower bound of CCSN progenitor mass, $8 \pm 1 M_{\odot}$, the star's expected main sequence lifetime is 55^{+22}_{-14}Myr; more massive stars will have even shorter lifetimes. Therefore, if we observe light from a core collapse supernova in some past era of cosmic history, we know that its progenitor star formed within the preceding 55 million years or thereabouts. The bulk of the SDSS-II CCSN sample are observed at redshifts near ($z \approx 0.1$), where we see events that occurred about 1.4Gyr ago. Thus if we use CCSN events as tracers of massive star formation, the time of core collapse lags the time of star formation by less than 4%. By measuring the CCSN volumetric rate as a function of time, we probe the star formation history of the universe.

Measuring the CCSN rate history of the universe is also useful to other measurements where CCSN act as a background, contaminating the primary signal under study. Cosmology studies based on type Ia supernovae are in this category; some CCSN have light curves superficially similar to SNIa, but do not obey the SNIa stretch-luminosity relation. A CCSN rate measurement provides a quantitative basis for estimating the uncertainty in SNIa cosmology results due to CCSN contamination. Neutrinos produced by CCSN also may contaminate experiments searching for neutrinos from other sources, such as primordial cosmic neutrinos. A more accurate CCSN rate measurement allows better subtraction of the CCSN neutrino background.

The CCSN rate may also be compared to other star formation indicators, to better understand differences between CCSN progenitor stars and the general stellar population. Furthermore, a comparison of the CCSN rate to the overall star formation rate could reveal more precisely the mass threshold between CCSN progenitors and white dwarf progenitors, if the stellar initial mass function can be measured accurately by other means.

1.7 Previous Supernova Rate Measurements

Perhaps the earliest publication that could be considered a modern CCSN rate measurement is the 1999 work of Cappellaro *et al.* [12], in which a number of amateur and professional surveys were pooled to form a sample of relatively nearby supernovae. In its day this was a landmark result, well ahead of any previous SN rate measurement. However, because it relied on a heterogeneous pool of observing programs, questions remain about the survey time and volume over which the CCSN sample was divided, and as to whether systematic uncertainties were correctly estimated.

By 2005, the study of supernova populations was advanced by the completion of deliberate supernova surveys with well defined, consistent observational limits. The Great Observatories Origins Deep Survey (GOODS) used the Hubble Space Telescope to survey high redshift galaxies, whereas the Two Micron All Sky Survey (2MASS) used ground based telescopes to view objects at a range of redshifts. The CCSN rate was extracted from each by Dahlen *et al.* [13] and Cappellaro *et al.* [14] respectively, providing improved statistics, well defined survey constraints and a better understanding of systematic errors than previous work.

The current generation of supernova surveys, motivated primarily by interest in cosmology, greatly increased the accuracy and time resolution for supernova observation. SDSS-II SN is part of this cohort, along with the Supernova Legacy Survey (SNLS) and Southern intermediate redshift ESO Supernova Search (STRESS). SDSS-II SN and SNLS were designed primarily to measure SNIa candidates for cosmology, but incidentally detected a large, well characterized sample of CCSN. STRESS, on the other hand, was explicitly designed as a supernova rate survey for both SNIa and CCSN, though it did not quite have the same commitment of observational resources as SNLS and SDSS-II SN. The SNLS analysis of Bazin *et al.* [1] and the STRESS analysis of Botticella et al [15] provide further improvements to the CCSN rate measurement project. The present work will complete the CCSN rate results for the current generation of surveys.

Chapter 2

The SDSS-II Supernova Survey

2.1 Astronomical Surveys

Traditionally, astronomical observations have tended to focus on individual targets, such as a specific planet, star or galaxy. This is a sensible strategy, given that telescope time has historically been scarce and that objects of interest occupy a tiny fraction of the sky's total observable area. This mode of observation still has great value, and will continue to be practiced for the foreseeable future.

However, in recent times a second mode of observation has become viable, where large regions of the sky are surveyed at once, capturing many object images simultaneously. Astronomical surveys of this kind have been made possible by digital imaging technology. Because the telescope images are represented electronically, it is possible to store and catalog a vast database of images, even when the angular density of interesting objects is low. Also, electronic processing can compensate for the rotation of the Earth so that the telescope need not track the apparent motion of the stars across the sky, a technique known as drift scan imaging.

With the use of drift scan imaging and digital image processing, large sky surveys can now be conducted at a reasonable cost, and the volume of astronomical survey data generated is

increasing exponentially by the year. Figure 2.1 shows the production rate of astronomical image data for a number of survey telescopes, versus the year of commissioning.

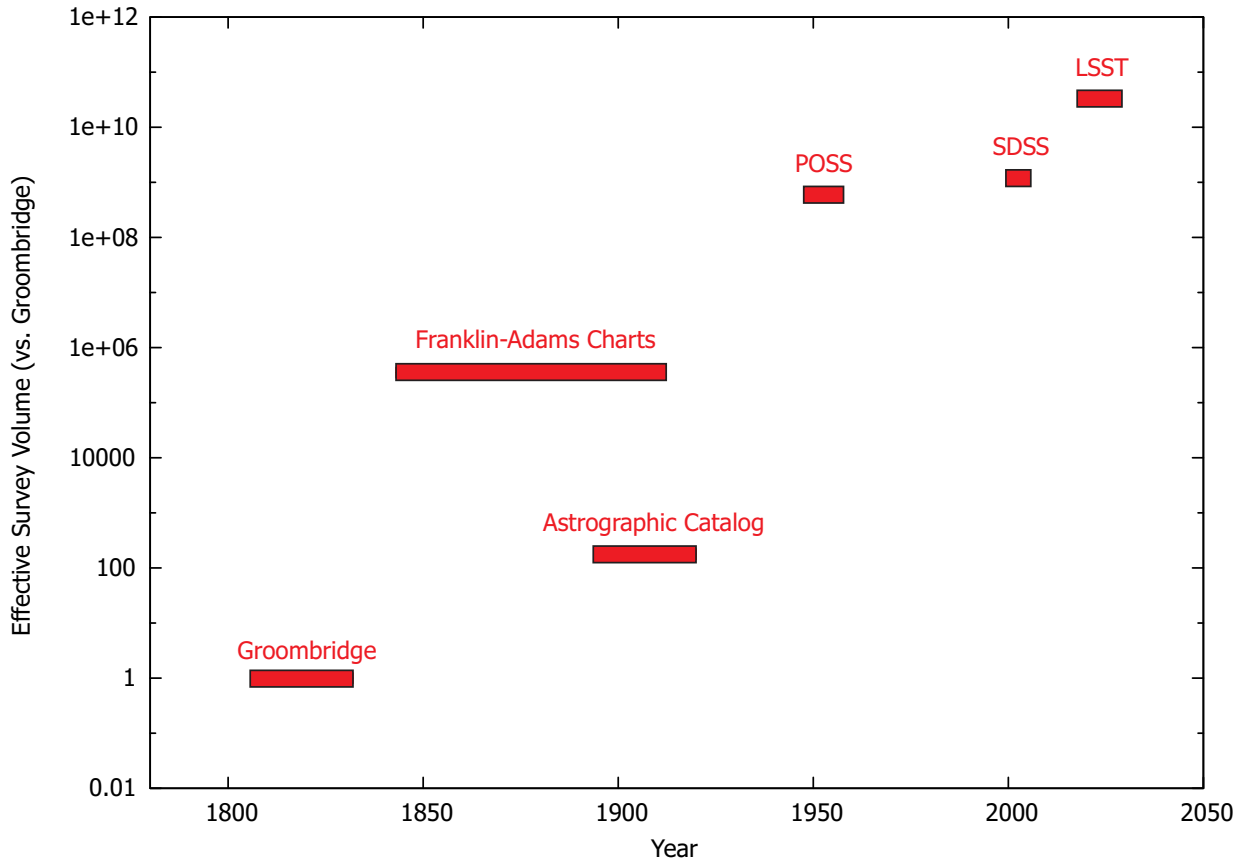

Figure 2.1: The progression of historical astronomical surveys is shown, along with projections for one future survey, LSST. The y coordinate represents the spatial volume over which each survey reliably detected stars or galaxies.

2.2 A Brief History of SDSS

The original Sloan Digital Sky Survey (SDSS) was designed as a broad survey of approximately one fourth of the visible sky. The primary 2.5 meter telescope, commissioned in 2000 and still in operation, is located at Apache Point Observatory, New Mexico. It is notable for its very wide field of view, covering eight times as much sky as the full moon in one image. [16]

The SDSS telescope uses a large-format, 120-megapixel mosaic CCD camera to capture five images simultaneously, each in a separate optical band [17]. The five optical bands imaged by SDSS comprise the 'SDSS filter system', which has since been adopted by a number of other observatories. Figure 2.2 shows the transmission curve of the filters used to image each band, labeled u, g, r, i and z. In addition, two digital spectrographs can be trained on specific objects identified in images from the primary telescope. [18]

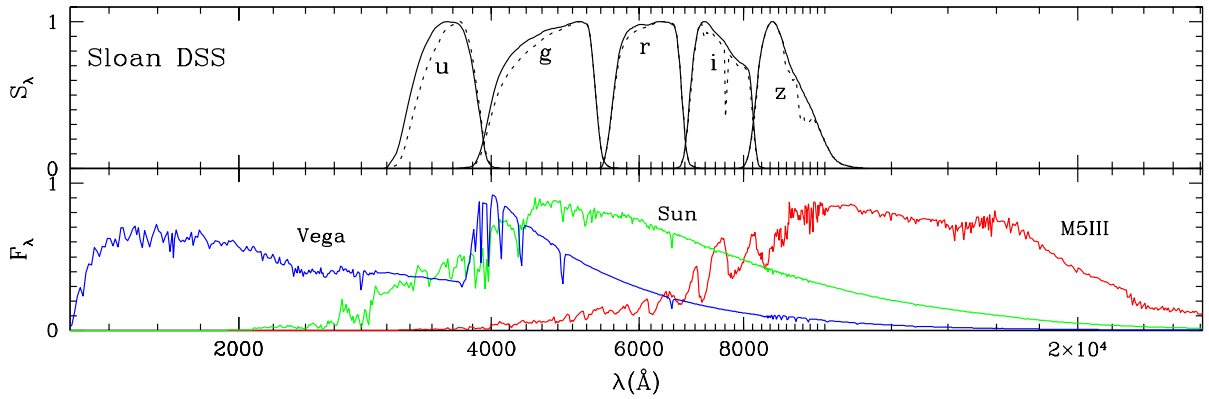

Figure 2.2: SDSS photometric filter transmission curves are compared to spectra of several celestial objects by L. Girardi et al (2002). [19]

The second Sloan Survey, known as SDSS-II, reused the original SDSS telescope and infrastructure to conduct three specific astronomical search programs. First, the Sloan Legacy Survey (SLS) was a direct extension of the original SDSS search goals, and completed the final SDSS dataset of 230 million celestial objects. Second, the Sloan Extension for Galactic Understanding and Exploration (SEGUE) was designed to study the structure and history of our own galaxy, imaging 3500 deg^2 of sky and capturing 240,000 stellar spectra. The third search program was the Sloan Supernova Survey (SDSS-II SN), which provided the primary data set for this work.

A third generation of the Sloan Survey, SDSS-III, is underway as I write this thesis. Scheduled to run from 2008-2014, SDSS-III includes four surveys. The APO Galactic Evolu-

tion Experiment (APOGEE) and SEGUE-2 both focus on the Milky Way galaxy, precisely measuring the motion and composition of nearly half a million stars. The Multi-Object APO Radial Velocity Exoplanet Large-area Survey (MARVELS) tracks the radial motion of 11,000 bright stars, measuring them frequently and precisely enough to detect large planets over a broad range of orbital periods. Finally, the Baryon Oscillation Spectroscopic Survey (BOSS) is obtaining spectroscopic redshifts for over 1.5 million galaxies, one of the most accurate measurements to date of the Universe's large scale structure. Although SDSS-III does not include a dedicated supernova search, BOSS is observing many galaxies that hosted SDSS-II supernova candidates, including a list of suspected host galaxies provided by the SDSS-II SN Survey team. That data has also contributed to this work.

2.3 The SDSS-II Supernova Search Program

The SDSS-II SN Survey was designed primarily as a search for type Ia Supernovae (SN Ia), which are desirable because they can be used as standard candles for cosmology [20]. According to the current consensus model, each SNIa detonates when it has accumulated sufficient mass from a companion star to exceed the Chandrasekhar limit of 1.46 solar masses [6]. Because all SNIa detonate at nearly the same mass, the luminosity of their explosions is nearly uniform. Therefore the supernova's observed brightness informs us of its distance from Earth, independently of its Hubble red shift.

In practice, SNIa explosions are not as uniform as astronomers would like. For one, the elemental composition of SNIa progenitors can affect the luminosity of their explosions. Fortunately, it is possible to independently estimate a supernova's intrinsic brightness via the width of its light curve peak. SNIa with higher intrinsic luminosity tend also to evolve more slowly in time, a trend known as the stretch-luminosity relation.

Dust in the supernova's host galaxy can also complicate its use as a standard candle, a phenomenon known as extinction. Interstellar dust particles scatter light at all wavelengths,

but scatter short, blue wavelengths most strongly. The effect is to reduce the supernova's apparent brightness, and to redden its apparent color.

The SDSS-II SN Survey, like other modern supernova studies, attacks problems of intrinsic luminosity variation and extinction with a detailed empirical model known as MLCS[21]. MLCS uses a multi-parameter warp to fit a candidate to a set of canonical SNIa templates, finding the best fit distance modulus, extinction parameter (A_V) and SNIa stretch parameter (Δ). For most SNIa, MLCS has been shown to converge on results that match spectroscopic confirmation with high confidence.

A second light curve program, SALT2 [22], was also applied to SDSS-II supernova light curves, to assess the systematic effect of the fitting program itself on cosmology results. SALT2 employs a similar, template-based approach to MLCS, but with the additional constraint that it minimizes the scatter of data points on the Hubble diagram. The initial analysis, using only 2005 data, uncovered significant systematic differences in cosmology results between MLCS and SALT2. However, work continues to reconcile the two models through further analysis using the full three years of SDSS-II SN data. [21].

Prior to SDSS-II, supernova surveys for cosmology had concentrated on two extremes, either wide angle surveys focusing on nearby galaxies, or deep, narrow surveys focusing on the most distant galaxies. The intermediate region, from about $z = 0.1$ to 0.3, had sparse SNIa data. The SDSS-II SN survey was specifically designed to study this redshift desert', and was quite successful in doing so. Figure 2.3 shows the Hubble diagram, a logarithmic plot of distance versus redshift, combining SDSS-II SN data with other surveys.

Unlike most galaxies, supernovae change rapidly, with significant changes in brightness on the scale of weeks or even days. Therefore, to properly observe supernovae requires a shorter cadence, the time between images of the same sky region, compared to a galaxy survey. For the SDSS-II SN Survey, a 300 $\deg^2$ region of sky, designated 'Stripe 82', was targeted for imaging once every two days; however, viewing conditions only allowed imaging of the entire stripe once every four days, on average.

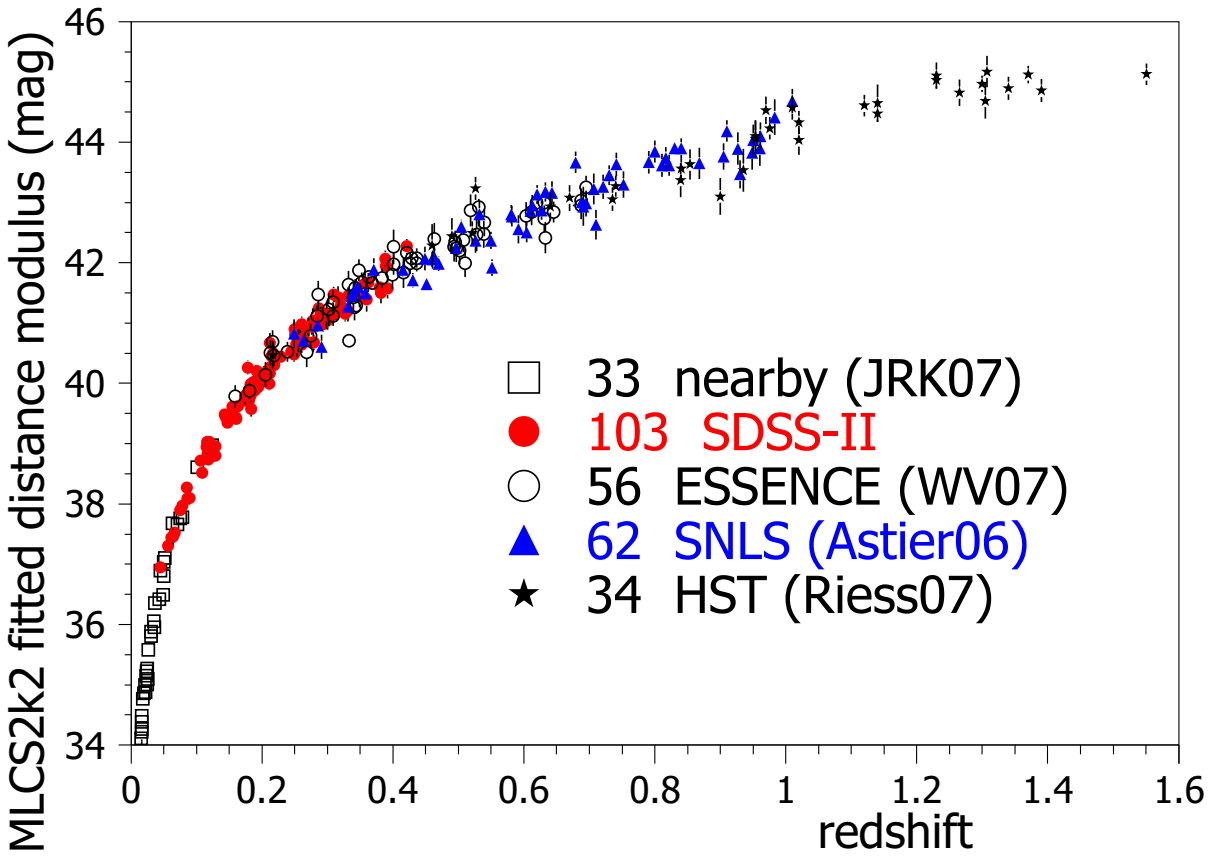

Figure 2.3: The Hubble Diagram is shown, including the first year of SDSS-II SN data [21].

To detect supernovae within the search region, images from each night were first compared to a template image of the same region of the sky. Any part of the image differing significantly from the template was selected for further analysis, as it might indicate a distant object whose brightness is variable on a time scale of days. To reduce the volume of data processed, a catalog of known quasars, variable stars and active galactic nuclei (AGNs) was used to exclude variable objects that are known not to be supernovae. Also, most objects within the solar system are rejected by software; their proper motion is so rapid that their position shifts significantly in the few minutes between *g, r* and *i* camera exposures.

The remaining variable objects were forwarded to a team of human scanners within the collaboration. Images of each object were presented to one or more scanners, who registered their judgment on whether the object might be a supernova. Many objects that show image differences from night to night are not supernovae, such as asteroids, bright stars and telescope artifacts. Also, when a variable object was detected in more than one year of observation, it was excluded from the sample, as supernovae are very unlikely to be active over such a long period of time. As the survey progressed, exclusion of these non-supernovae became increasingly automated, so that a greater fraction of objects forwarded to human scanners were subsequently identified as possible supernovae.

2.4 SDSS-II Type Ia Supernova Rate Results

As the SDSS-II SN survey was designed to detect and measure SNe Ia very accurately, it produced an excellent sample for measuring the rate at which SNe Ia occur in space. Analysis of the SDSS-II SN data by Dilday *et al.* [23] identified a rate sample of over 500 SN Ia candidates, approximately half of which were spectroscopically confirmed. The remainder were typed by a template fitting algorithm, shown in Monte Carlo simulations to add only about 5 percent uncertainty to the rate measurement due to false positives.

Figure 2.4, from Dilday *et al.*, shows the SN Ia rate binned by red shift up to $z \approx 0.3$.

Previous SN Ia rate results are superimposed on the plot.

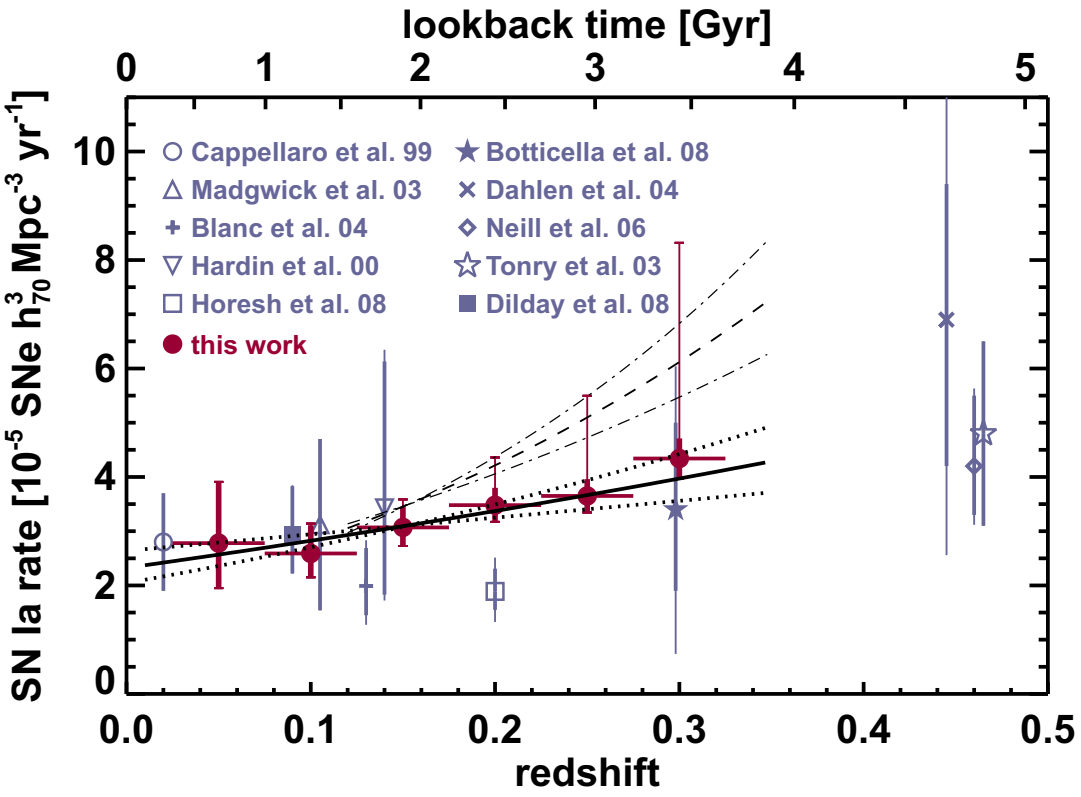

Figure 2.4: The SN Ia Rate from Dilday et al. [23] and previous work is shown.

For the core collapse supernova (CCSN) rate measurement presented in this thesis, I build on the result of Dilday *et al.*. In general, CCSN are much more diverse than SNe Ia, and therefore tools to identify CCSN candidates from photometry alone are not as well developed as for SNe Ia. However, we can make use of the current consensus view that SNe Ia and CCSN together comprise nearly the entire set of observed supernovae. Thus I am able to count the CCSN rate by first counting the supernova rate for all types, then subtracting the accurately measured SN Ia rate found by Dilday. The possibility of exotic supernova types that are neither CCSN nor SN Ia does exist, but their numbers as a fraction of all supernovae detected to date is miniscule. Uncertainty in the rate due to exotic supernovae

is negligible compared to other sources of error.

2.5 BOSS Object Identifications and Redshift Measurements

At the beginning of the SDSS-III BOSS project, the SDSS-II Supernova Survey team compiled a list of suggested targets for BOSS. The suggested targets were a complete list of galaxies matching two criteria: that the galaxy is nearest to a supernova candidate in angular distance, and also nearest in isophotal distance. Isophotal distance measures the candidate's distance from the galaxy center, as a fraction of the galaxy's size along the galaxy-candidate axis. When a galaxy is nearest to a candidate in both angular and isophotal distance, confidence is high that it is the galaxy in which the supernova candidate actually occurred. [21]

Fortunately for this work, the BOSS collaboration scheduled the recommended SDSS-II targets very early in their observation plan. Many of the recommended targets could not be observed due to technical and observational constraints; however, BOSS was still able to collect spectra for 2,458 targets. BOSS discovered that some of the targets were variable stars or quasars, which likely means that the variable light source observed by SDSS-II was not a supernova at all. For the remainder, which appear to be typical, inactive galaxies, the BOSS team measured redshifts using the spectrum analysis pipeline already developed for their primary mission. [24]

Chapter 3

Rate Measurement Technique

3.1 Candidate Selection

The data analysis pipeline described in this section is not specific to my core collapse rate measurement; it was designed to identify supernovae in general, and the set of supernova candidates it generated has been used by all supernova-related work by the SDSS-II collaboration. Technical details of the pipeline, summarized below, are covered in the published SDSS-II Supernova Survey Technical Summary [20].

The SDSS-II SN data analysis pipeline is designed to identify supernova candidates among the sequence of images of "stripe 82", the survey's designated region of sky. The full region surveyed extends from right ascension (RA) $-60°$ to $+60°$, and from declination $-1.25°$ to $+1.25°$. It is a narrow strip of sky along the celestial equator, primarily located in the constellations of Aquarius, Pisces and Cetus, with minor portions in Aquila, Taurus and Eridanus, as shown in Figure 3.1.

Prior SDSS-II work, such as the SNIa rate measurement of Dilday *et al.* [25], has noted systematic observational anomalies at the outermost edges of the stripe 82 RA range. Templates were not available for that region of the sky during the first year of observation, and the calibration star catalog does not completely cover that region. Therefore, I restrict my

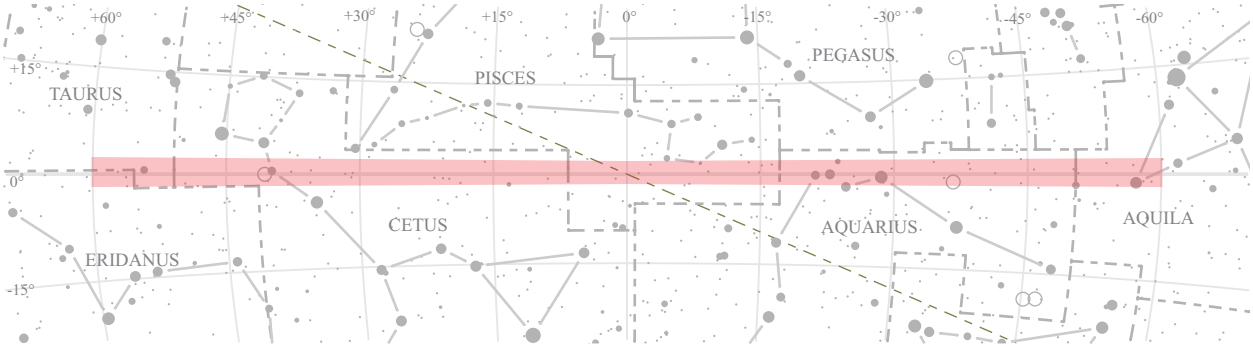

Figure 3.1: Stripe 82, the SDSS-II Supernova Survey region, is shaded in red

rate sample to include right ascension $-50°$ to $+55°$ only.

Numerous small patches of sky within stripe 82 are excluded from the search, because they are known to contain variable light sources that are not of interest to the survey, such as variable stars and quasars. This list of excluded patches is referred to as the veto catalog, which vetoes only ≈1 percent of the stripe.[25]

The first step in the analysis pipeline, performed on-site in observatory computers, is to produce astrometrically calibrated, corrected images using the standard SDSS photometric reduction process, developed and employed during the original SDSS observations [26].

The second step, also performed at the observatory, is to identify objects of variable luminosity. Supernovae differ from most other astronomical light sources in this regard, since stars and galaxies have relatively constant brightness. Fixed light sources are treated as a background signal, characterized by combining images of stripe 82 from many previous nights of observation to form a template image. This template image is subtracted from all the nightly images collected, using an adapted version of software developed by the ESSENCE collaboration [27]. Any bright source that remains in a subtracted image is therefore a variable object. If such an object is detected in at least two passbands and does not move during the ≈5 minutes between g and r band exposures, its images are transmitted to Fermilab computers for further processing [20].

The next step is to classify variable object images with a combination of software analysis

and human scanning. Some of the variable objects turn out not to be variable light sources at all; they are just artifacts of the observation process. Diffraction spikes from telescope optics can vary from one night to the next, and therefore be incorrectly flagged as variable objects. The brightest stars can saturate the Sloan telescope's camera CCDs, forming unpredictable patterns in the resulting image data. Asteroids within our solar system move through the field of view, and their change in position also appears as a difference versus the background template. Initially, the survey relied on human eyes to visually scan each image and identify these artifacts. Later, software routines were developed that filtered out most of the artifacts. Objects passing the software checks were still scanned by human eyes, and still contained a significant number of artifacts, though the volume of objects that required scanning was greatly reduced. Sample images of a supernova, and various rejected images, are shown in false color on Figure 3.2.

With artifacts removed and the remaining objects verified by human scanning, the survey has high confidence that these objects were indeed astronomical sources of variable luminosity. The next hurdle is to remove the large volume of variable sources that are not supernovae, primarily consisting of active galactic nuclei (AGN). A key difference between supernovae and AGN sources is that each supernova is a one-time event lasting only a few weeks or months, whereas variable stars and active galaxies tend to persist for many years. Many non-supernova objects were therefore excluded by removing those which are active in multiple viewing seasons.

Any object that survives this series of requirements is promoted to candidate status. Candidates are assigned an SDSS-II SN candidate ID number (CID), and queued for higher quality image analysis through the scene modeling photometry (SMP) program. SMP fits each image to a canonical form including an extended galaxy with a bright point source superimposed. The brightness of the point source is the output of the SMP program, along with some characteristics of the galaxy and the source's location within that galaxy. Details of the SMP program may be found in the 2007 publication by Holtzman *et al.* [29]. Repeating

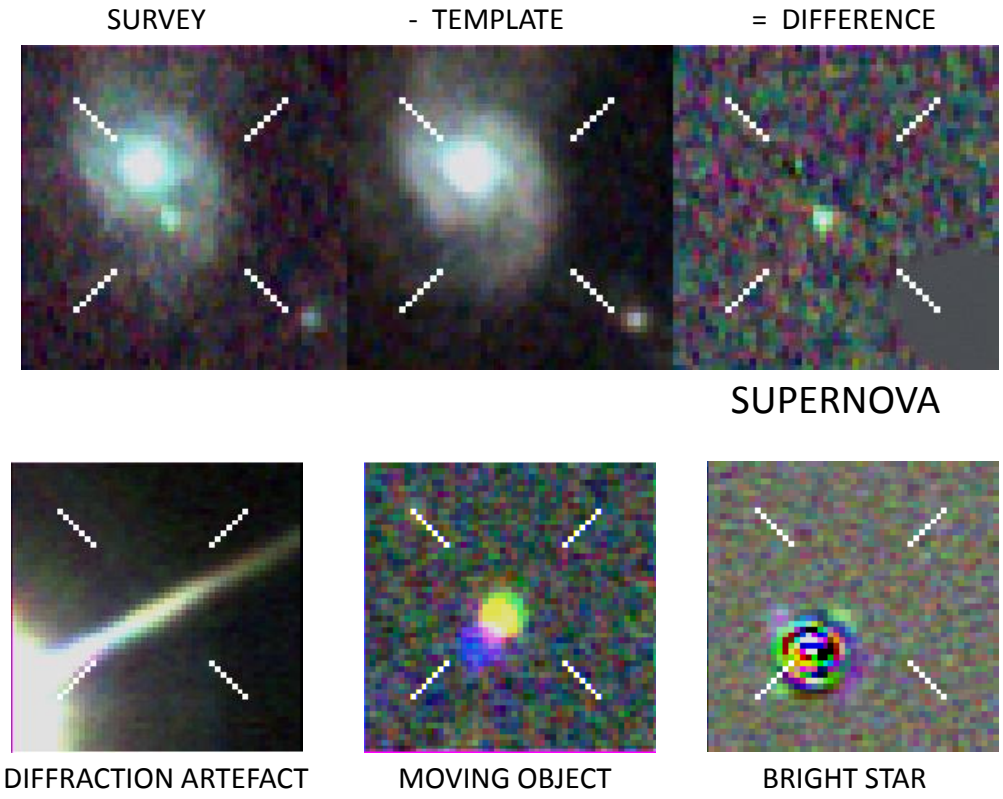

Figure 3.2: False color composites of images submitted to human visual scan, including an accepted supernova and some rejected images, are displayed in the SDSS-II scanning guide [28].

the SMP analysis for the full time sequence of images on a single object produces a light curve, a series of time-brightness pairs representing the time evolution of the object's light production.

Figure 3.3 illustrates the pipeline data flow, from raw Sloan telescope images to SDSS-II supernova candidate light curves.

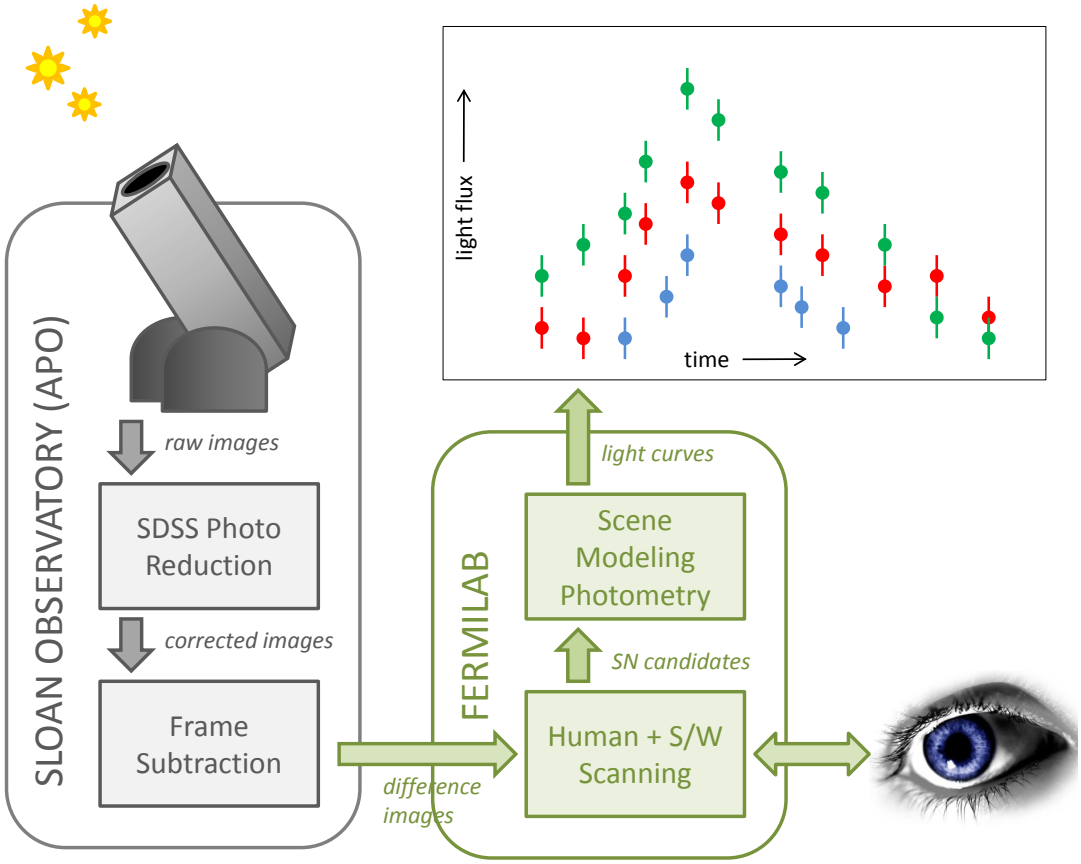

Figure 3.3: The SDSS-II Supernova Survey data analysis pipeline condenses raw telescope data into supernova candidate light curves.

3.2 Phenomenological Light Curve Fitting

My rate measurement begins with the complete set of SDSS-II SN candidate light curves, as produced by the analysis pipeline outlined in the preceding section. The SDSS-II SN

Survey used relatively loose criteria for identifying a supernova candidate, followed by stricter light curve quality criteria for the SNIa cosmology sample [21]. Of course, I do not apply the cosmology SNIa requirements for my sample, because SNIa are not core collapse supernovae. Therefore, the candidate set from which I begin includes a large number of variable objects that are not supernovae, such as variable stars, quasars and other active galaxies, or perhaps even novae within the Milky Way.

To separate supernovae from other variable object types, I employed the phenomenological light curve fitting method used by Bazin et al. in the Supernova Legacy Survey (SNLS). [1] Bazin models observed supernova brightness in each passband as a function of time using the parameterized formula:

$$f(t) = Ae^{-(\frac{t-t_0}{\tau_F})}(1 + e^{-(\frac{t-t_0}{\tau_R})})^{-1} \tag{3.1}$$

The left hand side of Equation 3.1 measures supernova brightness as flux, *i.e.* power received per unit area of the camera. The microjansky (μJy) is the unit of flux used by SDSS-II, equal to 10^{-32} watts per square meter.

The right hand side of Equation 3.1 contains four parameters, each of which is selected by the fitting program; A controls the overall amplitude of the light curve, t_0 roughly approximates the time of peak luminosity, τ_R governs the rate of flux increase long before the peak, and τ_F governs the rate of flux decrease long after the peak. Figure 3.4 shows the effect of varying each parameter on the shape of the model light curve.

Initial values for the four parameters, A, t_0, τ_R, and τ_F, are chosen by equating various integrals over the phenomenological form to corresponding sums over the light curve data. Three such quantities are used: t_{max} is the time of maximum flux, t_{bar} is the flux-weighted mean time, and σ is the flux-weighted standard deviation in time. I first find the intermediate value, a, defined as follows:

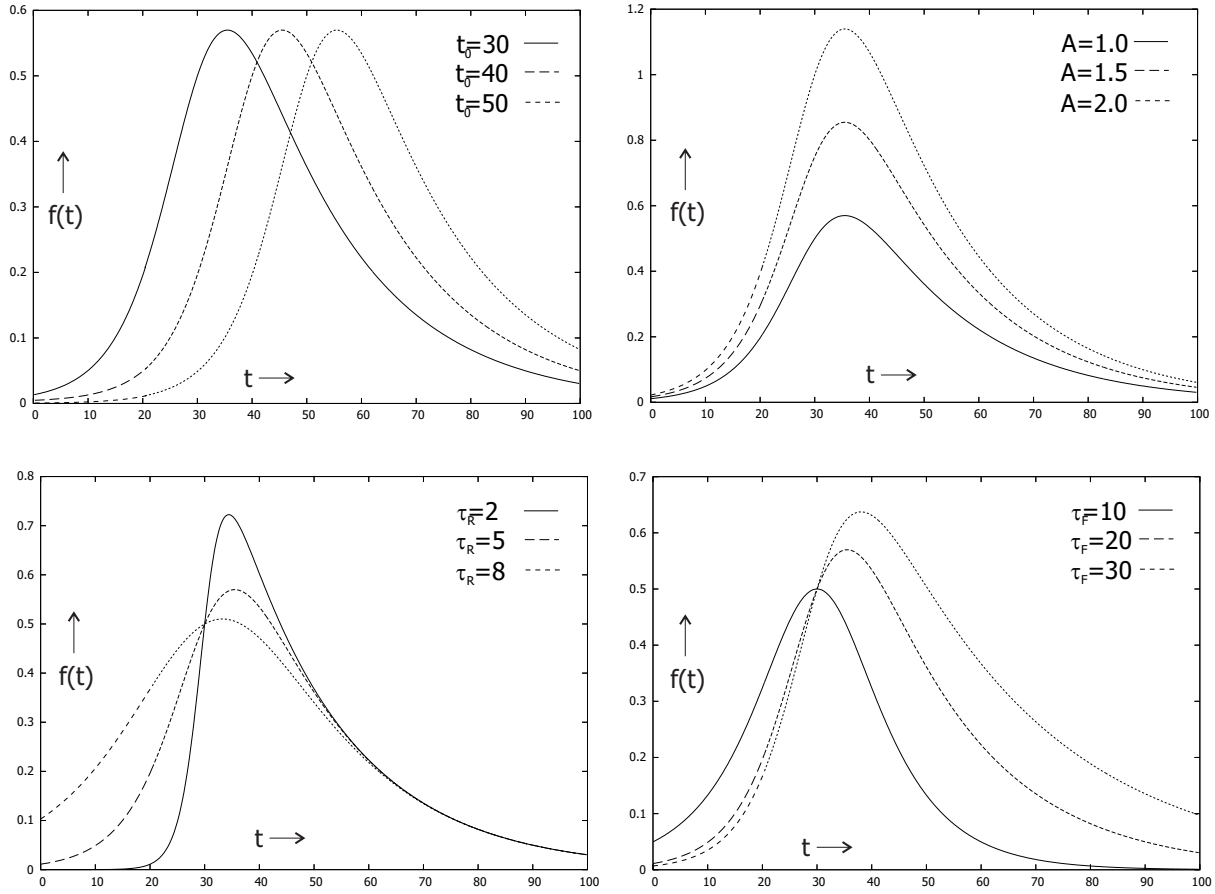

Figure 3.4: Model light curve functions are compared when varying a single parameter at a time.

$$a \equiv \pi \frac{\tau_R}{\tau_F} \approx \frac{\pi}{10} + 0.8 \cos^{-1}(\frac{6(t_{bar} - t_{max})}{7\sigma}) \tag{3.2}$$

Initial estimates for the phenomenological parameters can be expressed in terms of a, according to the following formulae:

$$t_0 = t_{bar} - \sigma \cos(a) \tag{3.3}$$

$$\tau_R = \frac{t_{bar} - t_0}{\pi} \tan(a) \tag{3.4}$$

$$\tau_F = \pi \frac{\tau_R}{a} \tag{3.5}$$

The initial value of the fourth, normalization parameter, A, is chosen to minimize chi-squared with the other three parameters held fixed, which has an exact, non-iterative solution. Chi squared is defined by:

$$\chi^2 = \sum_{i=0}^{N} \frac{(f_{model}(t_i) - f_i)^2}{\sigma_i^2} \tag{3.6}$$

where N is the number of measurements in the light curve, t_i is the time of each measurement, f_i is each measured flux and σ_i is the error in each measured flux.

To complete the fit, I apply an implementation of the Levenberg-Marquardt iterative algorithm developed by Joachim Wuttke under the name "lmfit" [30]. Of 9933 light curves processed, the fit failed to converge on 62 candidates. Of those, 50 candidates recorded null or negative flux in the r band for all epochs, so naturally those 50 are discarded. Visual inspection confirms that the remaining 12 display oscillatory features not characteristic of supernovae, as shown in Figures 3.5- 3.6. Therefore, I conclude that the error due to excluding non-converging fits is negligible compared to other sources of error.

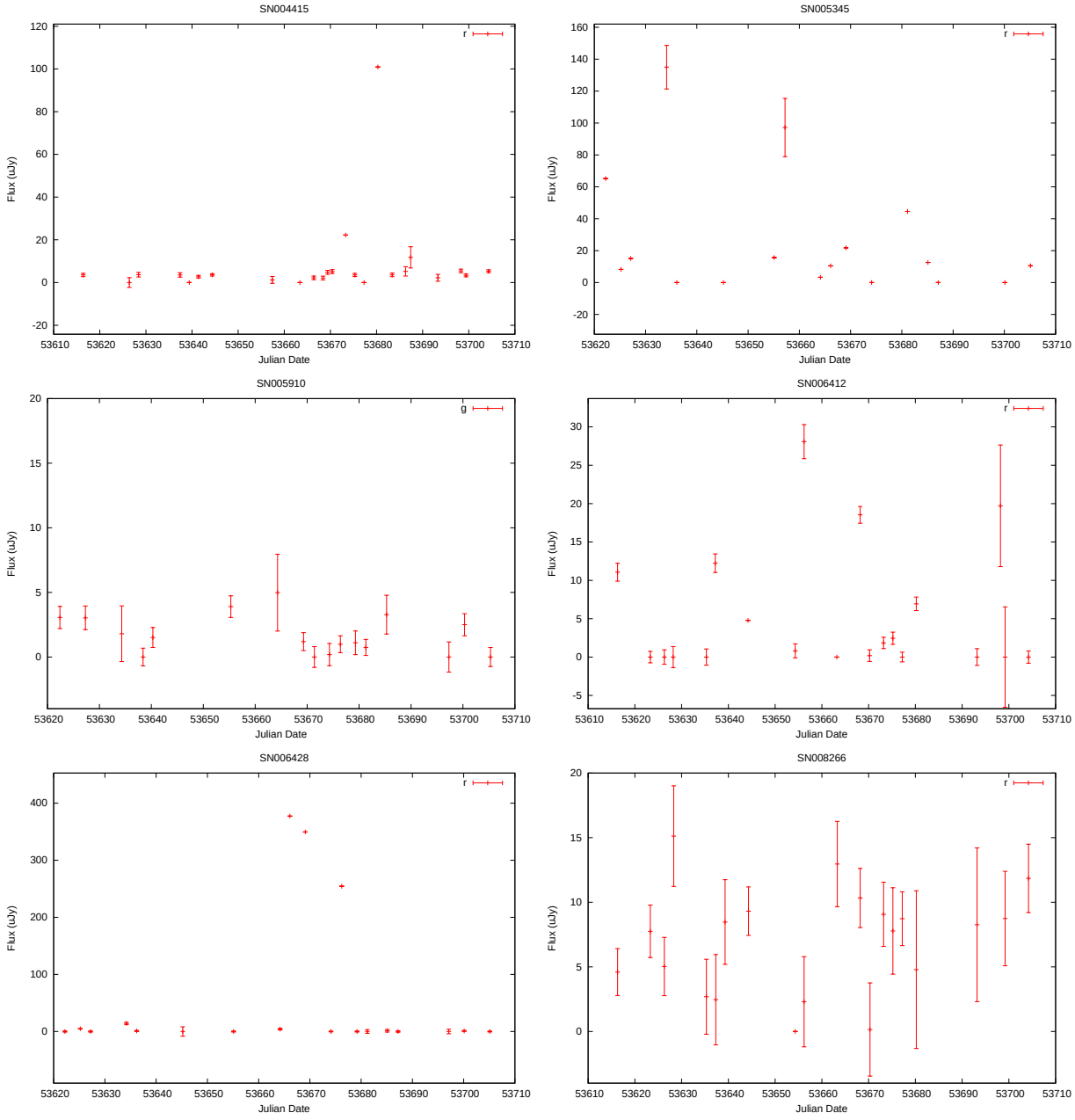

Figure 3.5: SDSS-II SN candidate light curves are shown for which the light curve model did not converge to a best fit.

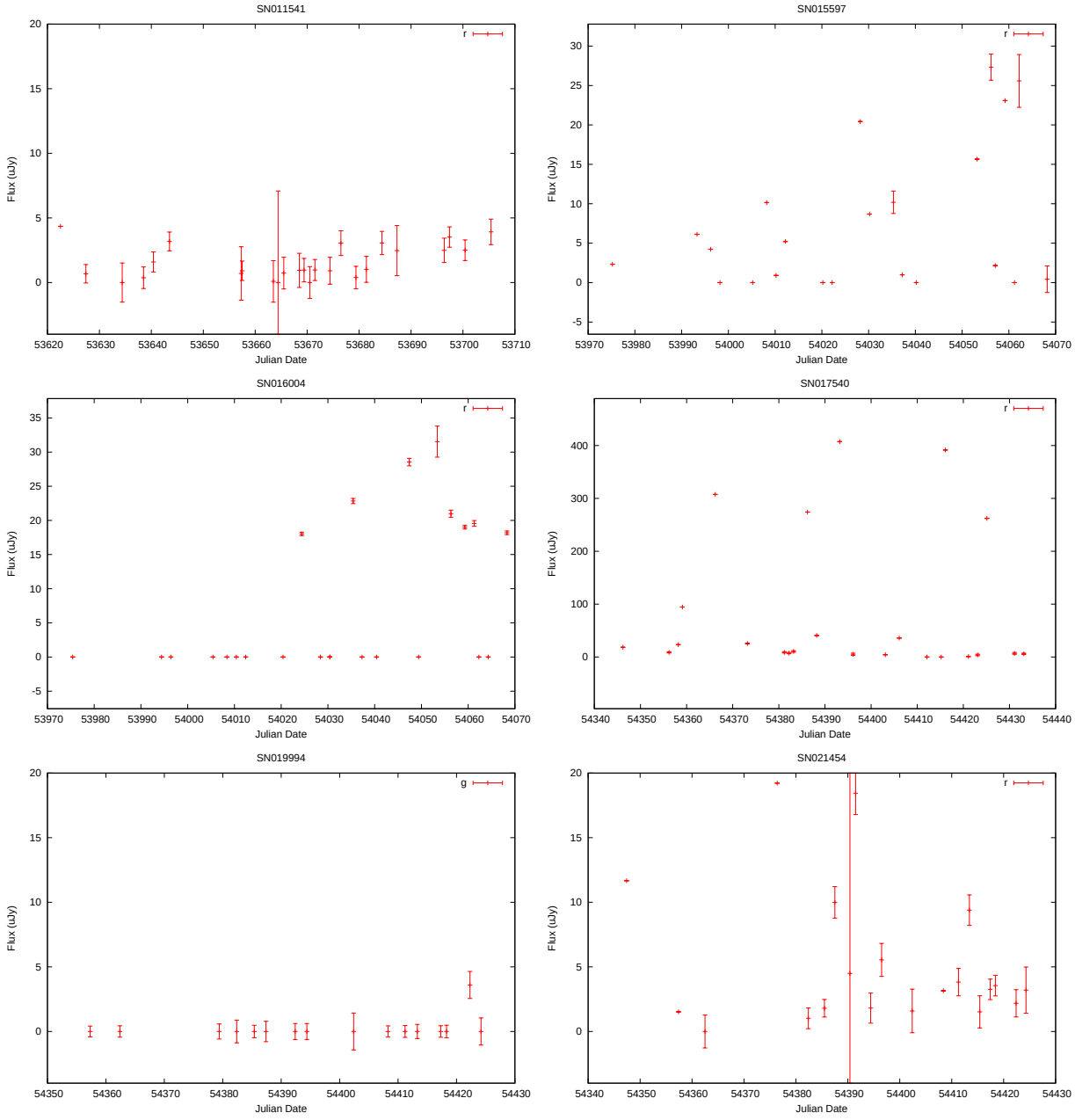

Figure 3.6: SDSS-II SN candidate light curves are shown for which the light curve model did not converge to a best fit.

3.3 Removal of Core Collapse Impostors

The phenomenological supernova model adapted from Bazin *et al.* can be fit to virtually any light curve; however, the fit will be poor for light curves without a clear, dominant peak. To measure the quality of the fit, I again follow the method of Bazin *et al.* [1] by fitting a second, trivial model to each light curve, which is just the best-fit constant flux. The chi-squared for this trivial fit can be solved exactly, without iteration.

When the trivial, constant flux fit has a chi-squared comparable to the chi-squared for the model fit, the object either is not a supernova, or the data is too noisy to identify it as a supernova. In either case, I remove such objects from the rate sample. The model and constant flux chi-squared can be directly compared, even though the model has three more degrees of freedom in its parameters, because both are fitted to the same number of data points, and that number is much greater than the number of free parameters. To quantify this comparison, I assign each light curve a flatness score, Λ, defined by:

$$\Lambda \equiv \frac{\chi^2_{model}}{\chi^2_{model} + \chi^2_{const}} \tag{3.7}$$

The value of Λ ranges from zero for the best measured, confirmed supernovae, to one for light curves that show no supernova features. Figure 3.7 shows the distribution of Λ for all SDSS-II SN candidates. It is is bimodal, with a large peak near $\Lambda = 0.5$, and a smaller peak near $\Lambda = 0$.

To test the correlation between flatness score and object type, I examine the Λ distribution for two candidate subsamples: core collapse supernovae and active galaxies, both of which have been confirmed through spectroscopic analysis, as described by Sako *et al.* (2008) [31]. The middle plot in Figure 3.7 shows that confirmed CCSN are concentrated near $\Lambda = 0$, while the bottom plot shows that confirmed AGN are concentrated near $\Lambda = 0.5$.

To remove the bulk of the non-supernovae from the rate sample, the rate calculation program calculates a cutoff, Λ_c, above which candidates are excluded. The program calculates

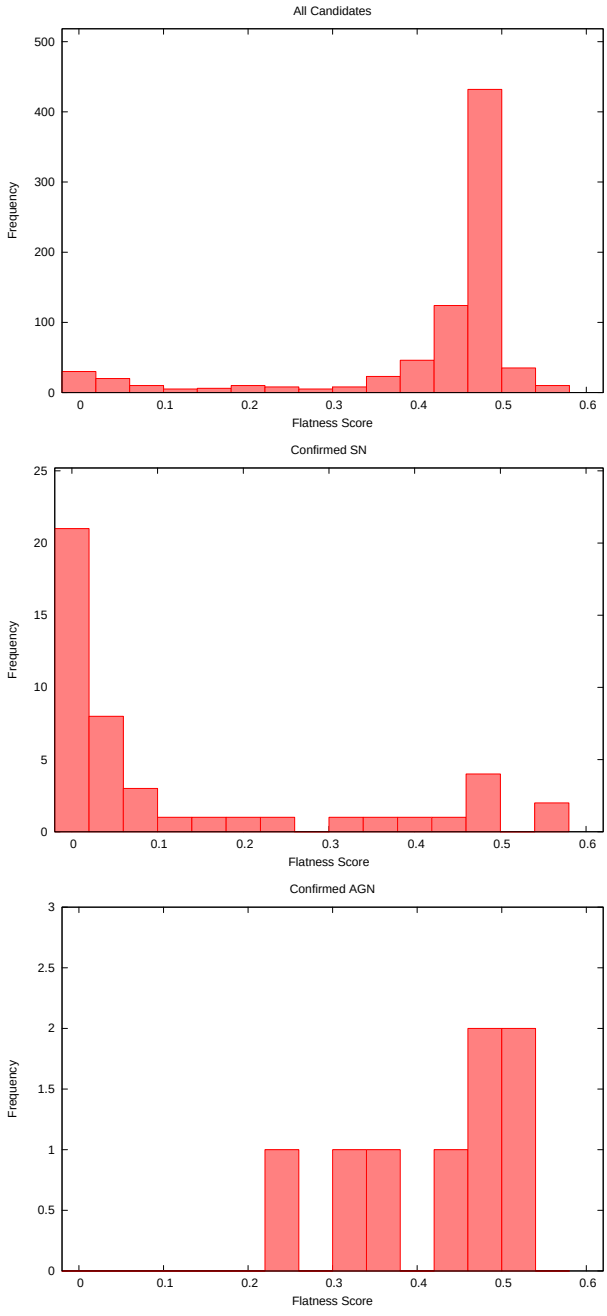

Figure 3.7: Flatness score distribution is shown for all candidates, for confirmed supernovae, and for confirmed AGN.

Λ_c by comparing the Λ distribution of the confirmed supernovae to that of the confirmed non-supernovae. In both the confirmed CCSN and confirmed AGN subsamples, there are some outlying light curves with unusually high or low Λ. The fraction of confirmed CCSN with $\Lambda > \Lambda_c$ estimates the rate of false negatives, *i.e.* the fraction of actual CCSN that will be removed from the rate sample at that value of Λ_c. Likewise, the fraction of confirmed AGN with $\Lambda < \Lambda_c$ estimates the rate of false positives, *i.e.* the fraction of SN impostors that will be included in the rate sample at that value of Λ_c.

The total number of candidates in the sample volume is known, up to detection efficiency, and each candidate has a flatness score. Therefore, for any choice of the cutoff value, Λ_c, the number of candidates below Λ_c (likely supernovae) and the number above Λ_c (likely AGN) are also known. Likewise, I estimate the number of false positives and false negatives as follows:

$$\text{false positives} = \left(\frac{\text{confirmed AGN with } \Lambda < \Lambda_c}{\text{all confirmed AGN}}\right) \times \text{candidates with } \Lambda > \Lambda_c \tag{3.8}$$

$$\text{false negatives} = \left(\frac{\text{confirmed CCSN with } \Lambda > \Lambda_c}{\text{all confirmed CCSN}}\right) \times \text{candidates with } \Lambda < \Lambda_c \tag{3.9}$$

The selected value, $\Lambda_c = 0.354$, is that at which the estimated number of false positives is equal to the estimated number of false negatives, implying that the correction to the supernova count for misidentification is zero. The rate of false positives and false negatives do, however, contribute to sources of systematic error. A selection of light curves excluded by the flatness score requirement is shown in Figures 3.8- 3.9.

One final class of impostors, thermonuclear supernovae of type Ia (SNIa), are unlikely to have been removed by the flatness requirement. Fortunately, the SDSS-II Supernova Survey has very sophisticated methods for identification of SNIa, as they are the primary targets of

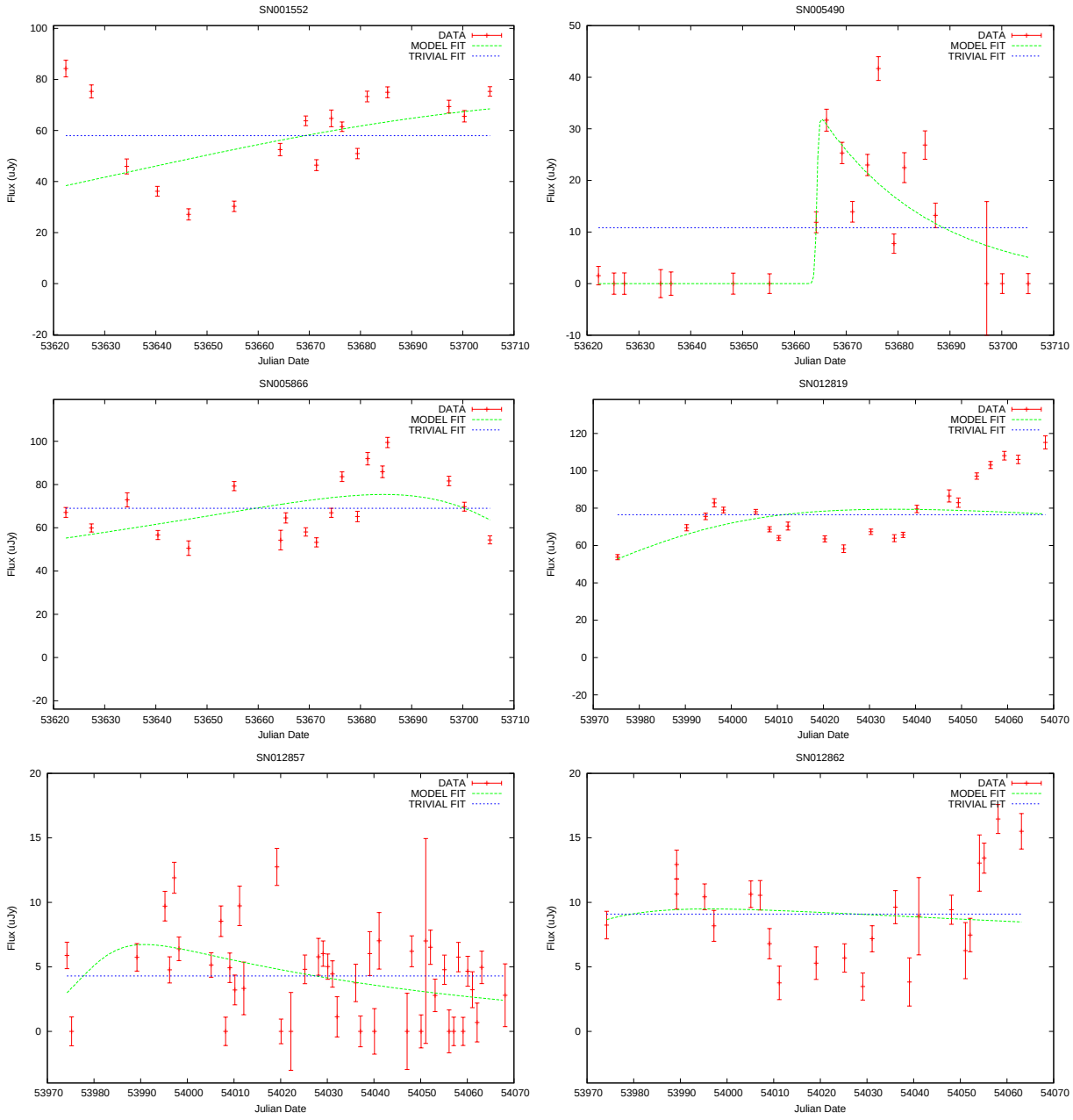

Figure 3.8: Above are examples of confirmed AGN light curves, with the best model fit plotted in green and the trivial, constant flux fit in blue. All these candidates were excluded by the flatness requirement.

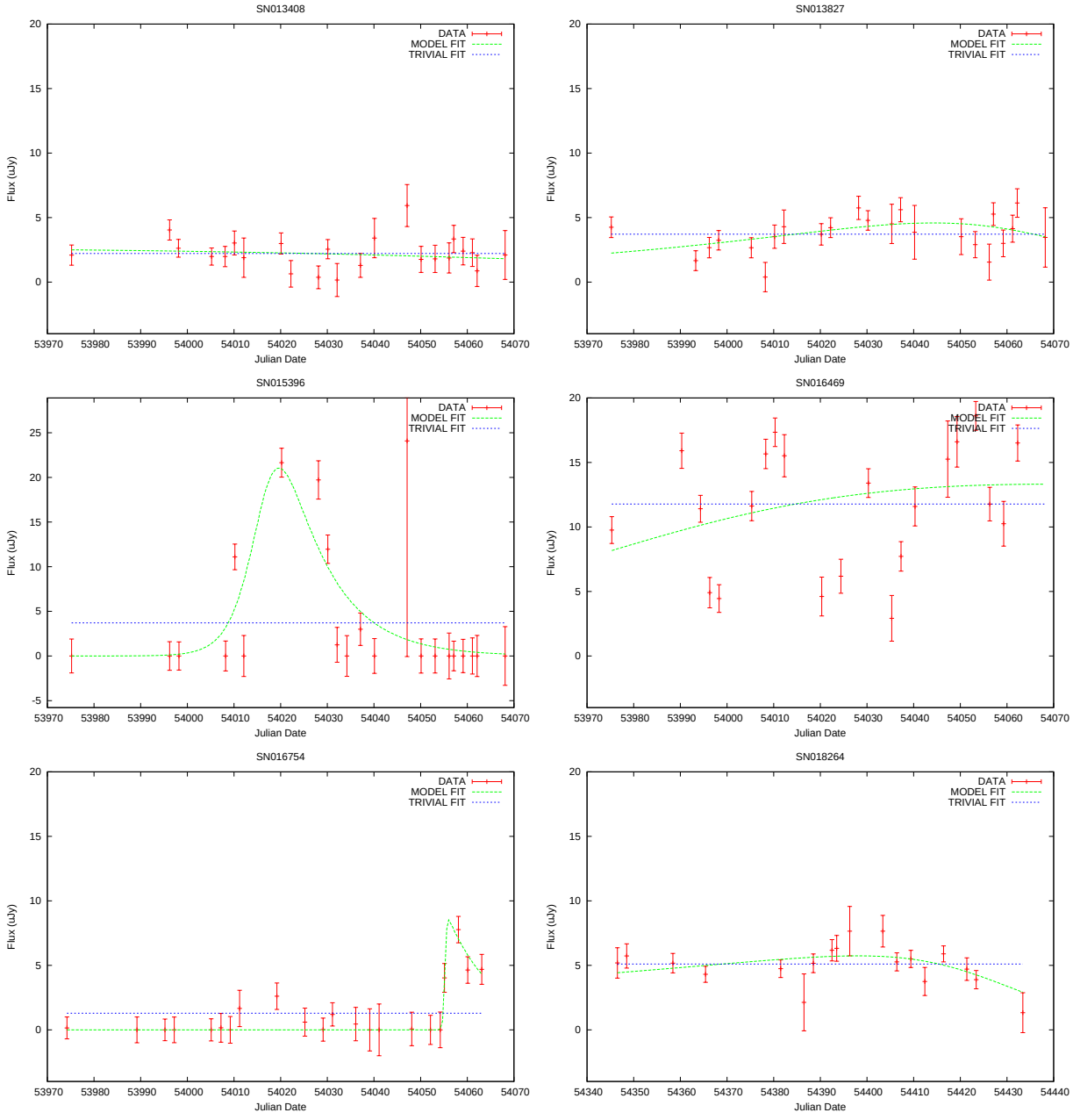

Figure 3.9: Above are examples of confirmed AGN light curves. All were excluded by the flatness requirement.

interest for the survey's cosmology mission [21].

Objects which display properties most similar to SNIa, and which are suitable for spectroscopic observation, are submitted to the SDSS-II SN Survey's partner observatories. The spectra obtained are subjected to a cross-correlation analysis, comparing them with template spectra for SNIa, CCSN and other object types. The spectroscopic target selection process and spectrum analysis are described in a publication by Zheng *et al.* [32]. Those which match the SNIa templates are marked as confirmed SNIa in the SDSS-II database, and I remove all such candidates from my CCSN rate sample.

The Sloan Observatory can identify many more supernova candidates than available spectroscopic resources can observe, therefore methods were developed to identify SNIa using only the photometric data from SDSS-II SN Survey itself. A software program was developed by M. Sako *et al.* [31] for exactly this purpose; the program attempts to fit light curves to a variety of supernova templates, selecting the supernova type which fits the data best. Those candidates identified as SNIa by this classification program are marked as photometric SNIa in the SDSS-II database, and I remove all such candidates from my CCSN rate sample.

In the region relatively near Earth where core collapse supernovae can be detected ($z < 0.1$), the combined photometric and spectroscopic identification of SNIa is very accurate. Simulation tests performed by Dilday *et al.* for their SNIa rate measurement found that less than 1 percent of survey-identified SNIa are actually CCSN. [23] CCSN are more than three times as numerous as SNIa in a given volume of space, therefore excluding survey-identified SNIa from my sample should remove less than 0.3 percent of CCSN from the rate calculation, an insignificant effect compared to other sources of error.

The remaining 89 candidates, after all requirements discussed above, form the core collapse supernova rate sample. Examples of some accepted CCSN candidate light curves are displayed in Figures 3.10- 3.11.

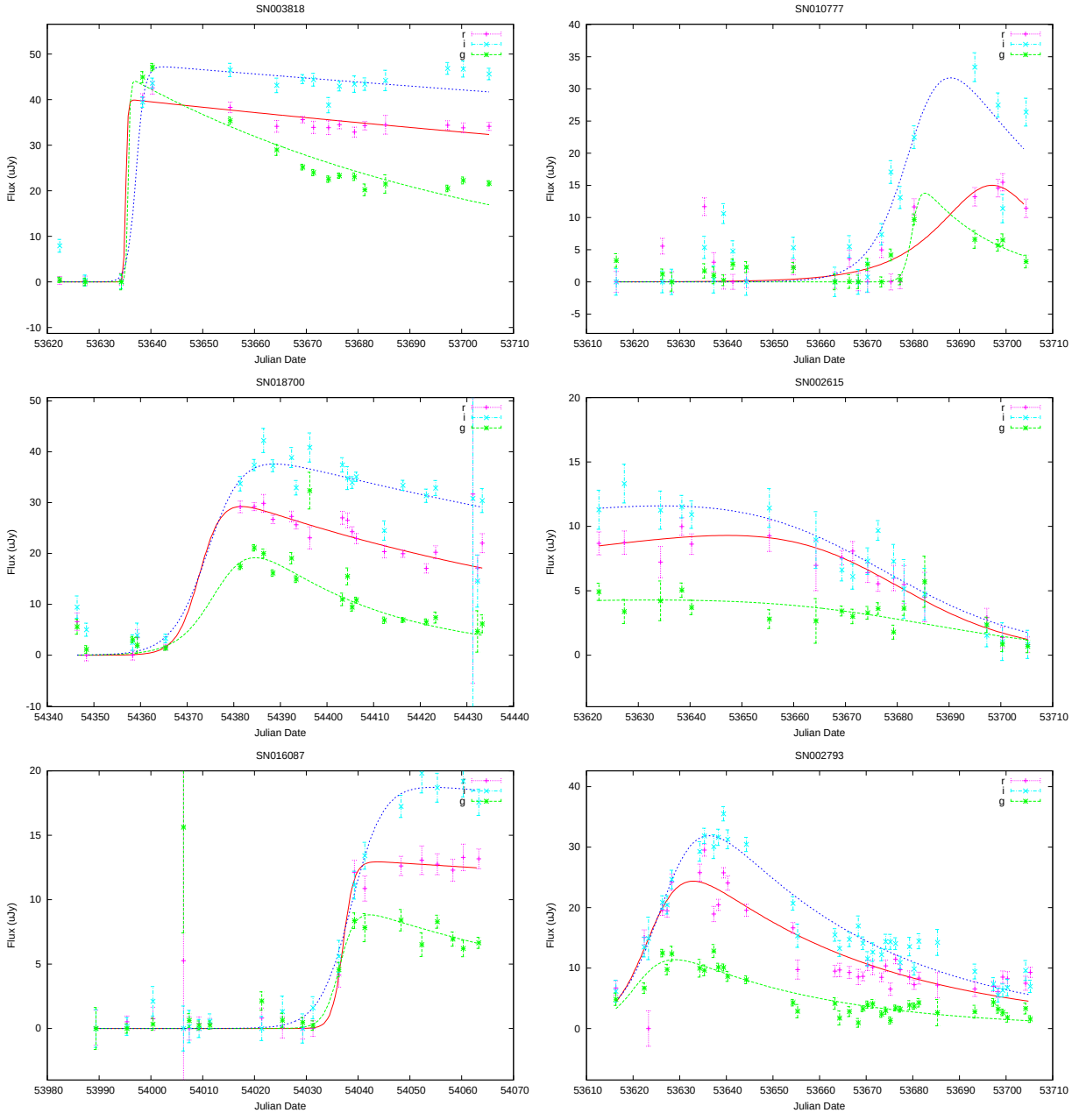

Figure 3.10: Above are examples from the accepted core collapse supernova rate sample.

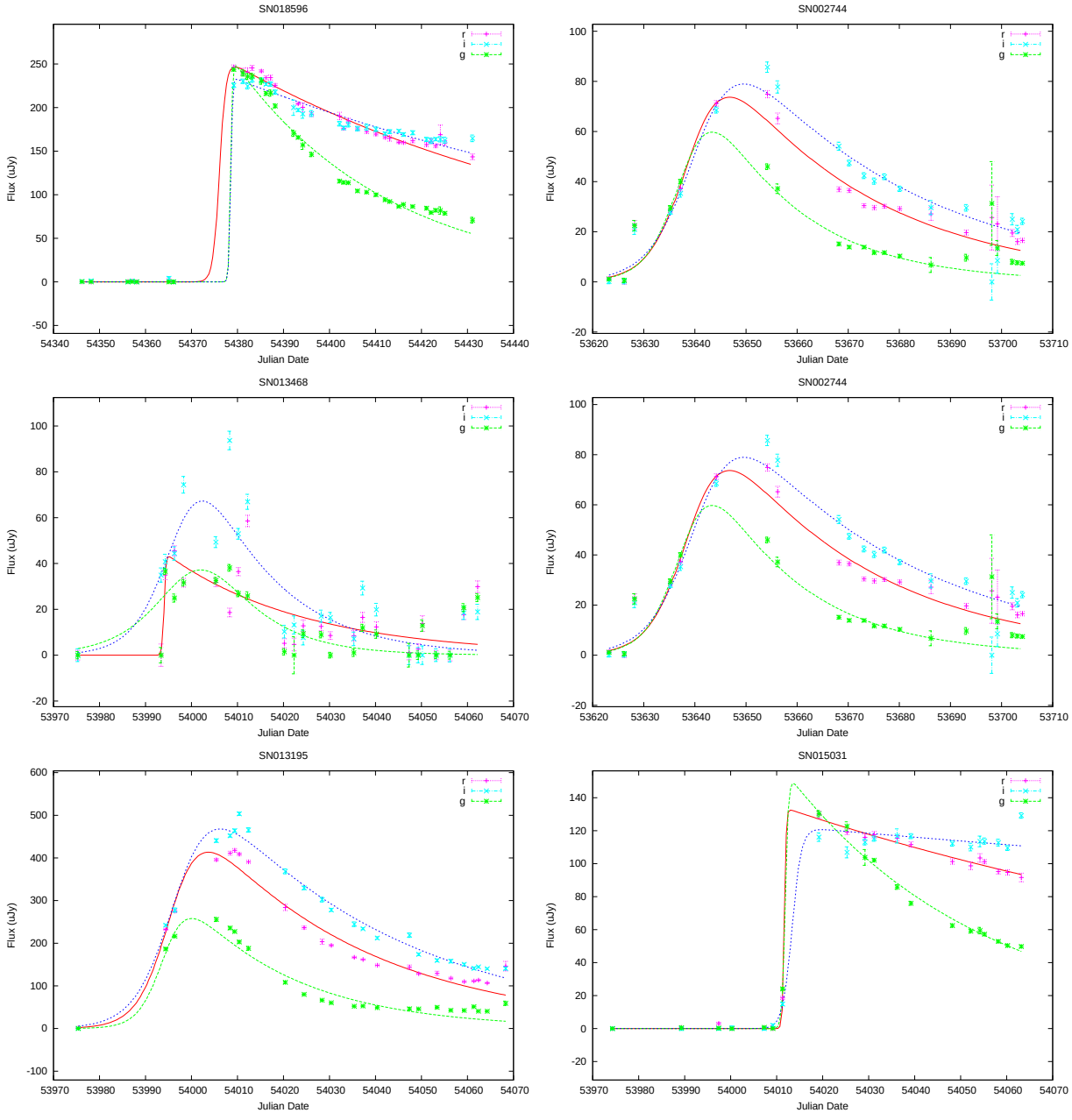

Figure 3.11: Above are examples from the accepted core collapse supernova rate sample

3.4 Luminosity, Distance and Volume Measurement

I measure the distance to a supernova via the spectrum redshift of the supernova itself, or of the galaxy in which it occurred. The preferred redshift measurements are those from the supernova spectrum itself, although this data is only available for a small fraction of candidates. More often, I use the redshift of the candidate's apparent host galaxy as an estimate of the supernova's redshift. Fortunately, SDSS-III BOSS has provided a spectroscopic redshift measurement for most of the host galaxies. The rest of the host galaxy redshifts are estimated using the photometric redshift algorithm of the original Sloan survey [34]. Figure 3.12 displays the resulting redshift distribution of candidates in the CCSN rate sample. Systematic error due to uncertainty in these photometric galaxy redshifts is estimated by comparing the photometric and spectroscopic redshift for those candidates where both are available, as explained further in Ch. 4.

For galaxies close enough to Earth that their redshift is about 0.03 or less, correlations between their peculiar velocities can be significant. These correlations can distort the apparent spatial distribution of supernovae. To avoid this systematic effect, I exclude any supernova candidate with redshift less than 0.03 from the rate sample.

As the distance from a light source to Earth increases, its apparent brightness decreases. Beyond redshift of about 0.1, the fraction of supernovae too faint for SDSS-II to detect begins to become significant. To reduce this additional systematic effect, I exclude any supernova candidate with redshift greater than 0.09 from the rate sample.

Exceptionally dim supernovae do exist, perhaps without a lower bound on absolute luminosity. If a lower bound on supernova luminosity exists, modern astronomy is not yet capable of detecting it. As the supernova's luminosity decreases, the effective volume in which the survey can detect it also decreases, because it must lie closer to Earth in order to be visible to the SDSS telescope. This means that the intrinsically dimmest supernovae are always under-represented in any fixed volume of space. To avoid this systematic effect, I exclude from the rate sample any supernova with peak absolute magnitude of -15.0 or

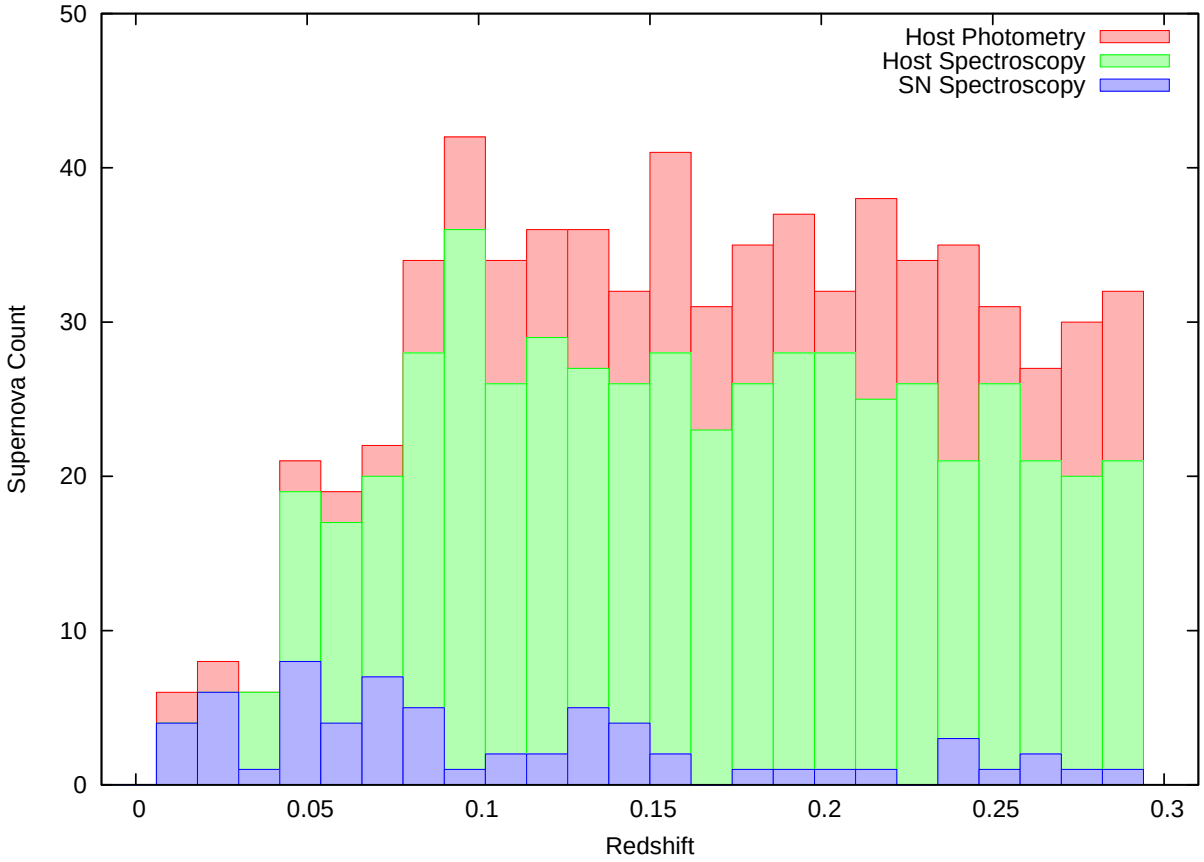

Figure 3.12: The redshift distribution of the raw CCSN rate sample is shown.

dimmer, in the SDSS r band. As all other supernova rate measurements to date suffer the same limitation, either implicitly or via an explicit luminosity requirement, my result will still be comparable to other rate measurements in the literature.

For purposes of this rate measurement, I am interested in the comoving volume that encloses the sample of supernovae. Comoving volume is defined as the space-time containing a set of objects, projected onto a constant time surface that contains the present era on Earth. In the redshift range of interest, the comoving distance as a function of redshift is well approximated by:

$$D_C(z) = \int_0^z D_H(\Omega_m(1+\zeta)^3 + \Omega_\Lambda)^{-1/2}\,\mathrm{d}\zeta \tag{3.10}$$

where $D_H = 4282.74$Mpc is the Hubble distance. The parameters $\Omega_m = 0.27$ and $\Omega_\Lambda = 0.73$ represent the current consensus ΛCDM cosmology. [36] To convert comoving distance to survey volume, I apply the following formula:

$$V_C = \frac{1}{3}\Omega(D_C(z=0.09)^3 - D_C(z=0.03)^3) \tag{3.11}$$

where Ω is the solid angle surveyed in steradians.

Uncertainty in cosmological parameters could make a small contribution to uncertainty in the comoving volume, and hence uncertainty in the supernova rate. However, this effect is very small at the redshift range where we observe CCSN. To probe the effect of varying cosmological parameters on comoving volume, I employed the iCosmos cosmological distance calculator, developed by M. Vardanyan [37].

The SDSS-II SN cosmology study found roughly 5 percent uncertainty in Ω_m [21], which translates to approximately 0.3 percent uncertainty in comoving volume at $z = 0.1$. This error due to uncertainty in Ω_m, the cosmic matter density parameter, is an order of magnitude smaller than other sources of error, and therefore I ignore it in this work.

Kessler *et al.* also found approximately 10 percent uncertainty in w [21], the dark energy

equation of state parameter, which translates to about 1.3 percent uncertainty in comoving volume at $z = 0.09$. The effect of uncertainty in w is small, but it is significant enough to account for in sources of error for the CCSN rate, and I have included it in the error tabulation in Chapter four.

3.5 Supernova Time and Luminosity

A supernova rate measurement treats each supernova as an instantaneous event. This view is physically appropriate, since a star's initial core collapse event spans only a few seconds of time. However, surveys such as SDSS-II have much coarser time resolution. Each object is imaged at most once every two days, and the optically bright explosion evolves much more slowly than the initial core collapse, on the scale of weeks or even months.

As is common in supernova research, I use the supernova's peak luminosity in the SDSS r band to mark its occurrence in time. While the time delay between initial core collapse and peak luminosity can vary among supernovae, there is always exactly one peak per core collapse. Therefore, the rate of observed luminosity peaks must equal the rate of core collapse events.

I determine the peak luminosity and time of each light curve from its fitted model function. To exclude spurious peaks, I require that the peak occur at least 10 days after the start of an SDSS-II viewing season, and at least 10 days prior to the end of a season. Also, there must be at least one observation of the supernova preceding the peak by 12 hours or more, and one following the peak by 12 hours or more. The 12 hour gap ensures that the observation is not on the same night as the peak.

Because the SDSS-II viewing season is shorter than the observable duration of a supernova, there is a possibility that I could mistake a local maximum in the light curve for a true luminosity peak. To estimate error due to this effect, I repeated the rate calculation excluding an additional 10 days of each viewing season. In this test, the peak finding algo-

rithm only identified one false peak out of few hundred candidate light curves. Therefore, I conclude that overcounting due to false peaks is not significant compared to other sources of error.

3.6 Supernova Detection Efficiency Model

The magnitude limit, beyond which a supernova is too dim for the survey to detect, is not a sharp boundary. There is a range of magnitudes in which supernovae have a finite probability of detection, referred to as the survey's detection efficiency. For this work, I model the detection efficiency as a function of the supernova's peak apparent magnitude, as seen from Earth in the SDSS r band. The form of the model efficiency function, $\epsilon(m)$ is:

$$\epsilon(m) = \frac{1}{2}(1 + \cos(\frac{\pi}{\sigma_E}(m - m_E))) \tag{3.12}$$

in the range $(m_E < m < m_E + \sigma_E)$, where m is the supernova peak magnitude.

Outside the range where $\epsilon(m)$ is defined, the efficiency is one $(m < m_E)$ or zero $(m > m_E + \sigma_E)$. The first parameter, m_E, defines the dimmest magnitude at which the survey's detection efficiency is perfect, for practical purposes. The second parameter, σ_E, defines the width of the magnitude range over which the efficiency falls from unity to zero.

The model parameters, m_E and σ_E, are chosen through a fitting routine. First, I build a model for the supernova rate sample as a function of limiting magnitude, using only those candidates bright enough that detection efficiency is nearly one. The number of candidates, $N_p(m)$ is expected to have the form:

$$N_p(m) = (p_0 + p_1 10^{0.6m} + p_2 10^{0.8m} + p_3 10^{1.0m} + p_4 10^{1.2m}) \tag{3.13}$$

where m is the limiting peak apparent magnitude in the SDSS r band.

Equation 3.13 may be derived by first expressing the SN rate, ρ_{SN}, as a function of

luminosity distance, D. Expanding $\rho_{SN}(D)$ with a Taylor series in D, the lowest order nonzero term must be proportional to D^2, since space appears flat and the SN rate appears uniform on sufficiently small distance scales. Therefore, the series appears as follows:

$$\rho_{SN}(D)\ \mathrm{d}V = (\sum_{k=2}^{\infty} c_k D^k)\ \mathrm{d}D \tag{3.14}$$

The luminosity distance, D, can be expressed in terms of the distance modulus, μ, according to:

$$D = (10\mathrm{pc})\ 10^{0.2\mu} \tag{3.15}$$

Combining Equation 3.15 and Equation 3.14 produces:

$$\rho_{SN}(\mu)\ \mathrm{d}V = (\sum_{k=3}^{\infty} b_k 10^{0.2k\mu})\ \mathrm{d}\mu \tag{3.16}$$

where constant factors have been rolled into the new coefficients, b_k. Now convolve Equation 3.16 with the SN luminosity function, $\psi(M)$, to find the supernova count as a function of limiting magnitude, as follows:

$$N_p(m) = \int_{-\infty}^{\infty} \psi(M) \int_{\mu=m_0-M}^{\mu=m-M} \rho_{SN}(\mu)\ \mathrm{d}V\ \mathrm{d}M \tag{3.17}$$

where m_0 is the brightest apparent magnitude that the SDSS telescope can image without saturating the camera. Combining Equation 3.16 and Equation 3.17, then integrating and simplifying, we have:

$$N_p(m) = \sum_{k=3}^{\infty} \int_{-\infty}^{\infty} \psi(M) 10^{-0.2kM}\ \mathrm{d}M \frac{b_k}{0.2\ \ln\ 10}(10^{0.2km} - 10^{0.2km_0}) \tag{3.18}$$

Collecting factors independent of the limiting apparent magnitude, m, in the relabeled coefficients, p_k, and truncating at order $10^{1.2m}$, produces Equation 3.13.

Once the best fit $N_p(m)$ is obtained for the bright portion of the rate sample, it is

compared to the actual number of candidates at dimmer limiting magnitudes, $N_a(m)$. The form of $N_p(m)$ should be nearly the same at dim magnitudes as at bright magnitudes, since each cohort in apparent magnitude includes objects at a wide range of distances from Earth. The model and actual supernova counts are shown in Figure 3.13.

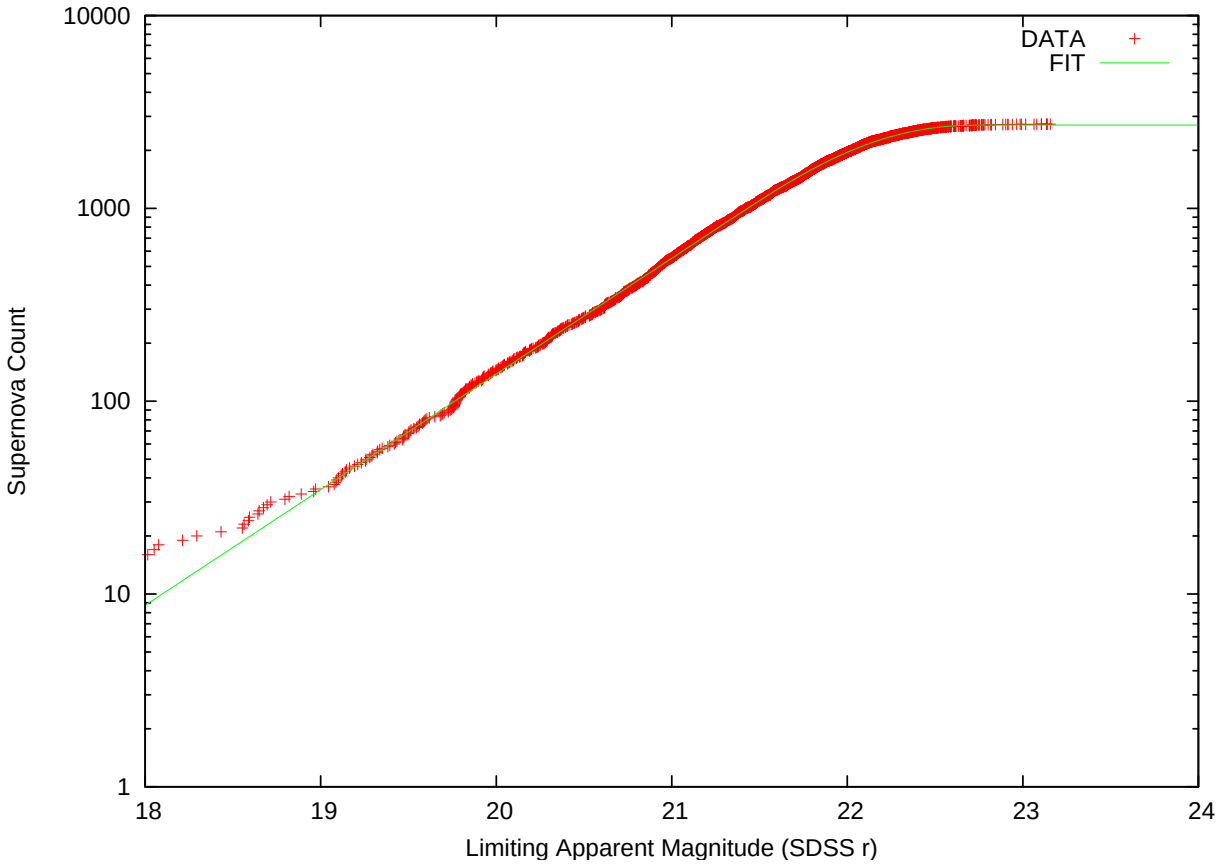

Figure 3.13: The supernova count is plotted versus limiting apparent magnitude.

Next, the actual number of candidates, $N_a(m)$, is fit to the expected form given in Equation 3.19.

$$N_a(m) = \int_{-\infty}^{m} \epsilon(\mu) N_p(\mu)\, \mathrm{d}\mu \tag{3.19}$$

The parameters of $N_p(m)$, the model population function, are held fixed at the values fitted to the bright subsample, while the parameters of $\epsilon(m)$, the efficiency function, are

allowed to float. The resulting, best fit efficiency model is displayed in Figure 3.14.

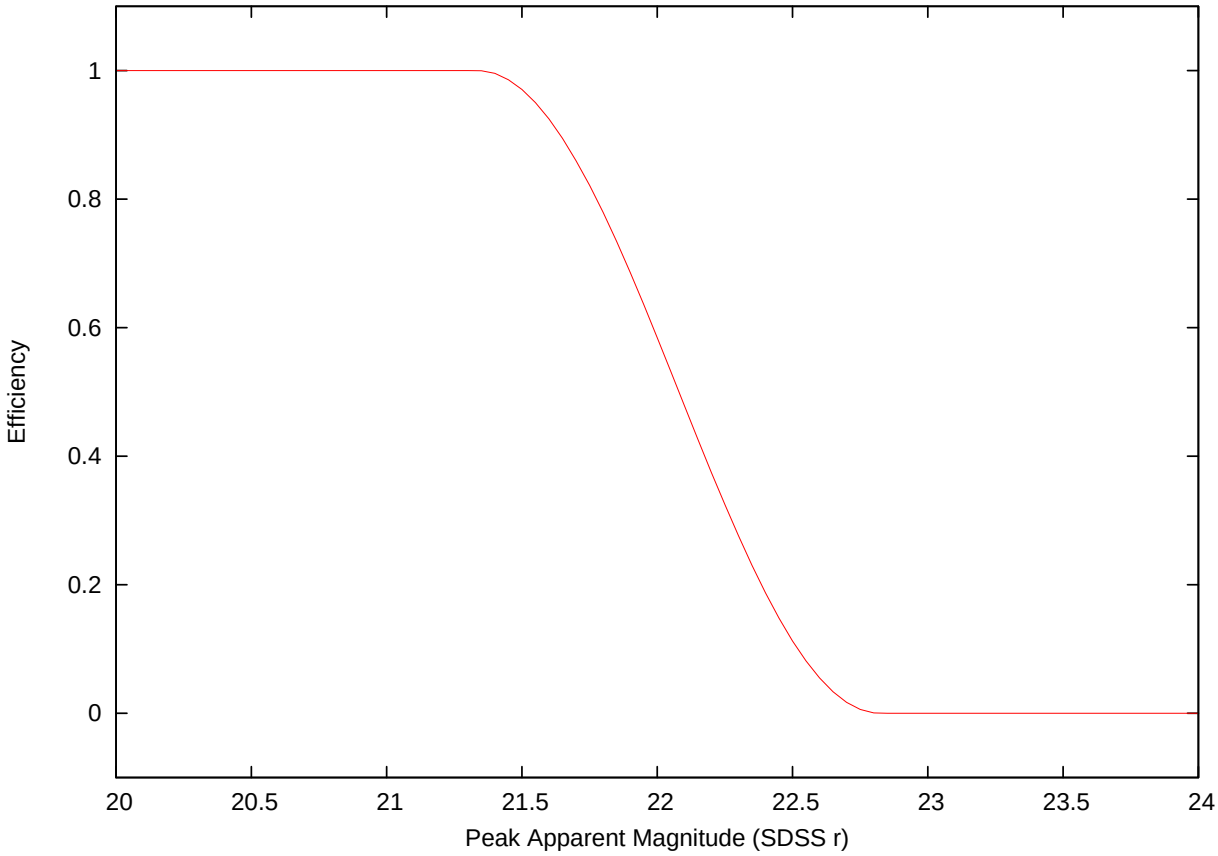

Figure 3.14: The model supernova detection efficiency is shown.

With the detection efficiency model in hand, I weight each supernova candidate according to the inverse of the efficiency at its peak apparent magnitude. The corrected supernova count is then the sum of these weights, for all accepted candidates. In rare cases where a supernova is detected at a very inefficient magnitude, i.e. $\epsilon(m) < 0.2$, the candidate is excluded to avoid a large, spurious increase to the supernova count.

The resulting, corrected redshift distribution is shown in Figure 3.15. The actual supernova count is expected to increase as the third power of redshift or more, because of the increasing volume sampled. However, beyond $z \approx 0.1$, an increasingly large fraction of the CCSN population is at magnitudes where the survey has very low or zero detection efficiency. The rate sample has therefore been truncated at $z = 0.09$ to avoid this effect.

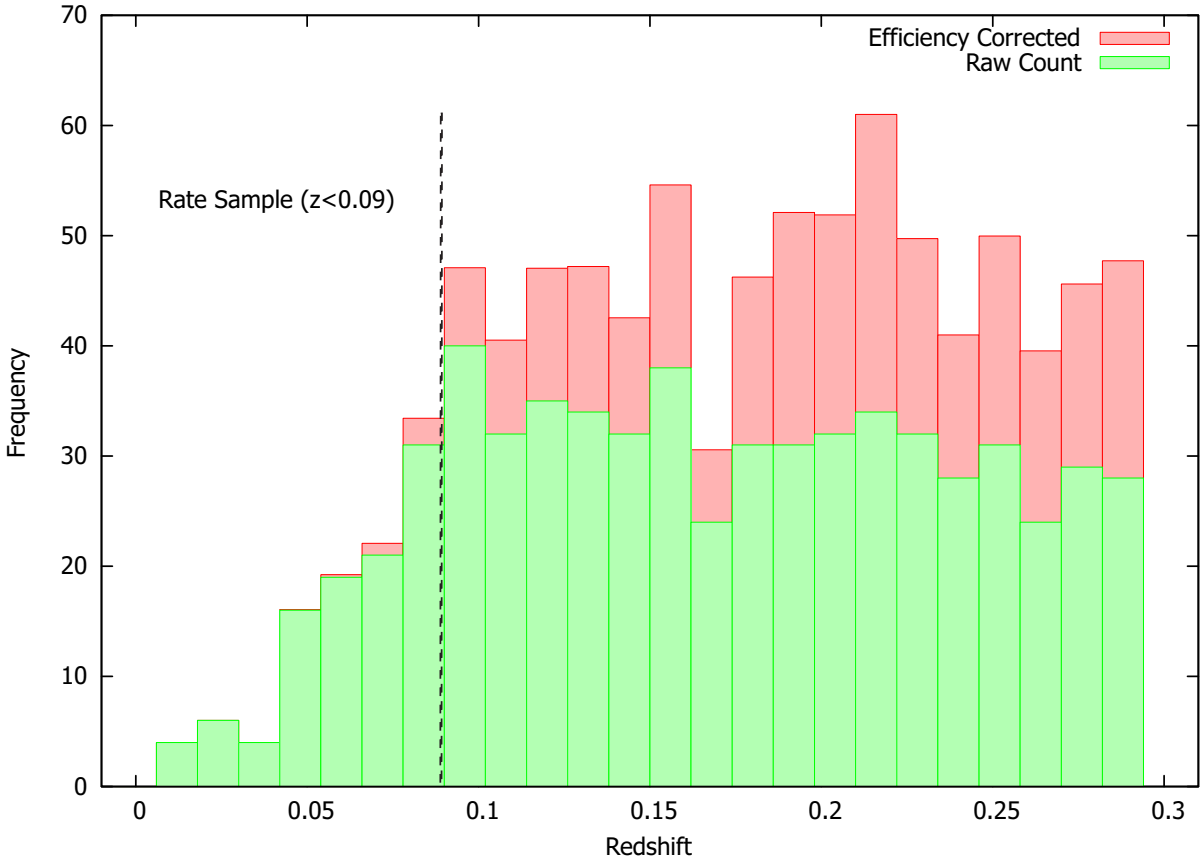

Figure 3.15: The redshift distribution of the CCSN rate sample is shown, subluminous candidates excluded, before and after the efficiency correction.

3.7 Host Galaxy Extinction Model

The observed luminosity of a supernova may be less than its actual luminosity, a phenomenon referred to as extinction. Extinction occurs due to the presence of dust, *i.e.* particles that scatter and/or absorb light, between the supernova and Earth. Dust within the Milky Way is relatively well understood, and SDSS-II supernova light curves have already been corrected for its effects by the SDSS-II Supernova Survey data pipeline. [21]

However, dust in each supernova's host galaxy, or perhaps even in the local environment of the supernova itself, is more difficult to measure. This local extinction is well represented by the model of Cardelli *et al.* [38], which quantifies extinction of a bright source with two parameters, A_V and R_V. The A_V parameter specifies the change in magnitude due to dust absorption, in the Johnson V band, and the R_V parameter specifies the wavelength dependence of dust absorption. Dust absorption is more pronounced at longer (red) wavelengths.

The central wavelength of the SDSS r filter, at 623 nm, lies between the Johnson R and V filters, at 658 nm and 551 nm respectively. Cardelli *et al.* find that $A_R/A_V \approx 0.75$ for the standard value of $R_V = 3.1$ in the diffuse interstellar medium [38]. Interpolating between A_R and A_V to estimate extinction in the SDSS r band, I find that $A_r/A_V = 0.83$.

Correcting for the effect of extinction on the observed supernova rate then requires a statistical distribution of A_r for core collapse supernovae. I employ the model developed by Hatano *et al.* [39], who simulated an ensemble of host galaxies at random inclinations, and placed model supernovae within them approximating the spatial distribution of observed supernovae. Dust along the resulting line of sight determined the extinction of each model supernova. The resulting A_V distribution is roughly exponential with exponent $\tau = 0.50 \pm 0.03$. Converting to SDSS r band scales τ in proportion to A_r/A_V, yielding a corrected exponent of $\tau = 0.42 \pm 0.03$.

$$\mathrm{P}(A_r) \approx \frac{1}{\tau} e^{-\frac{A_r}{\tau}} \tag{3.20}$$

The number of observed supernova, $N_{obs}(M)$, as a function of limiting magnitude, M, is then given by:

$$N_{obs}(M) = \int_{-\infty}^{\infty} \frac{\mathrm{d}N}{\mathrm{d}m} \int_{0}^{\infty} \frac{1}{\tau} e^{-\frac{A_r}{\tau}} \theta(M - (m + A_r)) \, \mathrm{d}A_r \, \mathrm{d}m \tag{3.21}$$

The integral over A_r can be solved exactly, as follows:

$$N_{obs}(M) = \int_{-\infty}^{\infty} \frac{\mathrm{d}N}{\mathrm{d}m} (1 - e^{\frac{m-M}{\tau}}) \, \mathrm{d}m = N_{actual} - \int_{-\infty}^{\infty} \frac{\mathrm{d}N}{\mathrm{d}m} e^{\frac{m-M}{\tau}} \, \mathrm{d}m \tag{3.22}$$

Now take the derivative on both sides with respect to the limiting magnitude, M, and simplify, resulting in the following:

$$N_{corrected}(M) - N_{obs}(M) = \tau \frac{\mathrm{d}N_{obs}}{\mathrm{d}M} \tag{3.23}$$

The above is just the correction to the supernova count, due to extinction. To estimate that correction, I fit a line to $N_{obs}(M)$ in the vicinity of absolute magnitude -15.0, and take the line's slope as the value of $\mathrm{d}N_{obs}/\mathrm{d}M$. Because of poorly quantified uncertainties in the extinction model, I count 100% of this correction as a source of systematic error. Fortunately, the extinction correction is small, less than 3 percent of the measured rate.

Chapter 4

Results

4.1 Supernova Count

The SDSS-II Supernova Survey had three viewing seasons of approximately 90 days each from 2005-2007, in the Northern Hemisphere autumn when the Sun is located furthest from the Stripe 82 region in Earth's sky. Over these three seasons, the survey identified a total of 10,606 supernova candidates which met the candidate criteria set forth by Frieman *et al.* [20]:

- The automated object detection algorithm detects a change in brightness versus the template, in two or more passbands.
- The object location is not on the veto list of known variable stars and galaxies.
- Human and software scans did not reject it as an artifact or Solar System object.
- The object was not active in multiple viewing seasons.

Of these, 9,934 candidates were active within the time and space constraints I chose for the core collapse rate sample, *i.e.* between right ascension $-50°$ to $+55°$, and in the 2005, 2006 or 2007 viewing season.

Phenomenological light curve fitting, using the method of Bazin *et al.* [1], rejected 50 candidates with null or negative flux in all epochs, and another 12 candidates for which the fit did not converge. The latter 12 light curves are displayed in Figures 3.5- 3.6.

After fitting light curves to the Bazin model, I excluded all candidates where the model peak occurs in the first or last 10 days of a viewing season, or where there is not at least one observation 12 hours prior and 12 hours following the peak. This requirement removed 479 candidates. The peak time distribution of the remaining sample is displayed in Figure 4.1. While the raw distribution shows systematic time bias, filtering by peak magnitude shows that the bias primarily affects objects dimmer than peak magnitude 22.0, near the limit of the survey depth.

The quality of the light curve fit is measured using the flatness score, Λ, defined in Equation 3.7, as explained in Ch. 3.3. I removed a total of 6,513 candidates from the rate sample for exceeding the flatness score threshold, $\Lambda_c = 0.354$, nearly 70 percent of candidates. However, the great majority of such candidates are well beyond Λ_c, in a range where confirmed supernovae occur very rarely, as shown in Figure 3.7.

To locate a supernova candidate in three dimensional space, I require a distance measurement, in addition to its angular coordinates. I use cosmic redshift as a distance indicator, according to the formula for comoving distance as a function of redshift described in Ch. 3.4. Spectroscopic redshift of the supernova itself is preferred, but when that is not available I instead use the spectroscopic redshift of the host galaxy, or a photometric redshift estimate of the host galaxy as a last resort. However, in a few cases no spectra were taken of the supernova, and the host galaxy is too faint to detect, thus I have no guidance at all for the candidate's distance.

I removed 150 candidates from the sample due to lack of redshift information, treating all of them as non-detections. Figure 4.2 shows the peak magnitude distribution of such candidates. By treating candidates with no redshift as non-detections, I aim to correct for their omission with the detection efficiency model, especially since redshift is most likely

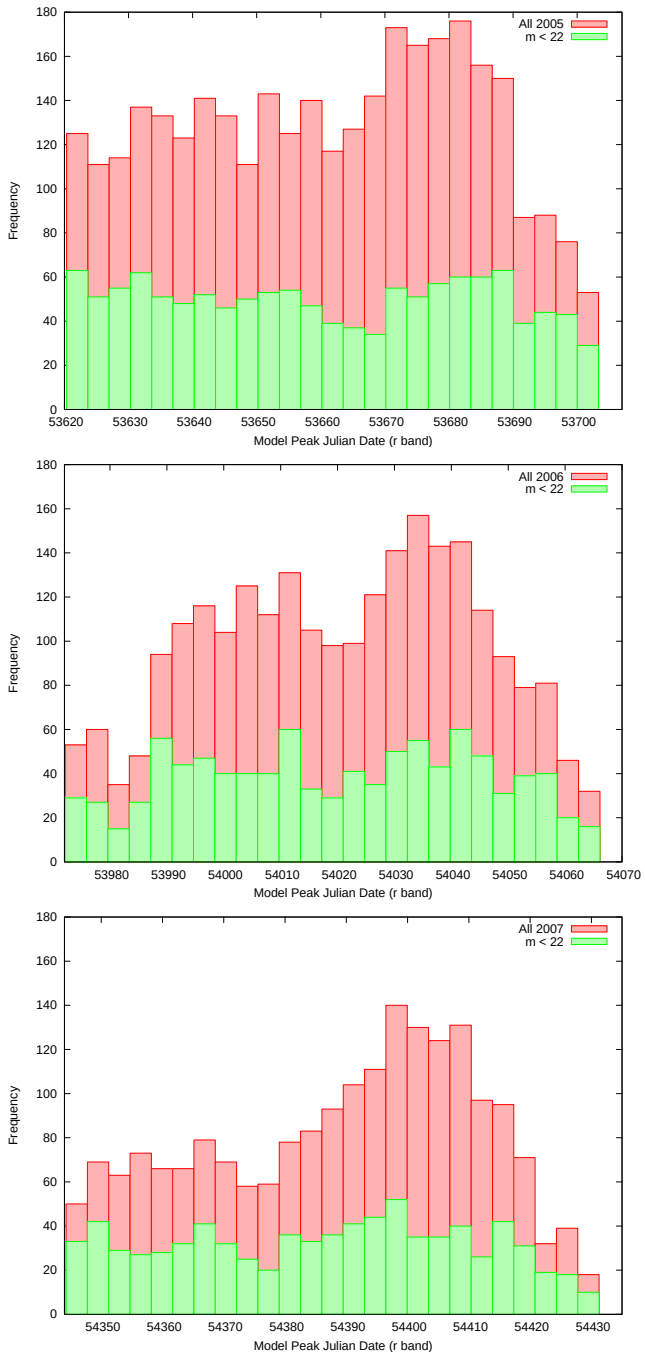

Figure 4.1: Peak time distribution is shown for all candidates within the time and angle constraints discussed in the text. A peak magnitude requirement shows that systematic time bias primarily affects very dim objects.

to be unavailable under the same conditions where detection efficiency is low, *i.e.* for dim objects.

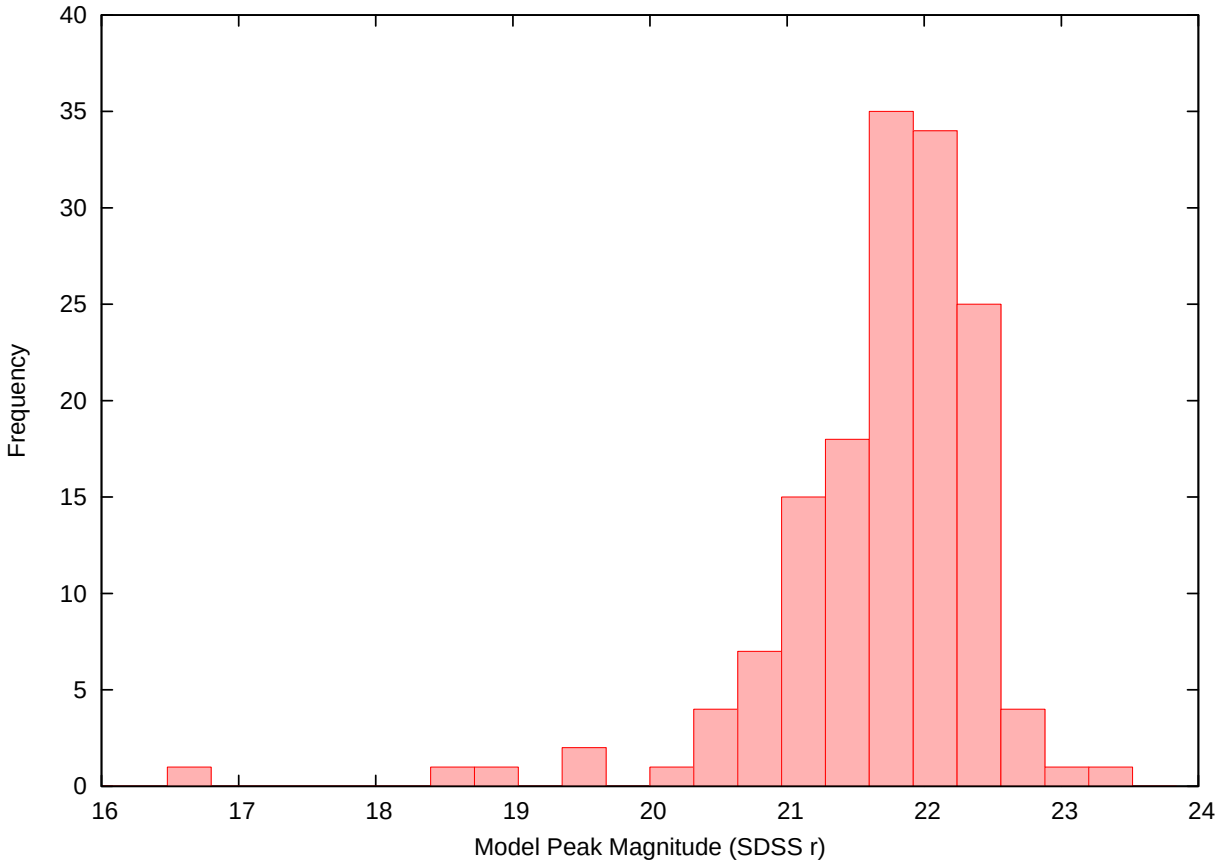

Figure 4.2: The peak apparent magnitude distribution, in SDSS r band, is shown for SN candidates excluded from the rate sample for lack of redshift information.

Thermonuclear supernovae (type Ia) must be removed from the rate sample. Fortunately, the SDSS-II supernova data pipeline is very efficient at identifying SNIa, as it was designed to collect data for SNIa cosmology. From the 2,739 candidates remaining, I then remove the 1,651 that are identified as SNIa. Table 4.1 breaks down this group by method used to identify them as SNIa. Removal of SNIa reduces the sample by a bit more than half (60.3%).

The remaining 1,088 candidates are all presumed to be core collapse supernovae for which peak luminosity occured during the 2005, 2006 or 2007 viewing season. SDSS-II could not detect the most intrinsically dim supernovae except in the region very near Earth. Because

Table 4.1: SNIa Removed from CCSN Rate Sample, by Identification Method, as defined by Sako *et al.* [31]

Identification Method (SDSS-II SEARCH TYPE)	Number of Candidates
Photometric SNIa, typed by light curve fitting (104,105)	1201
Spectroscopic SNIa, confirmed (118,120)	416
Spectroscopic SNIa, probable (119)	34
Total SNIa	1651

dim supernovae cannot be fairly sampled throughout the survey volume, I exclude them explicitly from the rate calculation. The final measurement is therefore more properly the "bright core collapse rate", however I do not emphasize this distinction, as it is implicit in all other supernova rate measurements as well.

I selected the threshold absolute magnitude of -15.0 (SDSS r), the dimmest peak magnitude that SDSS-II could detect at $z = 0.09$, according to the best fit efficiency function. Only fourteen candidates were removed by this requirement.

The final requirement selects only those candidates between redshift 0.03 and 0.09. As explained in Ch. 3.4, the region nearest Earth ($z < 0.03$) is excluded from the rate sample, to avoid systematic effects due to inhomogeneities in the density of galaxies. At the other extreme, regions too far from Earth ($z > 0.09$) are excluded, because beyond that distance SDSS-II can only detect exceptionally bright supernovae. The redshift range requirement removes 985 candidates, leaving a base rate sample of 89 core collapse supernovae.

Table 4.2 summarizes the requirement which narrow the initial, raw sample of over 10,000 light curves to the accepted, base sample of 89 CCSN.

4.2 Corrections

The SDSS-II Supernova Survey does not detect all supernovae that occur. Weather, lunar phase, proximity to other celestial objects, and many other factors can result in non-detection. To compensate for this effect, I constructed an efficiency model as described in

Table 4.2: Candidates Removed from CCSN Rate Sample, by Status and Redshift

Status	$z < 0.03$	$0.03 < z < 0.09$	$z > 0.09$	z Unknown	Total
All Candidates in RA Range	96	829	6973	2035	9933
Light Curve Fit Failed	4	21	29	8	62
Too Close to Edge of Viewing Season	5	57	349	59	470
Flatness Score Test	77	603	4014	1818	6512
Type Ia Supernova	1	48	1602	0	1651
Sub-Luminous Supernova	2	11	1	0	14
Acceptable CCSN Candidates	7	89	978	150	1224

Section 3.6. Each candidate in the rate sample is then weighted by the inverse of the survey detection efficiency, as a function of supernova peak apparent magnitude. The weighting scheme corrects the base sample count upward by 6.13 supernovae. Figure 3.15 shows the base and efficiency-corrected redshift distribution of the rate sample.

Even when viewing conditions are ideal, the survey may measure a dimmer light curve than the actual supernova luminosity, due to the extinction of light by dust in the host galaxy. This could affect the rate by shifting some candidates below the sub-luminous threshold. To compensate, the sample count is corrected according to the procedure outlined in Ch. 3.7, resulting in a second upward correction of 2.11 supernovae.

The results of efficiency and extinction corrections are summarized in Table 4.3.

Table 4.3: Corrections to the CCSN Rate Sample Size, by Reason

Reason	Adjustment	Sample Size
Base Rate Sample		89.00
Efficiency Correction	6.13	95.13
Extinction Correction	2.11	97.24
Corrected Rate Sample		97.65

4.3 Sources of Error

Statistical error in the rate is significant. Although the SDSS-II supernova survey detected a large number of core collapse supernovae, most of those detected occurred at redshift ($z > 0.09$), in a region where the CCSN luminosity range is not fairly sampled. To estimate the statistical error in the supernova count, I use the standard $\sqrt{N}$ formula for a Poisson process, *i.e.* $N = 97.65 \pm 9.88(stat)$

Systematic error arises, first of all, from uncertain detection of supernovae. While I have attempted to correct for the finite detection efficiency of the survey, and the extinction of supernova light by dust in the host galaxy, the assumptions behind these corrections may be incorrect. Therefore, I add 100% of the correction to sources of systematic error, including ± 6.13 from the efficiency correction, and ± 2.52 from the extinction correction.

The identification of supernovae based on flatness score, Λ, also may introduce systematic error. The number of confirmed AGN in the target redshift region is very small, and they may not be representative of all AGN. To estimate this error, I measure the rate at which confirmed supernovae are rejected by the flatness score requirement, and the rate at which confirmed AGN are accepted by the same requirement; 100

Though the SDSS-III BOSS data greatly improved the accuracy of redshift estimates, there are still some supernovae in the sample with only photometric redshifts. To estimate the resulting uncertainty, I compared spectroscopic and photometric redshift measurements, for those candidates where both were available. The resulting error is counted as the number of candidates that would be moved into or out of the redshift range of interest ($0.03 < z < 0.09$) when replacing the photometric value with the spectroscopic value. This yields $\pm 10\%$ systematic error in the supernova count, due to incorrect redshift.

The supernova rate is measured by the supernova count divided by survey time and volume, therefore errors in both the count and in the time and volume could contribute to the total error in the rate. However, in practice error in the time and volume is negligible compared to error in the supernova count, since space and time coordinates can be measured

quite accurately. The only exception is in the conversion of redshift to comoving distance, which is affected by uncertainty in cosmological parameters as described in Ch. 3.4, resulting in a 1.3% systematic error in the rate.

Table 4.4 summarizes the sources of statistical and systematic error, and adds them in quadrature for a total error estimate.

Table 4.4: Sources of Error in the CCSN Rate

Source of Error	Error in SN Count	Percent Error
Statistical Error ($\sqrt{N}$)	9.88	10.1%
Efficiency Correction	6.13	6.28%
Extinction Correction	2.11	2.05%
Identification by Flatness	6.22	6.37%
Photometric Redshift	10.00	10.24%
Cosmology Parameters		1.3%
All Systematic Errors		13.9%
Total Error		17.2%

4.4 Division by Survey Time and Volume

The survey volume is calculated as the difference between two sections of a sphere, each subtended by the solid angle given by the chosen limits on right ascension and declination. Because the declination range lies within 1.25° of the celestial equator, I can use the small angle approximation for $\Delta\theta$ given by:

$$V = \frac{1}{3}(\Delta\theta)(\Delta\phi)(D_{c2}^3 - D_{c1}^3) \tag{4.1}$$

where D_{c1} and D_{c2} are the comoving distances at $z = 0.03$ and $z = 0.09$, respectively. This calculation yields a survey volume of $1.373 \times 10^6 Mpc^3$. As discussed in Ch. 3.4, uncertainty in cosmological parameters introduces an error in the calculated volume, which must be propagated into the systematic error on the rate.

The survey time is counted as the number of days where a supernova could have peak luminosity, and be included in the rate measurement if detected. This is just the number of days in the three viewing seasons for 2005, 2006, and 2007, minus the first and last ten days of each season. The Julian date ranges included are shown in Table 4.5, summing to a total survey time of 264 days, or 0.723 years.

Table 4.5: Survey Time Ranges Included in CCSN Rate Measurement

Viewing Season	Julian Date Range (last 5 digits)	Days
2004	53622 - 53705	83
2005	53974 - 54068	94
2006	54346 - 54433	87
Total		264

When counting supernova that occurred during the survey time range, a systematic error may be introduced by incorrectly measuring the peak time. Light curves only have data recorded every two days, at best, therefore the light curve fit may incorrectly judge the time of maximum luminosity. To measure error due to this effect, I divided each viewing season into two halves; the difference in supernova count between the two halves was 5.5, with an average of 44.5 superovae in each half. This is within the bounds of statistical fluctuation, since $5.5 < \sqrt{(44.5)}$, therefore I conclude that additional, systematic error to to time uncertainty is negligible.

The final rate calculation is just the supernova count, divided by the survey time and volume. A factor of h_{70}^3 is included in the rate units, to reflect the fact that this rate measurement, like all supernova rate measurements in the literature, scales with the Hubble constant, H_0, with value unity at $H_0 = 70$km/sec/Mpc. The final rate is given by:

$$\rho_{\mathrm{CCSN}} = \frac{97.24\mathrm{CCSNe}}{1.37 \times 10^6 \mathrm{Mpc}^3 \times 0.723\mathrm{yr}} = 9.79 \pm 1.37(stat) \pm 1.21(sys) \times 10^{-5} \frac{h_{70}^3}{\mathrm{Mpc}^3\mathrm{yr}} \quad (4.2)$$

Chapter 5

Conclusion

5.1 Comparison with Prior Measurements

To compare my core collapse rate result with other measurements in the literature, I must first relate it to cosmic history. It is known that the star formation rate has evolved throughout the history of the universe [40]. Because the rate at which massive stars are created is time-dependent, the rate at which massive stars are destroyed must also be time-dependent. Therefore, the core collapse supernova rate is not a universal constant, but a function of time.

Any astronomical observation has an inherent time delay, due to the finite speed at which light propagates from the source to Earth. In extragalactic astronomy, this lookback time is very well correlated with an object's cosmic redshift, according to the Hubble law. Because my CCSN rate sample spans a range of redshifts, it also spans a range of cosmic history. The number of CCSN in the sample, divided by time and volume, is an average over this time range, not an instantaneous rate.

In order to compare my result to previous CCSN rate measurements, it is useful to find the approximate redshift at which the average redshift over the entire bin is equal to instantaneous CCSN rate. I refer to this matching redshift as z_{match}. To determine z_{match}, I

fit the observed CCSN density vs. redshift to a polynomial in z, then find the root, z_{match} of the following equation:

$$\rho_{fit}(z_{match}) = \frac{1}{V}\int_{z=0.03}^{z=0.09} \rho_{fit}(z)\mathrm{dV} \tag{5.1}$$

The fitting procedure is derived from a polynomial expansion of the unknown rate function, truncated at a finite order, n, where the correction, z^n, is assumed to be negligible. Expanding in a Taylor series about z_0, the mean redshift of the CCSN rate sample, the series has the form:

$$\mathrm{dN_{CCSN}} = (\sum_{k=0}^{n} a_k(z-z_0)^k)\mathrm{dV} \tag{5.2}$$

Equation 5.2 alone is not sufficient to solve for the unknown coefficients, a_k. However, by multiplying both sides by a factor of $(z-z_0)^n$, then integrating, I derive an independent equation for each a_k:

$$\int_{z=0.03}^{z=0.09} (z-z_0)^n \mathrm{dN_{CCSN}} = \sum_{k=0}^{n} a_k \int_{z=0.03}^{z=0.09} (z-z_0)^{n+k}\mathrm{dV} \tag{5.3}$$

Solving for the nth coefficient, a_n, yields:

$$a_n = \frac{\int_{z=0.03}^{z=0.09}(z-z_0)^n \mathrm{dN_{CCSN}} - \sum_{k=0}^{n-1} a_k \int_{z=0.03}^{z=0.09}(z-z_0)^{n+k}\mathrm{dV}}{\int_{z=0.03}^{z=0.09}(z-z_0)^{2n}\mathrm{dV}} \tag{5.4}$$

To find the best fit coefficients, a_k, I first set a_0 to the average rate over the entire bin. For each successive a_n, I then apply Equation 5.4 using all lower order coefficients that have already been determined. Table 5.1 displays the results of this calculation. Terms higher than quadratic order in $(z-z_0)$ are negligible compared to statistical error, therefore I use the quadratic approximation of this series to solve for the matching redshift, $z_{match} = 0.083$.

Figure 5.1 shows my result, and CCSN rate measurements from the literature, on a logarithmic scale in both rate and $(1+z)$, where z is the cosmic redshift. The expression

Table 5.1: Polynomial Expansion of CCSN Rate vs. Redshift

Order	Coefficient (a_n)	Series Term ($a_n(z_{match} - z_0)^n$) $\times 10^{-4}$	Percent of Avg. Rate
$(z - z_0)^0$	0.00006478	0.6478	100%
$(z - z_0)^1$	0.000850	0.0905	14.0%
$(z - z_0)^2$	-0.0678	-0.0768	11.9%
$(z - z_0)^3$	-1.134	-0.0137	2.1%
$(z - z_0)^4$	-5.954	-0.0008	0.1%

$(1 + z)$ is chosen to fit a commonly used phenomenological form, $\rho_{\mathrm{CCSN}} = \rho_0(1 + z)^\alpha$ [40] to the combined rate measurements. Minimization of chi-squared finds $\alpha = 3.6 \pm 1.4$ and $\rho_o = 7.5 \pm 0.2 \times 10^{-5} h_{70}^3 \mathrm{Mpc}^{-3}\mathrm{yr}^{-1}$. The Cappellaro *et al.* result of 1999 is excluded from the fit, due to suspected underestimation of error in that pioneering study.

My result is generally consistent with the trend identified in earlier CCSN surveys, but provides coverage in a redshift range not previously measured. This is somewhat analogous to the "redshift desert" in SNIa surveys that SDSS-II was designed to probe.

5.2 Implications for Star Formation

The core collapse rate is closely related to the star formation rate, because the massive stars that undergo core collapse are relatively short lived. A star with eight times the Sun's mass, about the minimum mass for a CCSN progenitor, has a main sequence lifetime of about 55 million years [42]. At ($z = 0.07$), that is only 5.7 percent of the time it takes a galaxy's light to reach Earth, and more massive stars than that have even shorter lifetimes. The core collapse rate is therefore a good indicator of cosmic star formation history, following the star formation rate to within a few percent of the lookback time.

The cosmic star formation rate can be independently measured using galaxy spectra, and follows a phenomenological rate law proportional to $(1 + z)^{3.4}$. This is consistent with the best fit exponent $a = 3.6 \pm 1.4$ shown in Figure 5.1.

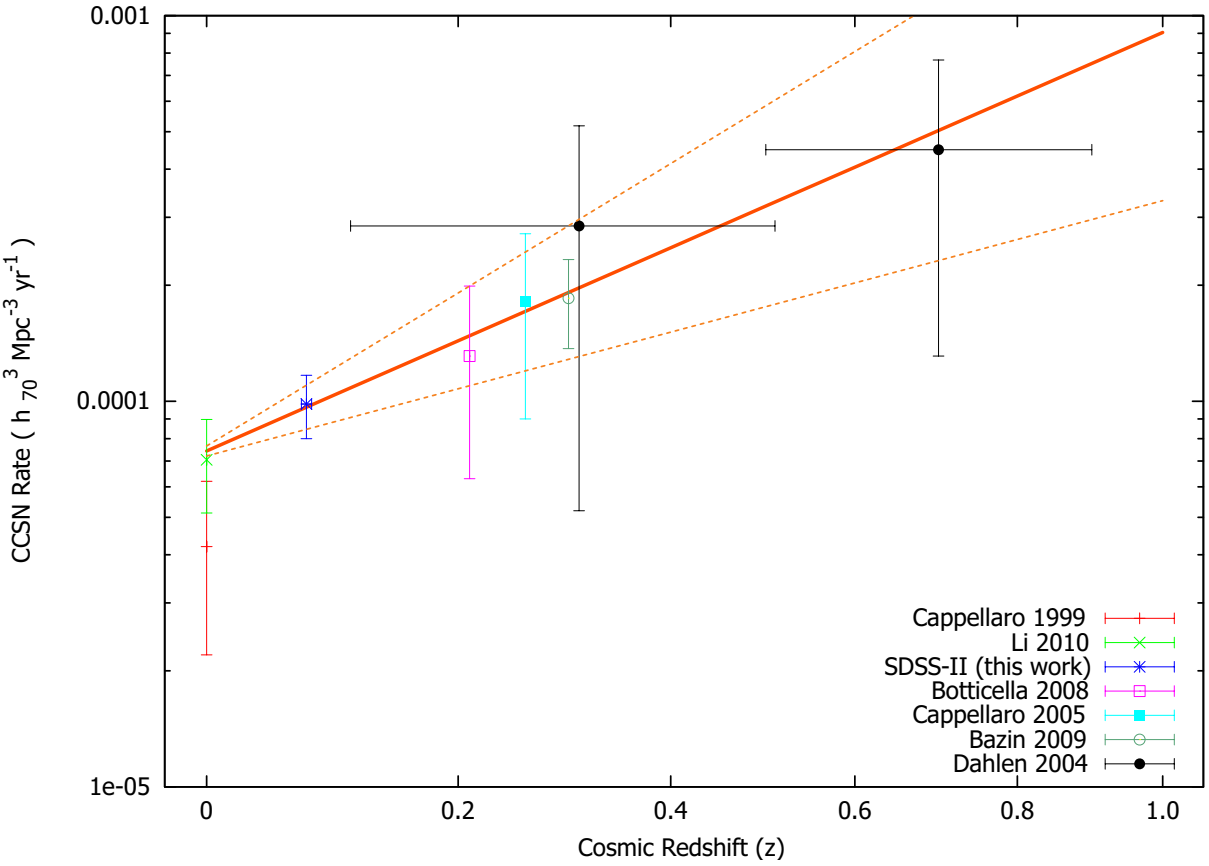

Figure 5.1: The CCSN rate measurement from this work is shown with previous CCSN rate measurements in the literature, as given by Horiuchi et al. [40] The solid line is the best fit to $\rho = \rho_0(1+z)^a$, with dashed lines indicating uncertainty. The blue shaded region and nearby points represent the star formation rate estimated primarily from the UV galaxy luminosity data of Baldry et al. [41].

As expected, the core collapse rate is proportional to the star formation rate. However, the constant of proportionality is not consistent with stellar population models, as discovered by Horiuchi it et al. [40]. They found that the observed CCSN rate falls short of the prediction from the star formation rate by approximately a factor of two. Figure 5.2, taken from their paper and updated to include the present work, shows this discrepancy.

Horiuchi *et al.* frame the disagreement between star formation and CCSN rates as a "supernova rate problem", a gap in our current understanding of stellar evolution. Either we have only observed half of all CCSN that actually occur, our models of the stellar mass distribution are flawed, or a portion of massive stars have a fate other than to explode as a CCSN.

5.3 The CCSN Luminosity Function

With the SDSS-II supernova data, I can explore one aspect of the problem raised by Horiuchi, the number of CCSN not observed because they are too dim. Horiuchi divides CCSN into two categories, bright and faint. Bright CCSN are those with absolute V magnitude of -15.0 or brighter. The V or visual band refers to the Johnson filter system, and is roughly similar to the SDSS r band. An object's absolute magnitude, M, is related to its redshift, z, and apparent magnitude, m, as follows:

$$m = M + \mu(z) \tag{5.5}$$

The quantity, $\mu(z)$, is known as the distance modulus, a logarithmic measure of the object's distance. The formula for distance modulus as a function of redshift is:

$$\mu(z) = 43.16 + 5\log_{10}(\frac{z^2 + 2z}{z^2 + 2z + 2}) \tag{5.6}$$

Equation 5.6 makes a somewhat simplistic assumption of perfectly flat cosmology, in order

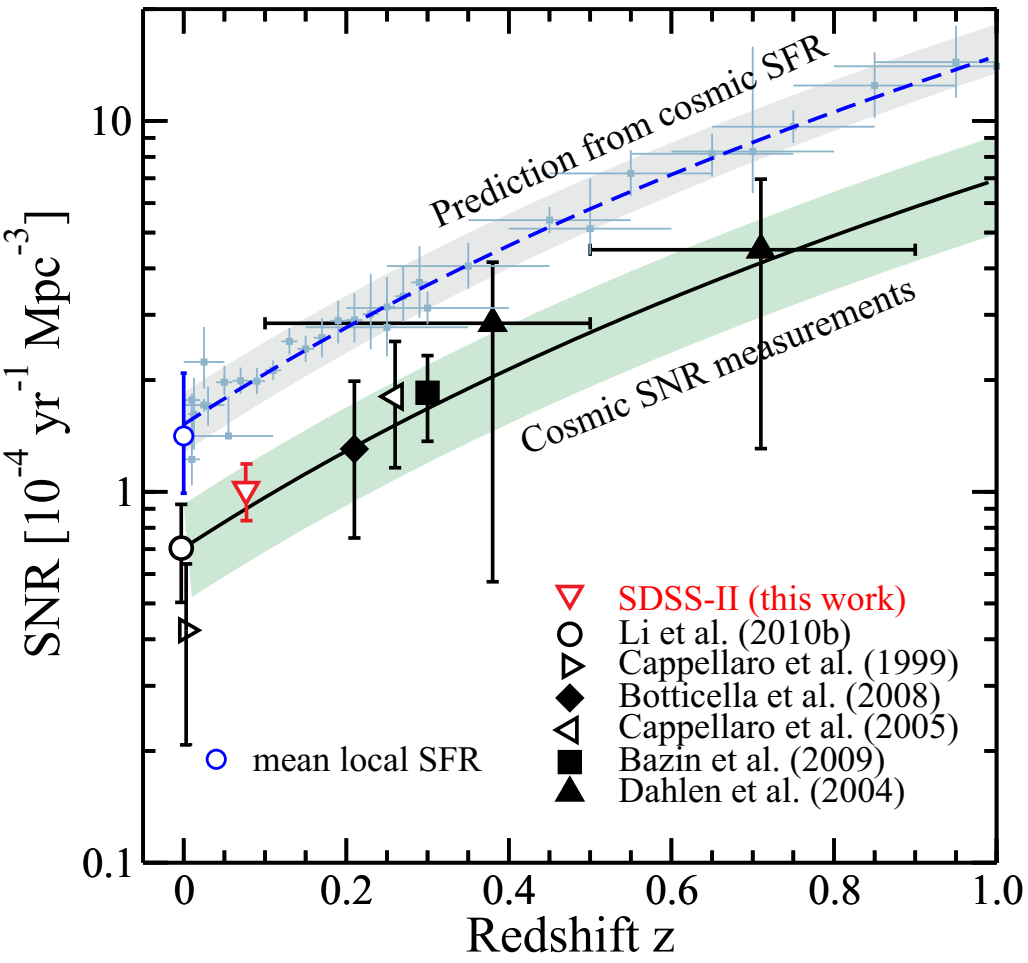

Figure 5.2: Historical CCSN rate and star formation rate measurements, from Horiuchi *et al.* [40], are updated with results from this work.

to reduce the complexity of the calculation. However, it is within 0.24 magnitudes of the value predicted by standard ΛCDM cosmology for a redshift of $z = 0.09$. Of the supernova candidates in my core collapse rate sample, there are none which would be demoted to the "subluminous" category by a shift of 0.24 magnitudes, and vice versa, therefore I conclude that cosmological uncertainty in absolute magnitude affects the rate measurement negligibly, compared to other sources of error.

Figure 5.3 shows the efficiency-weighted absolute magnitude distribution of my CCSN rate sample, plus those candidates excluded only because of they were too faint or were too near Earth. This distribution is also known as the core collapse supernova luminosity function. Error on each bin count is estimated as $\sqrt{N}$ assuming supernovae are a Poisson process, added in quadrature with the 13.9 percent systematic error found for the supernova count in Chapter 4.

In Figure 5.3, we see that subluminous supernovae are underrepresented in the full rate sample, because they are only detected when relatively near Earth. To estimate the actual rate of subluminous supernovae, I examine the subsamples for $z < 0.06$ and $z < 0.03$. The subluminous fractions in these ranges are 20 percent and 24 percent respectively. Statistics are too low to regard these figures as conclusive, but they do suggest that a subluminous fraction of 50 percent, the number required to solve Horiuchi's rate problem, is unlikely.

5.4 Potential for Future Measurements

Future astronomical survey instruments, such the Large Synoptic Survey Telescope (LSST) [43], promise orders of magnitude increase in the number of supernovae observed, including core collapse supernovae. While this will greatly reduce statistical error, systematic error is likely to remain comparable to present day surveys, especially because only a fraction of such events will have spectroscopic redshift measurements. Therefore, the CCSN rate measurements themselves may not be much more accurate than today.

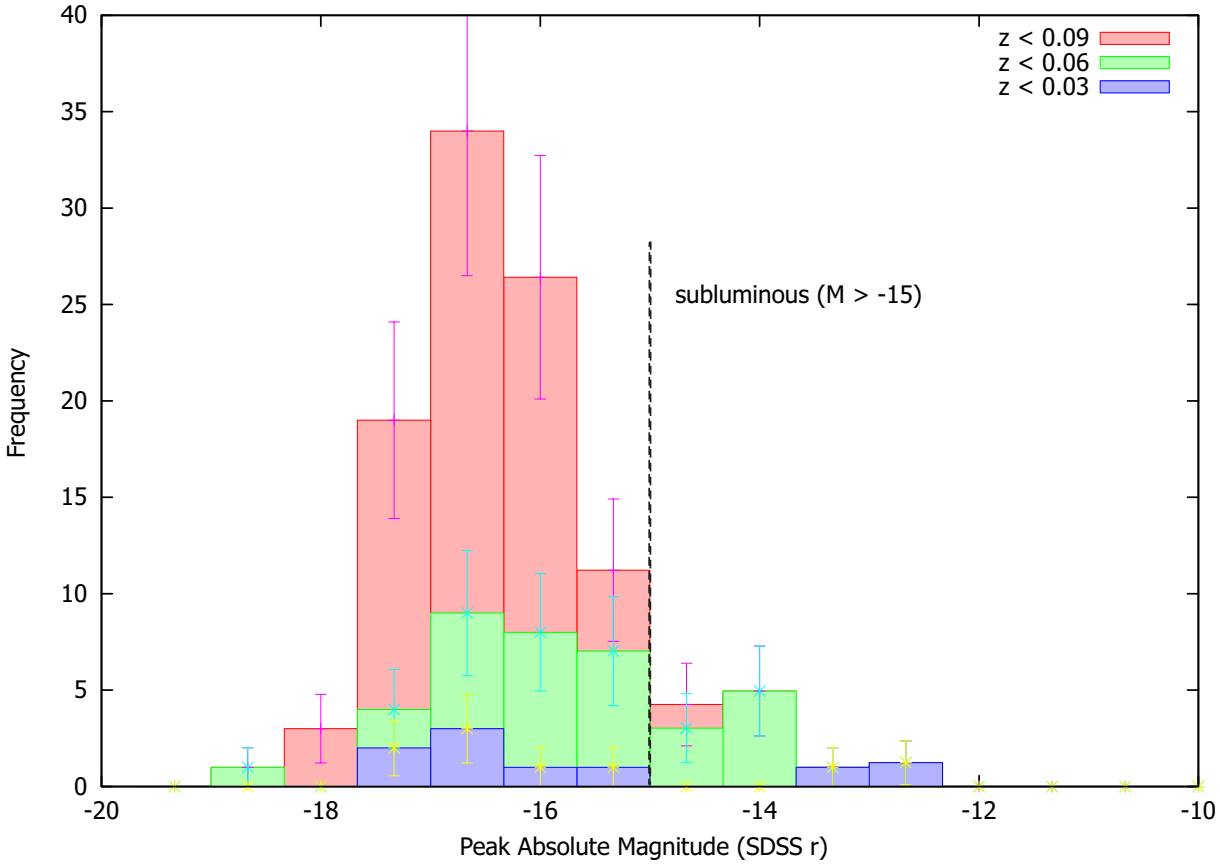

Figure 5.3: A CCSN luminosity function is derived for the rate sample in this work, plus candidates excluded only because they were faint or too near Earth.

On the other hand, greater statistics will be very important in better measuring the rate of subluminous CCSN, a crucial factor in solving Horiuchi's supernova rate problem. Also, the increased statistics will be invaluable in more complex supernova measurements, like understanding the distribution of various supernova characteristics within the CCSN population, and correlating CCSN rate and characteristics with properties of the host galaxy, and location within the galaxy.

In the meantime, the CCSN rate problem can be attacked from the other direction, by investigating hypothetical modes of stellar death other than a CCSN explosion. For example, a measurement of the local neutron star and black hole birth rates could show whether some of the "missing" massive stars end their lives through direct formation of black holes, with no accompanying bright explosion. Or perhaps, as Horiuchi speculates, the CCSN rate problem will one day be solved by a major rethinking of stellar evolution and supernova physics.

Appendix A: Rate Sample Light Curves

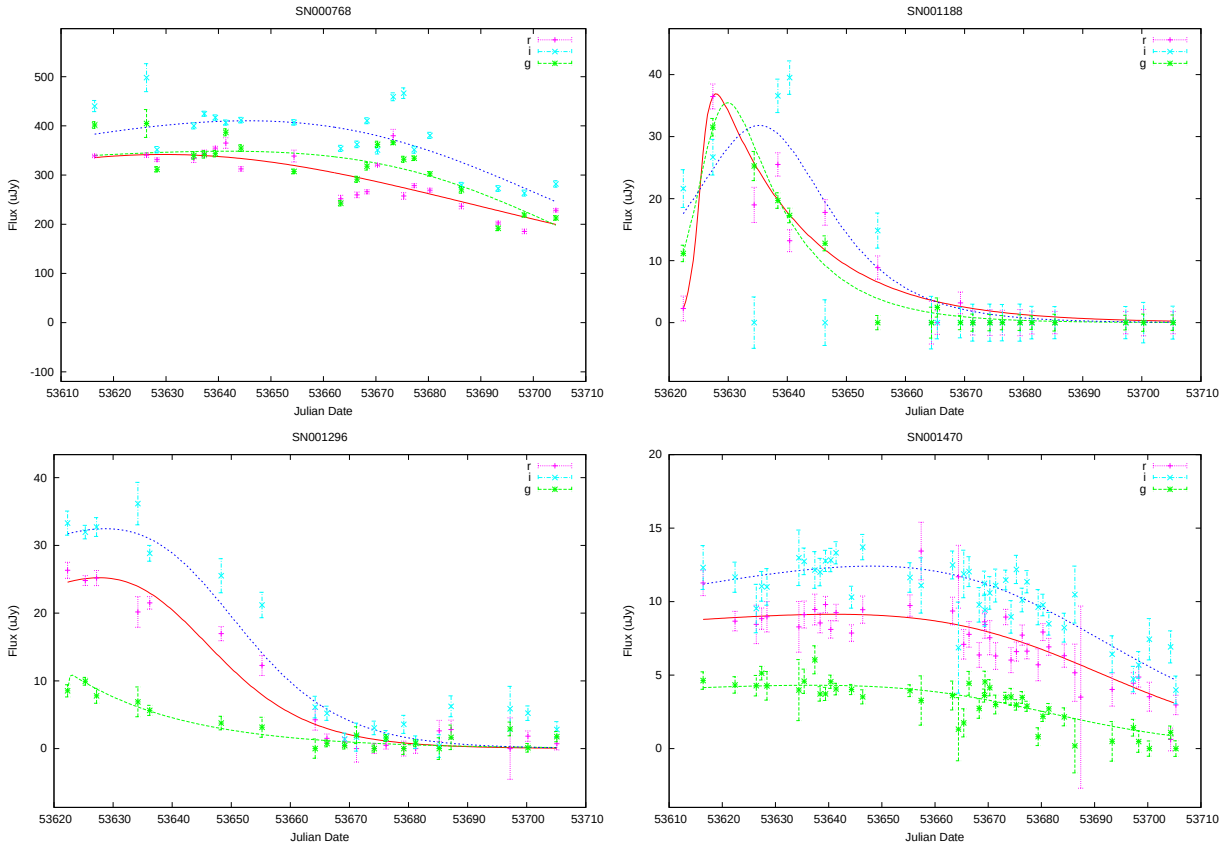

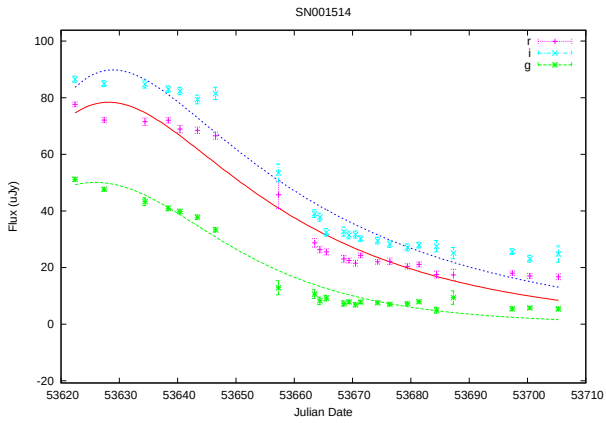
SN001514
Flux (uJy)
Julian Date
r
i
g

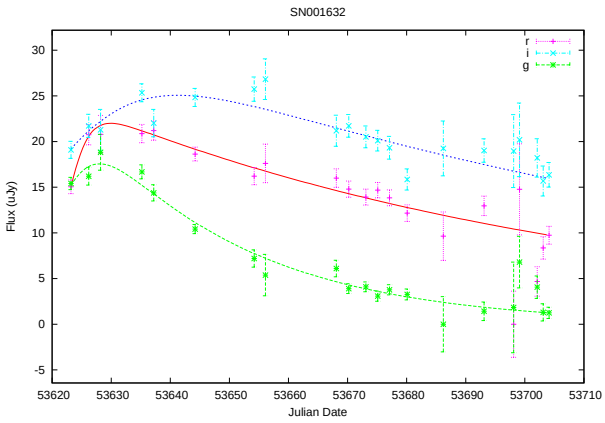
SN001632
Flux (uJy)
Julian Date
r
i
g

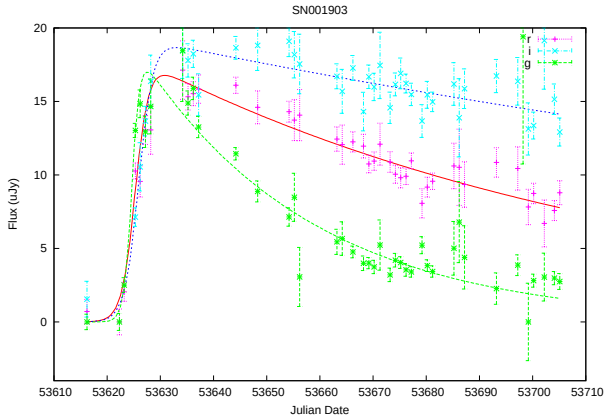
SN001903
Flux (uJy)
Julian Date
r
i
g

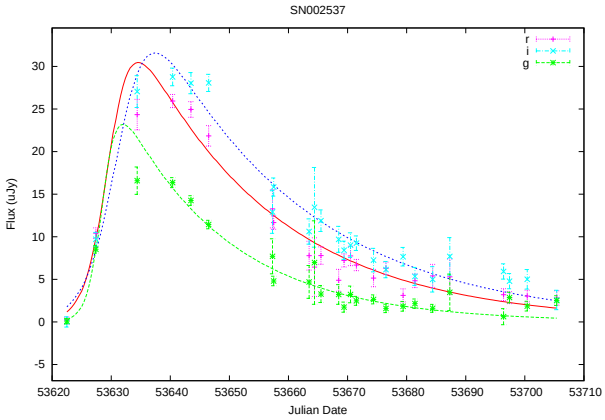
SN002537
Flux (uJy)
Julian Date
r
i
g

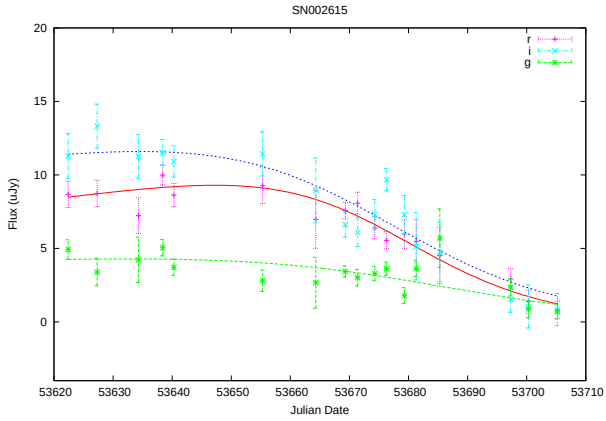
SN002615
Flux (uJy)
Julian Date
r
i
g

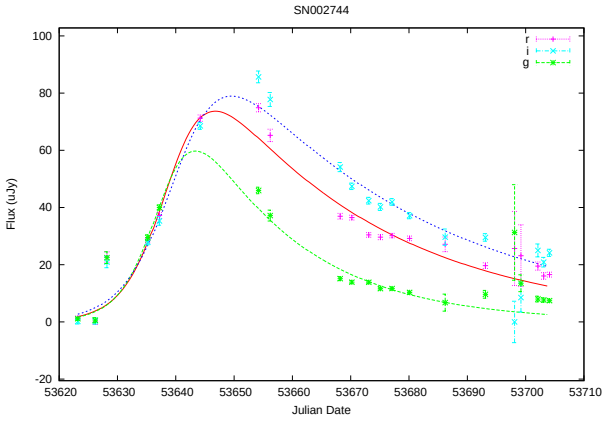
SN002744
Flux (uJy)
Julian Date
r
i
g

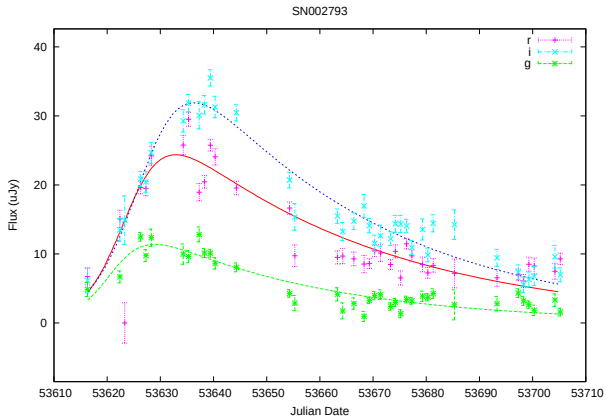
SN002793
Flux (uJy)
Julian Date
r
i
g

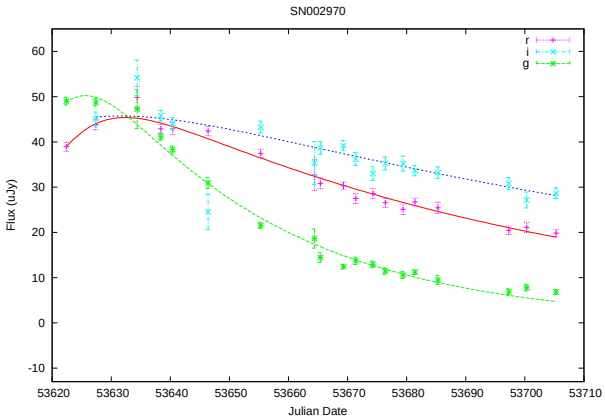
SN002970
Flux (uJy)
Julian Date
r
i
g

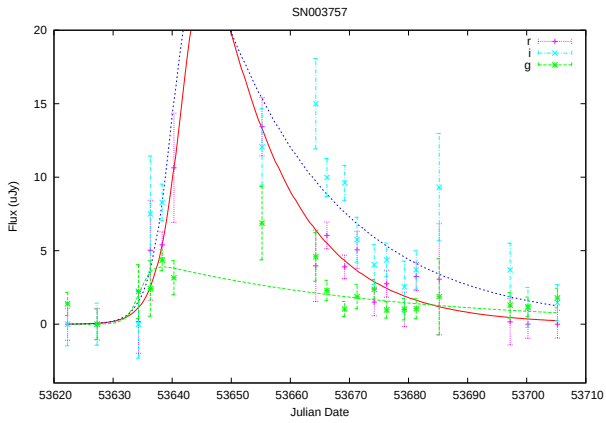
SN003757
Flux (uJy)
Julian Date
r
i
g

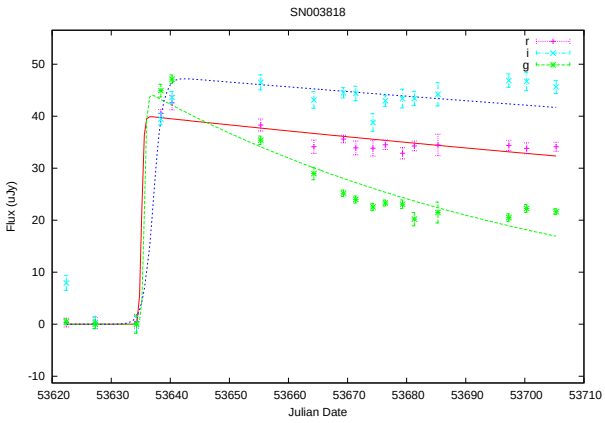
SN003818
Flux (uJy)
Julian Date
r
i
g

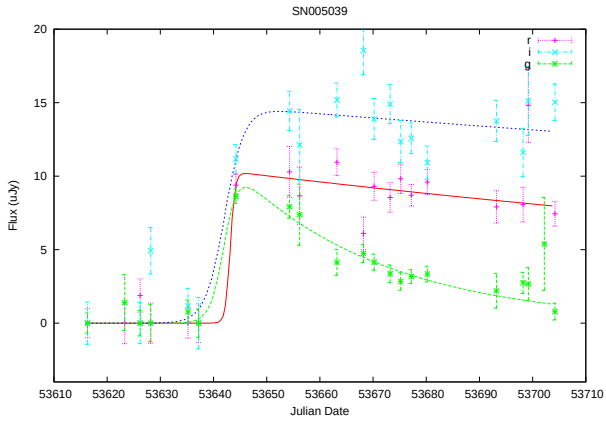
SN005039
Flux (uJy)
Julian Date
r
i
g

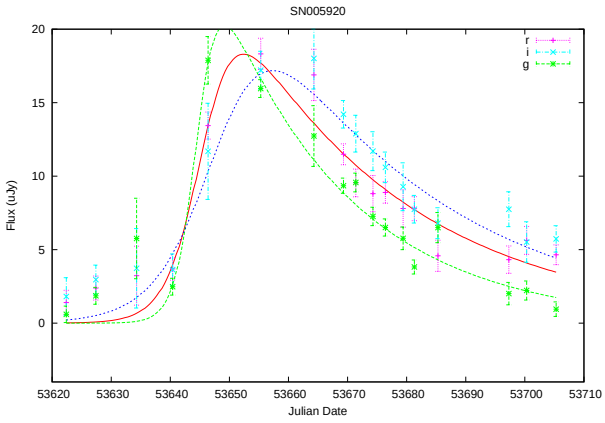
SN005920
Flux (uJy)
Julian Date
r
i
g

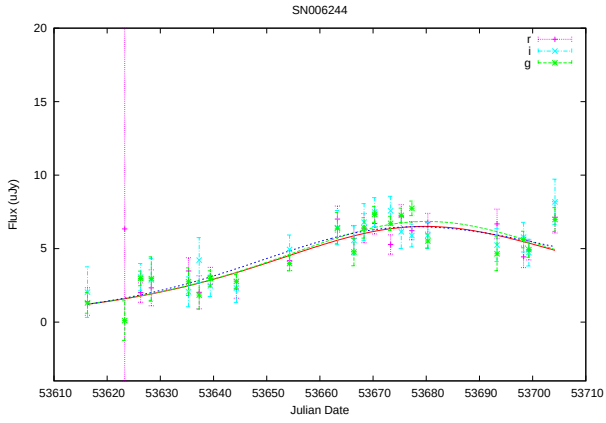
SN006244
Flux (uJy)
Julian Date
r
i
g

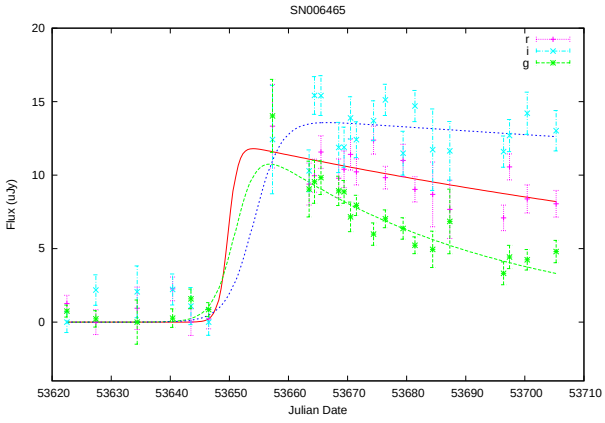
SN006465
Flux (uJy)
Julian Date
r
i
g

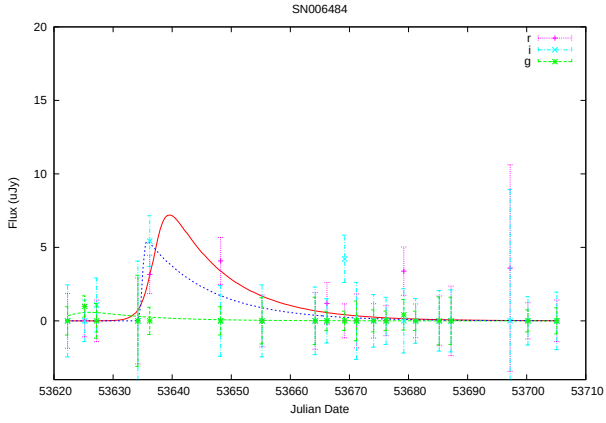
SN006484
Flux (uJy)
Julian Date
r
i
g

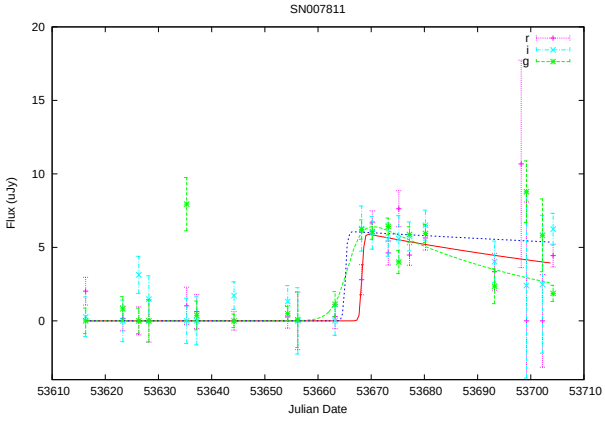
SN007811
Flux (uJy)
Julian Date
r
i
g

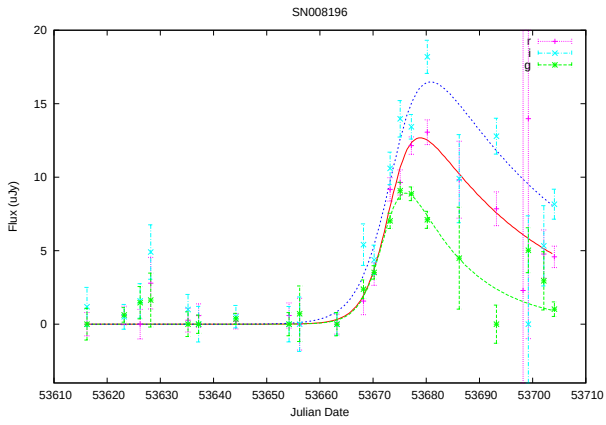
SN008196
Flux (uJy)
Julian Date
r
i
g

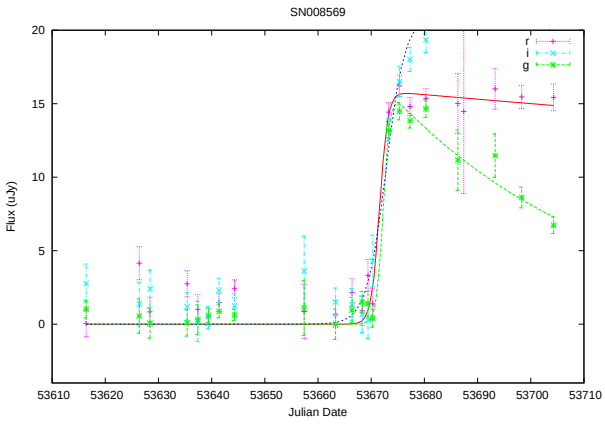
SN008569
Flux (uJy)
Julian Date
r
i
g

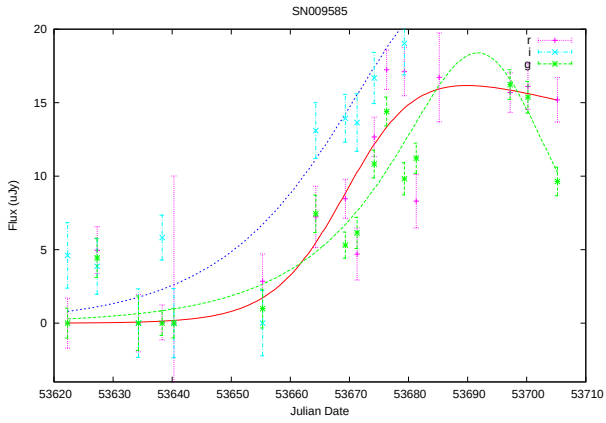
SN009585
Flux (uJy)
Julian Date
r
i
g

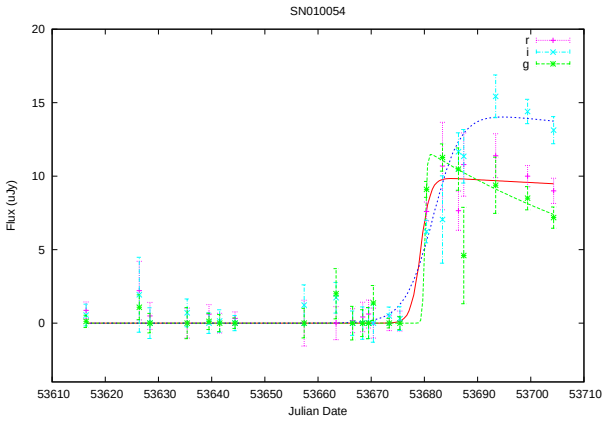
SN010054
Flux (uJy)
Julian Date
r
i
g

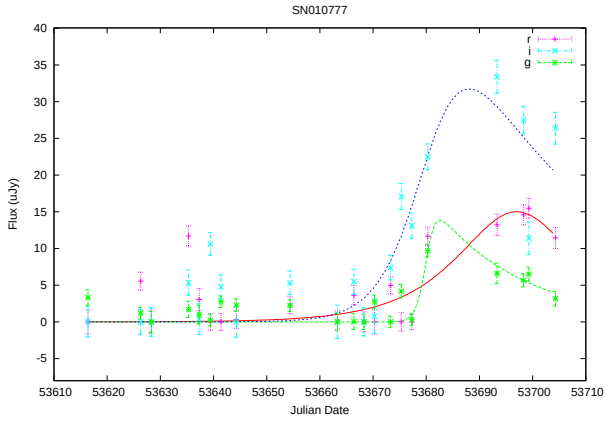
SN010777
Flux (uJy)
Julian Date
r
i
g

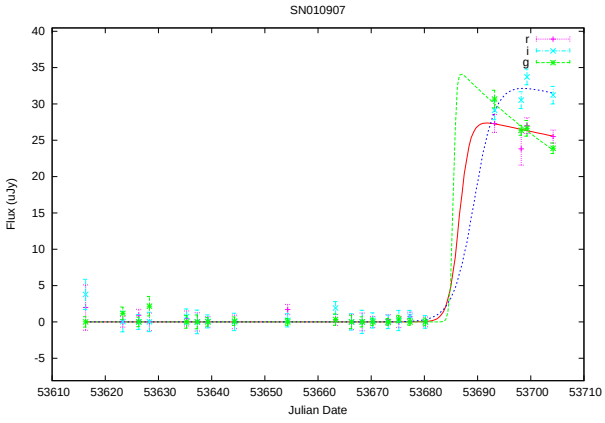
SN010907
Flux (uJy)
Julian Date
r
i
g

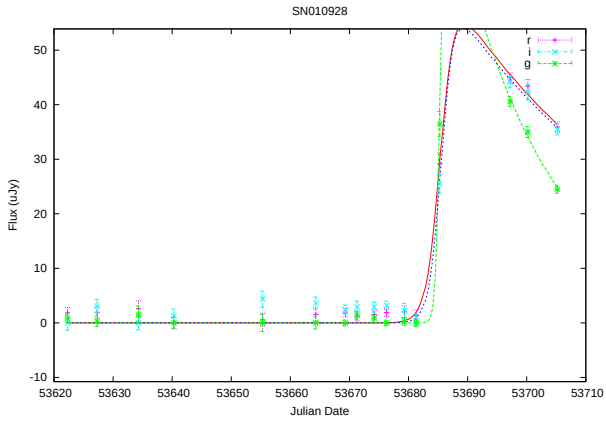
SN010928
Flux (uJy)
Julian Date
r
i
g

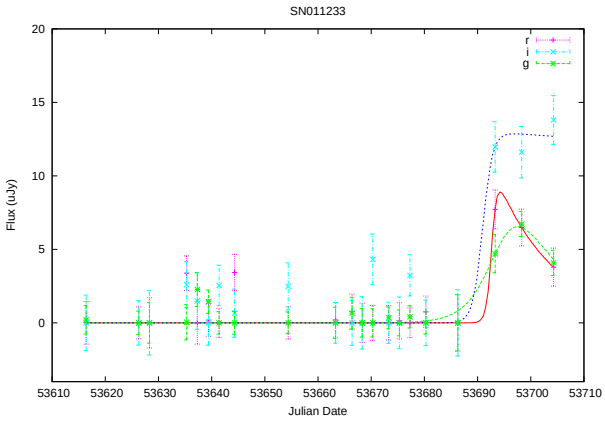
SN011233
Flux (uJy)
Julian Date
r
i
g

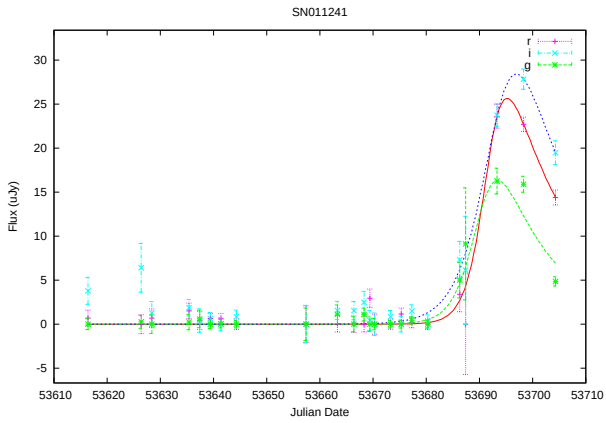
SN011241
r
i
g
Flux (uJy)
Julian Date

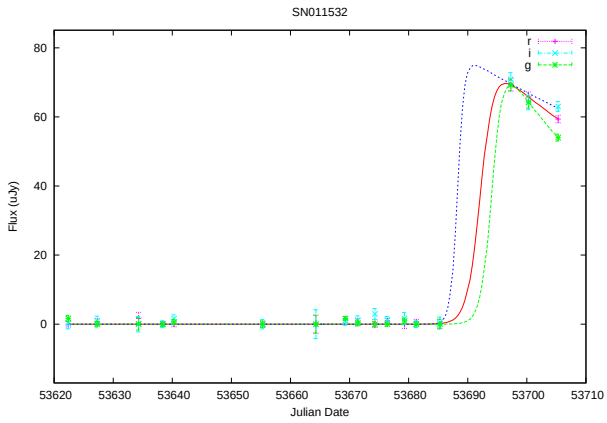
SN011532
r
i
g
Flux (uJy)
Julian Date

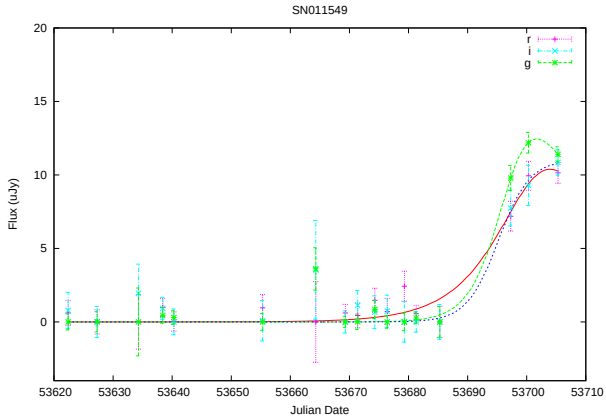
SN011549
r
i
g
Flux (uJy)
Julian Date

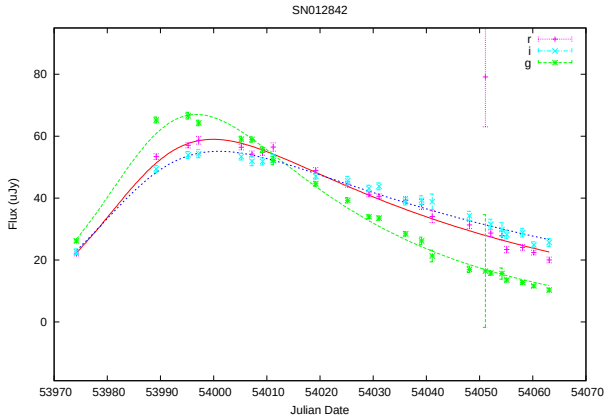
SN012842
r
i
g
Flux (uJy)
Julian Date

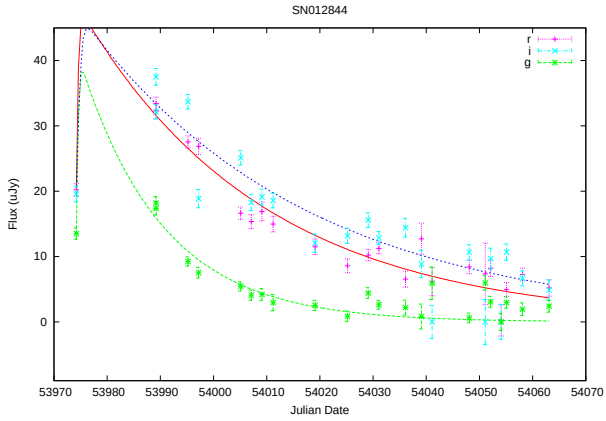
SN012844
r
i
g
Flux (uJy)
Julian Date

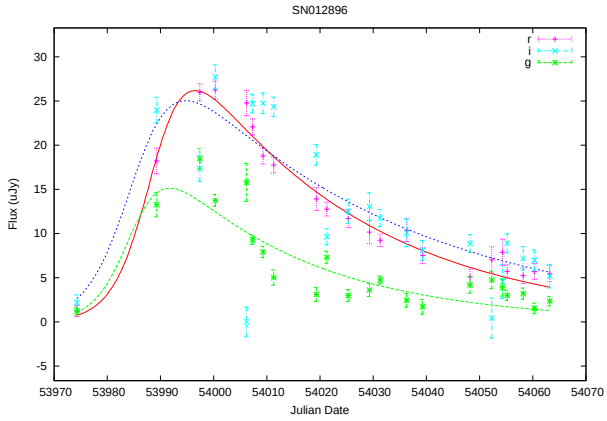
SN012896
r
i
g
Flux (uJy)
Julian Date

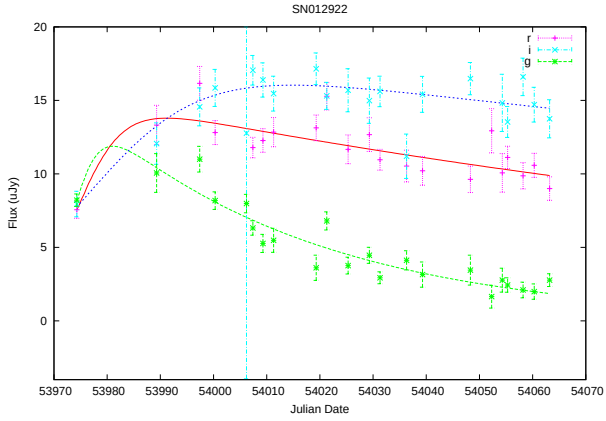
SN012922
r
i
g
Flux (uJy)
Julian Date

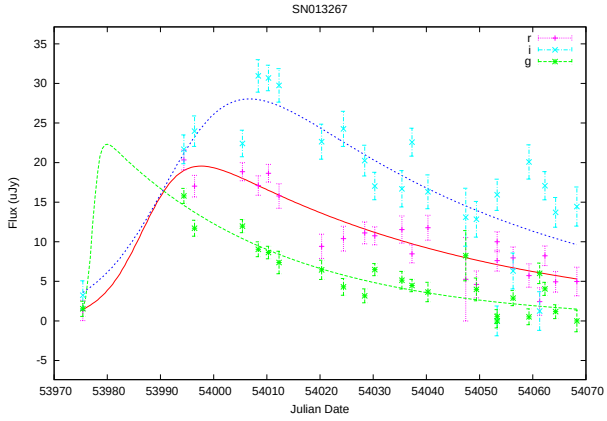
SN013267
r
i
g
Flux (uJy)
Julian Date

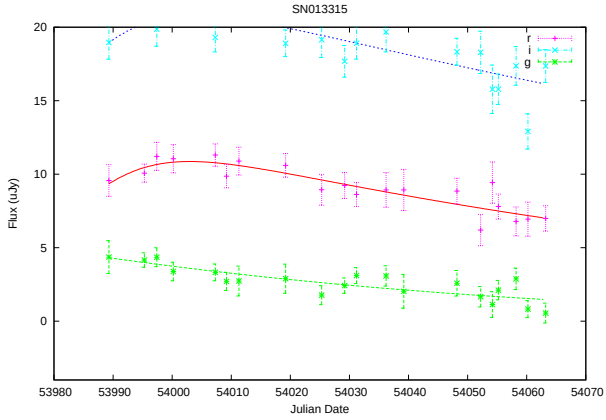
SN013315
Flux (uJy)
Julian Date
r
i
g

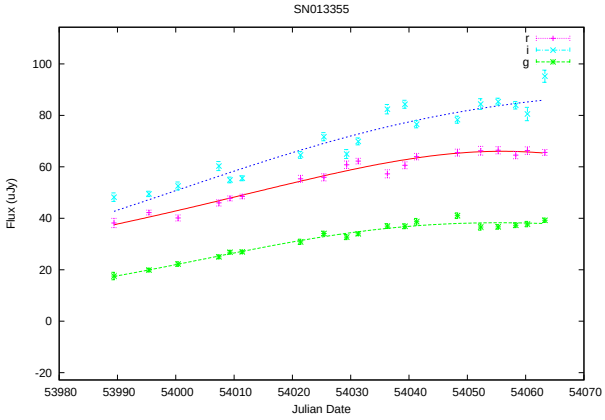
SN013355
Flux (uJy)
Julian Date
r
i
g

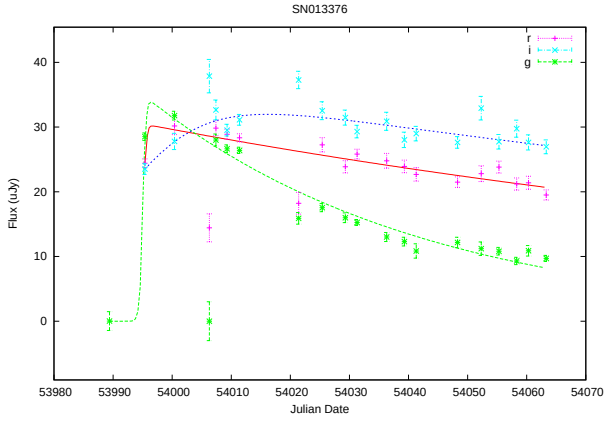
SN013376
Flux (uJy)
Julian Date
r
i
g

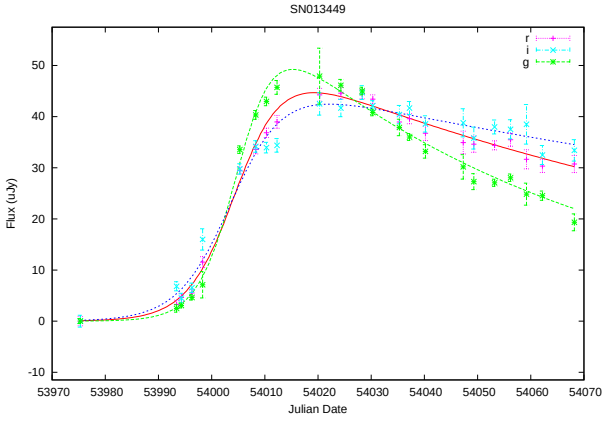
SN013449
Flux (uJy)
Julian Date
r
i
g

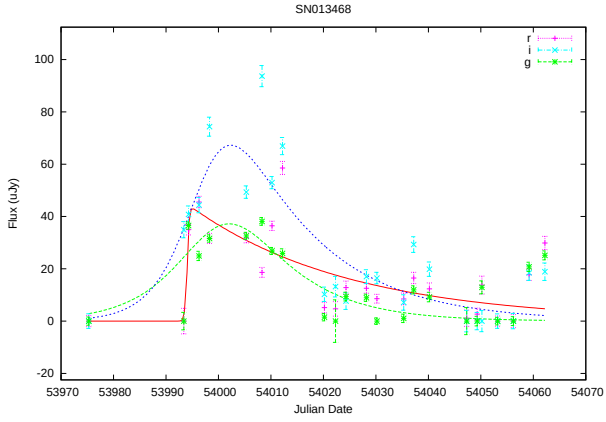
SN013468
Flux (uJy)
Julian Date
r
i
g

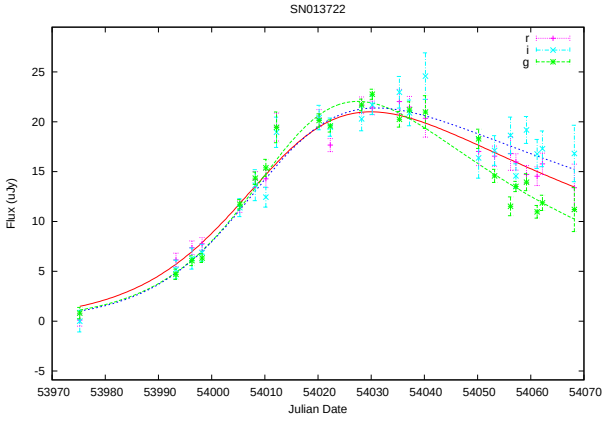
SN013722
Flux (uJy)
Julian Date
r
i
g

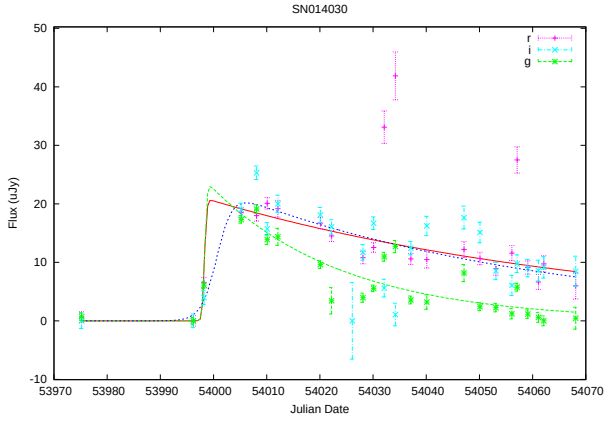
SN014030
Flux (uJy)
Julian Date
r
i
g

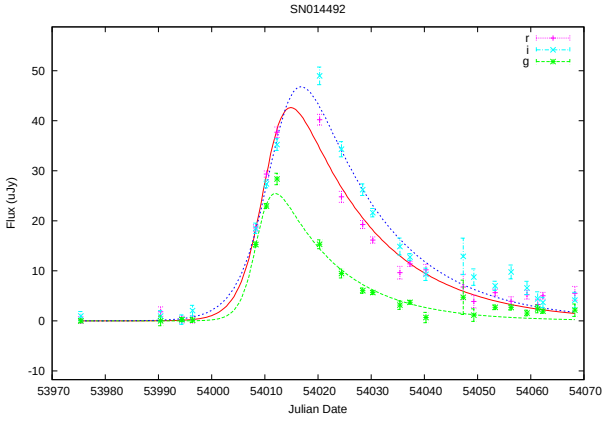
SN014492
Flux (uJy)
Julian Date
r
i
g

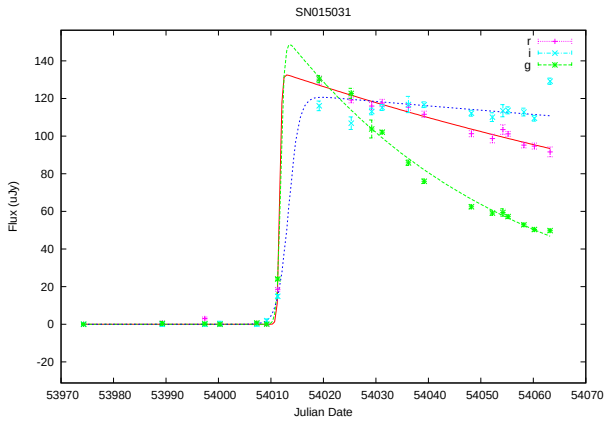
SN015031
Flux (uJy)
Julian Date
r
i
g

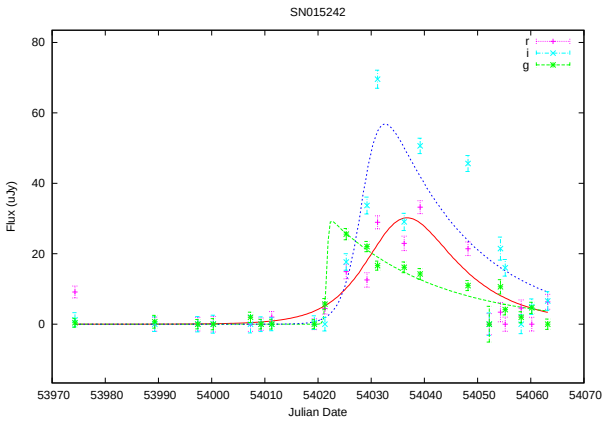
SN015242
Flux (uJy)
Julian Date
r
i
g

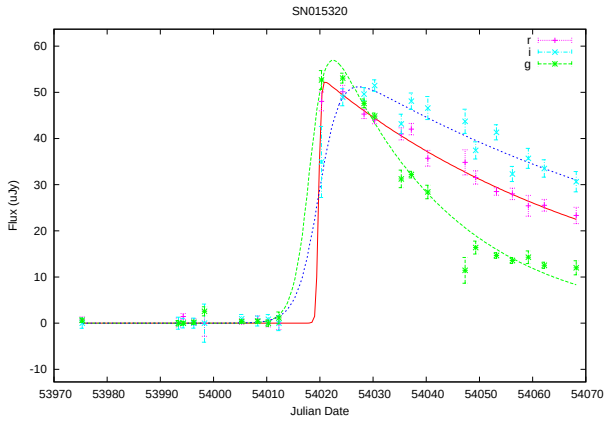
SN015320
Flux (uJy)
Julian Date
r
i
g

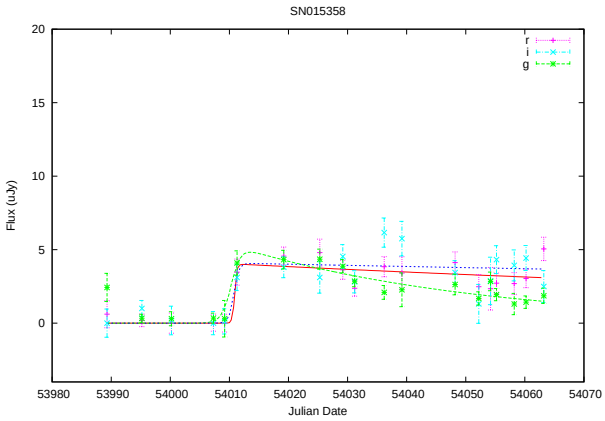
SN015358
Flux (uJy)
Julian Date
r
i
g

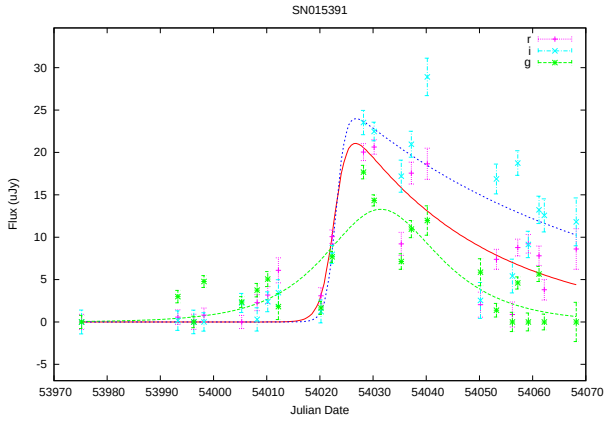
SN015391
Flux (uJy)
Julian Date
r
i
g

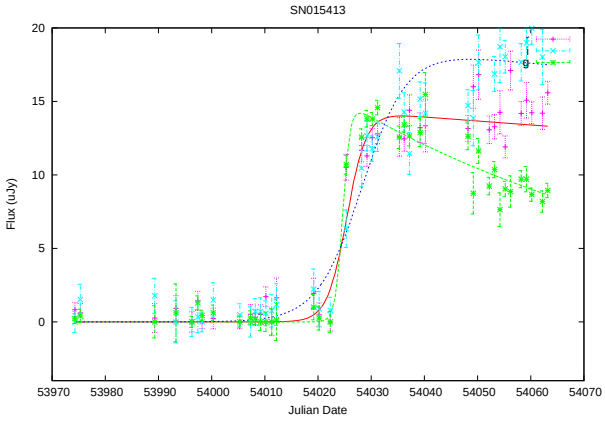
SN015413
Flux (uJy)
Julian Date
r
i
g

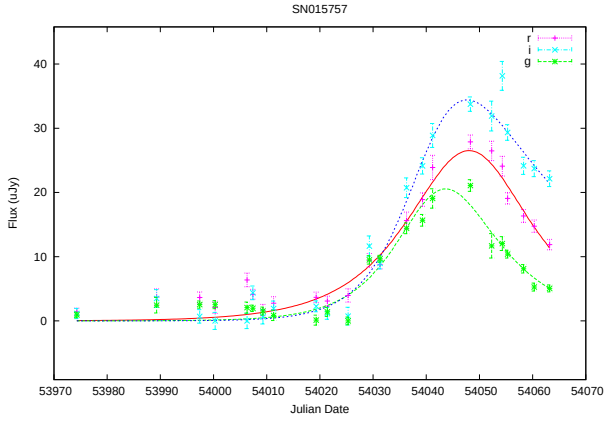
SN015757
Flux (uJy)
Julian Date
r
i
g

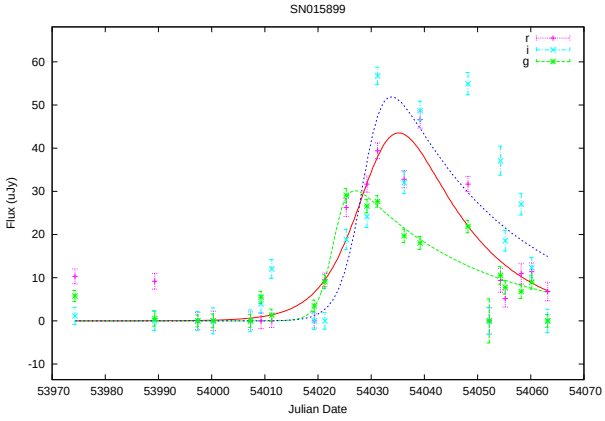
SN015899
Flux (uJy)
Julian Date
r
i
g

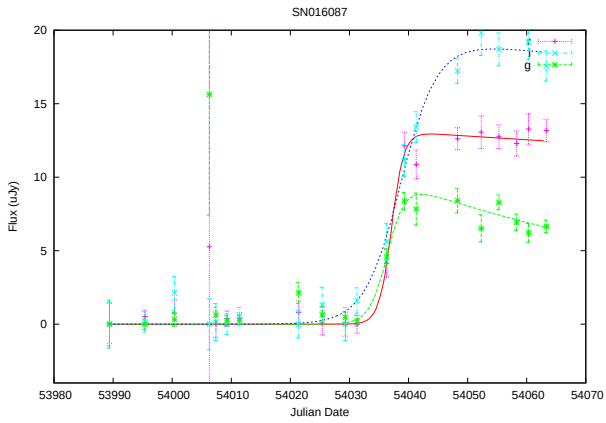
SN016087
Flux (uJy)
Julian Date
r
i
g

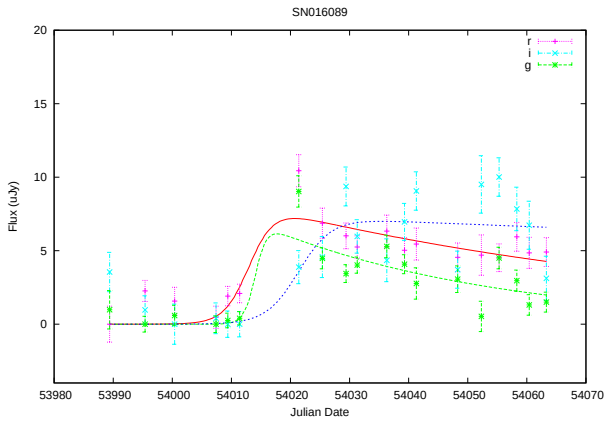
SN016089
Flux (uJy)
Julian Date
r
i
g

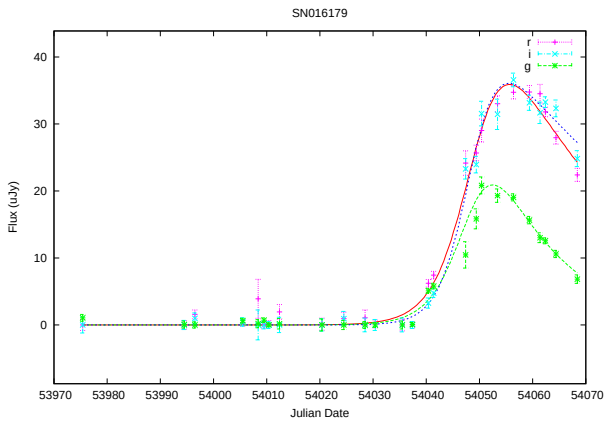
SN016179
Flux (uJy)
Julian Date
r
i
g

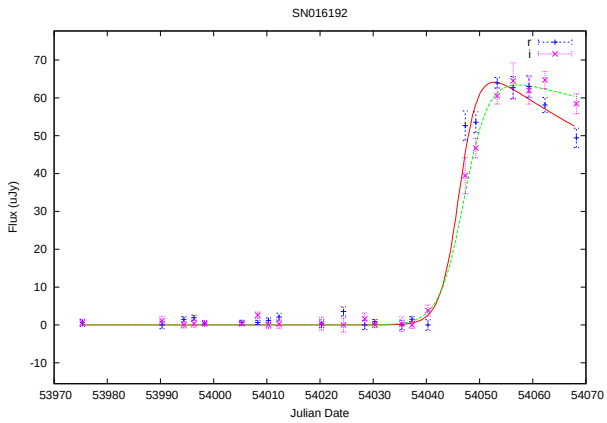
SN016192
Flux (uJy)
Julian Date
r
i

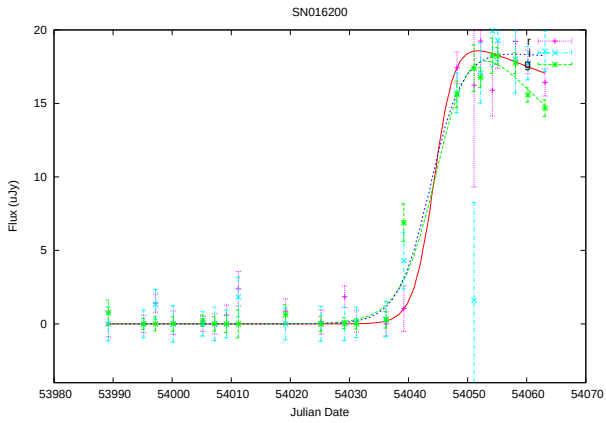
SN016200
Flux (uJy)
Julian Date
r
i
g

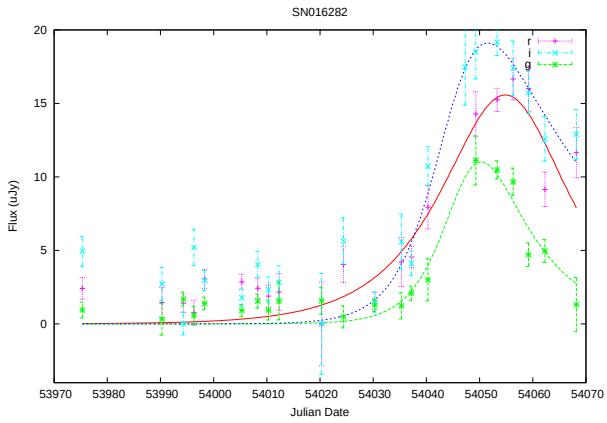
SN016282
Flux (uJy)
Julian Date
r
i
g

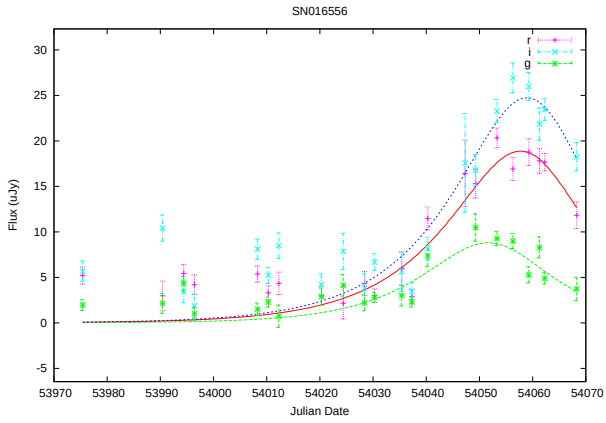
SN016556
Flux (uJy)
Julian Date
r
i
g

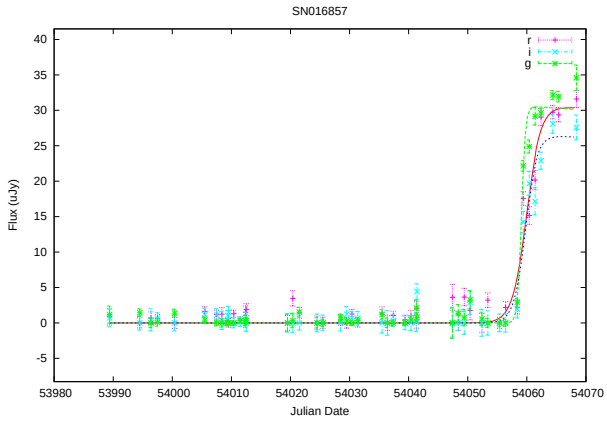
SN016857
Flux (uJy)
Julian Date
r
i
g

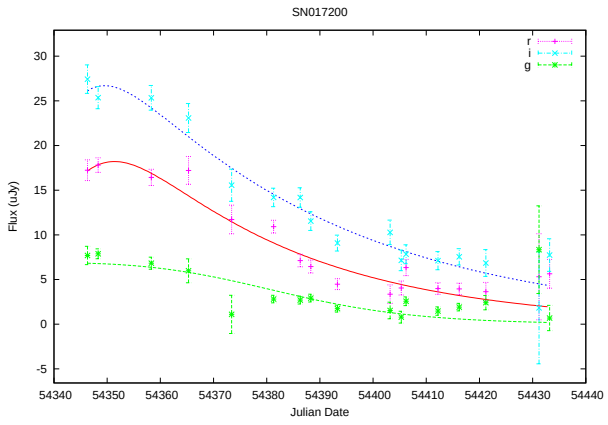
SN017200
r
i
g
Flux (uJy)
Julian Date

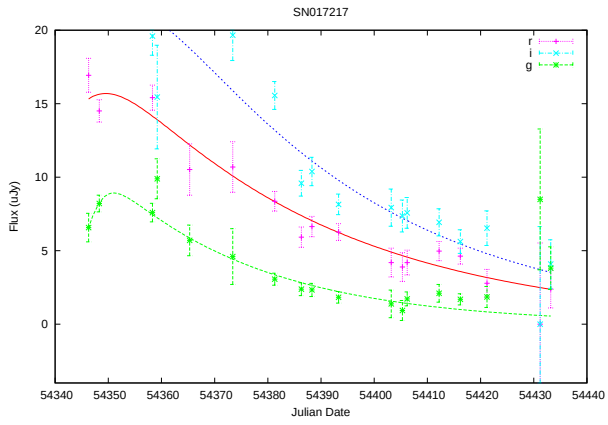
SN017217
r
i
g
Flux (uJy)
Julian Date

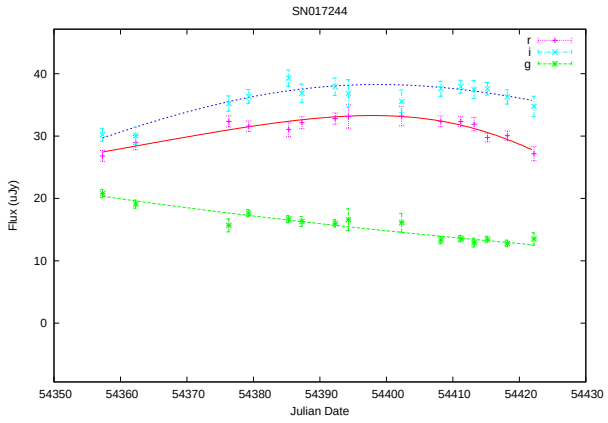
SN017244
r
i
g
Flux (uJy)
Julian Date

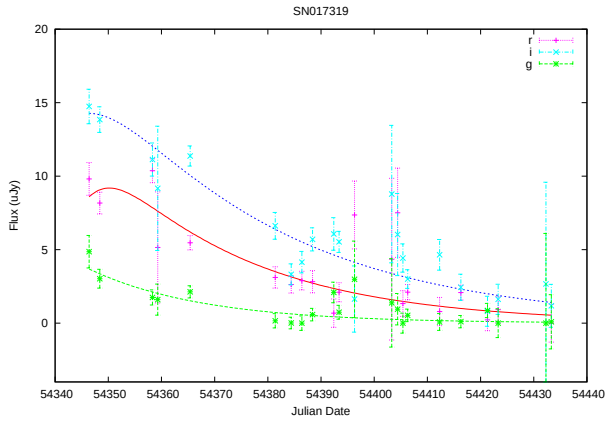
SN017319
r
i
g
Flux (uJy)
Julian Date

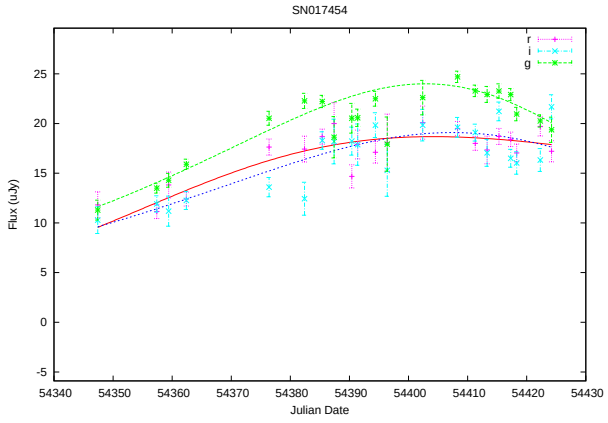
SN017454
r
i
g
Flux (uJy)
Julian Date

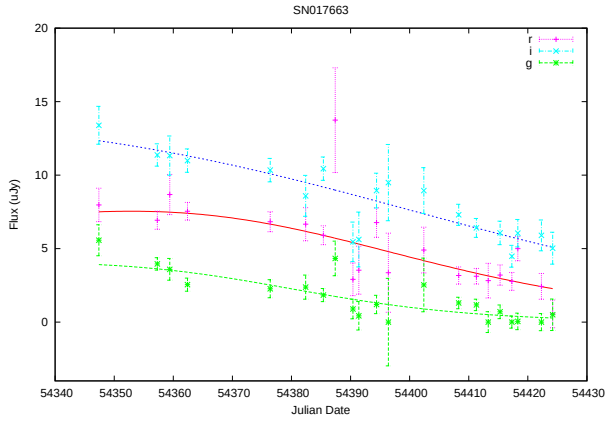
SN017663
r
i
g
Flux (uJy)
Julian Date

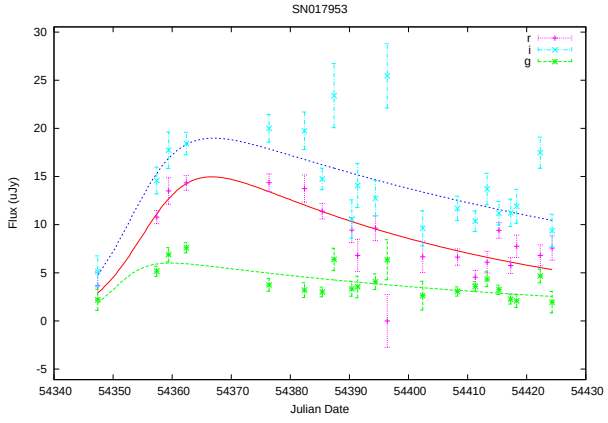
SN017953
r
i
g
Flux (uJy)
Julian Date

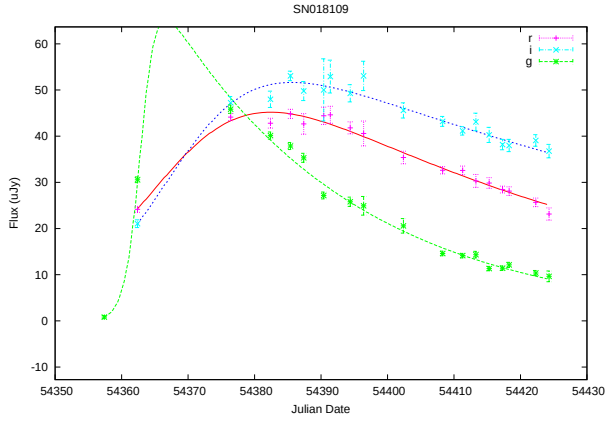
SN018109
r
i
g
Flux (uJy)
Julian Date

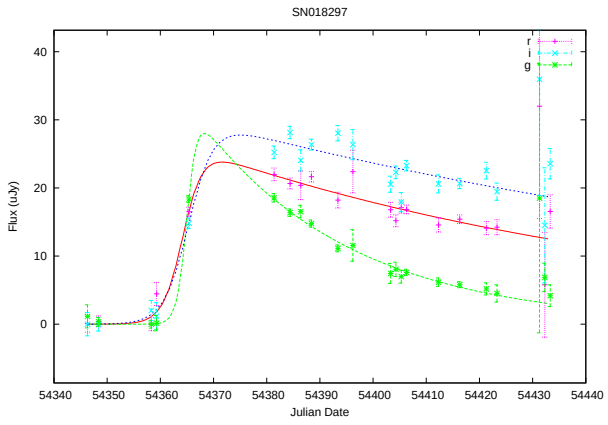
SN018297
r
i
g
Flux (uJy)
Julian Date

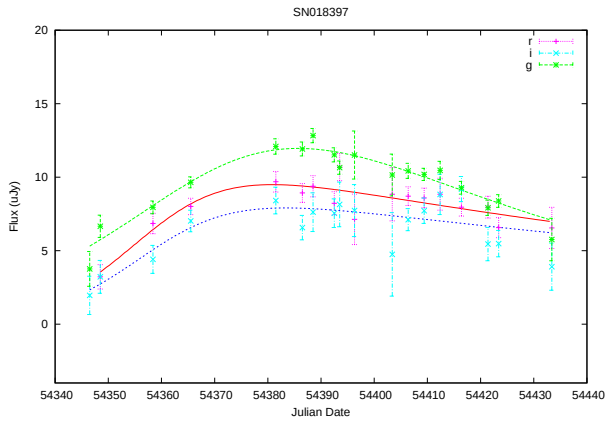
SN018397
r
i
g
Flux (uJy)
Julian Date

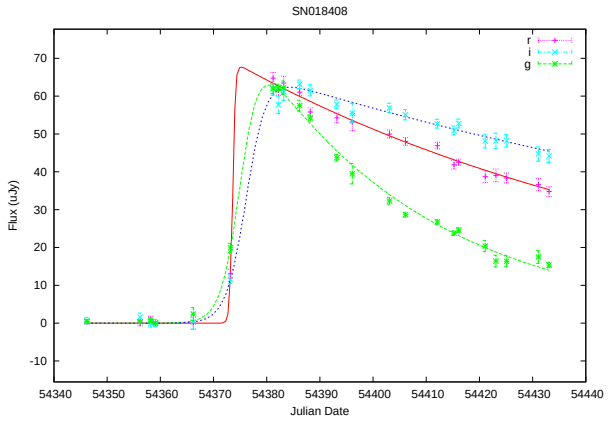
SN018408
r
i
g
Flux (uJy)
Julian Date

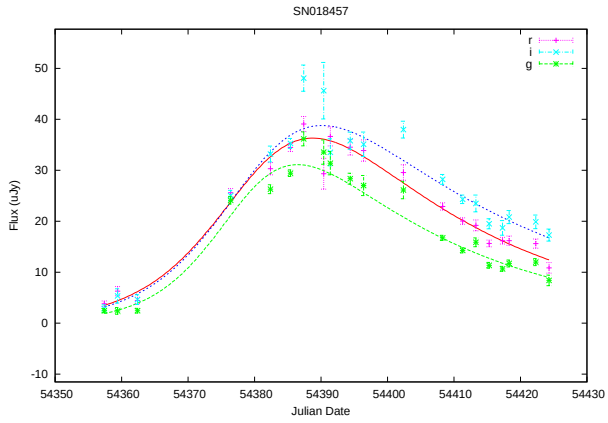
SN018457
r
i
g
Flux (uJy)
Julian Date

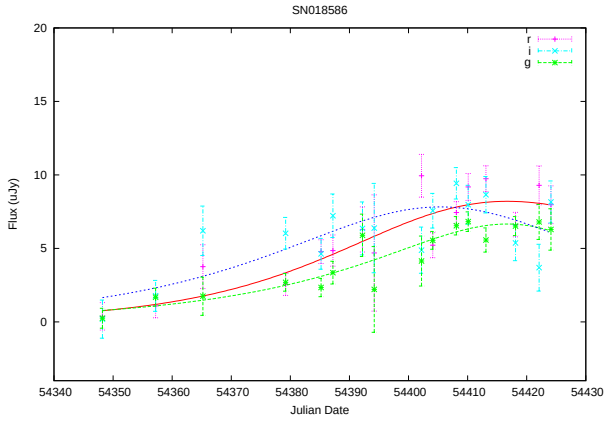
SN018586
r
i
g
Flux (uJy)
Julian Date

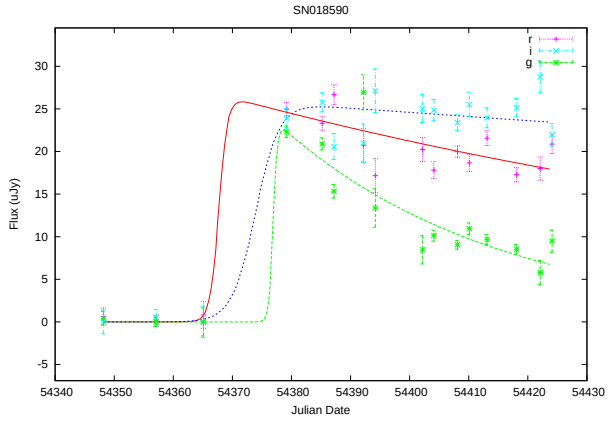
SN018590
r
i
g
Flux (uJy)
Julian Date

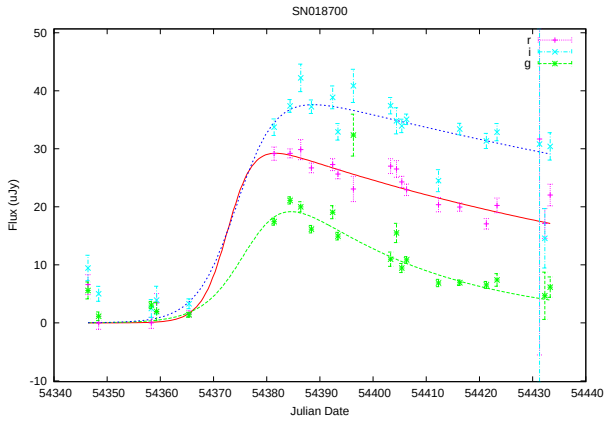
SN018700
r
i
g
Flux (uJy)
Julian Date

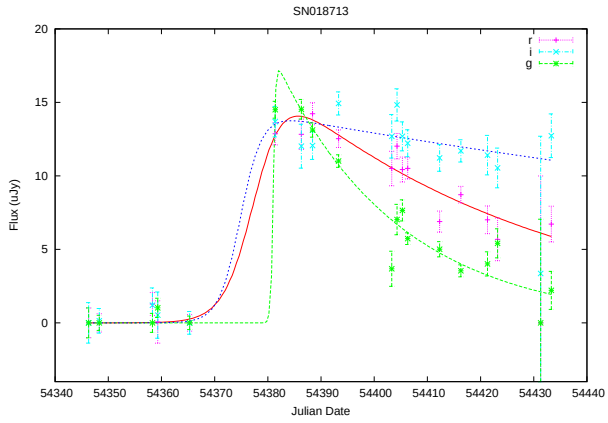
SN018713
r
i
g
Flux (uJy)
Julian Date

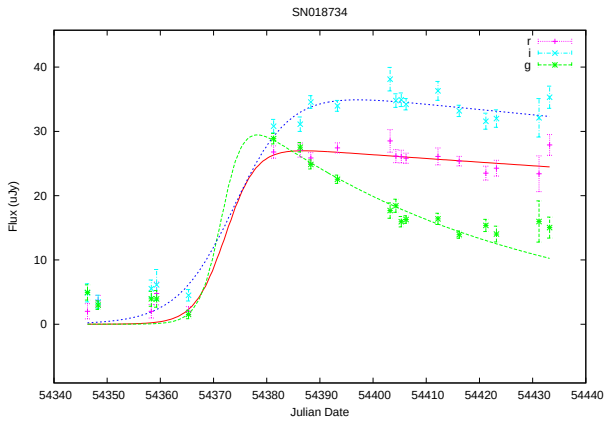
SN018734
r
i
g
Flux (uJy)
Julian Date

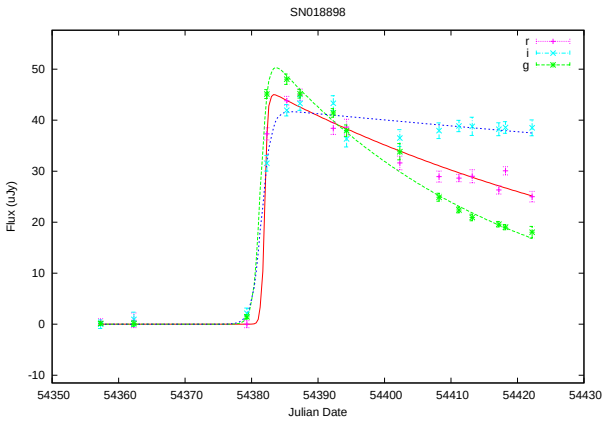
SN018898
r
i
g
Flux (uJy)
Julian Date

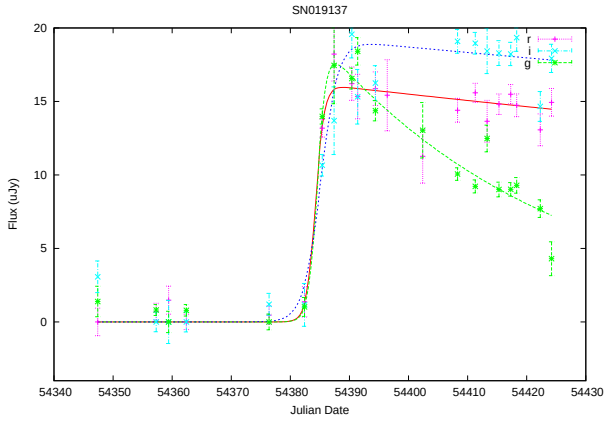
SN019137
r
i
g
Flux (uJy)
Julian Date

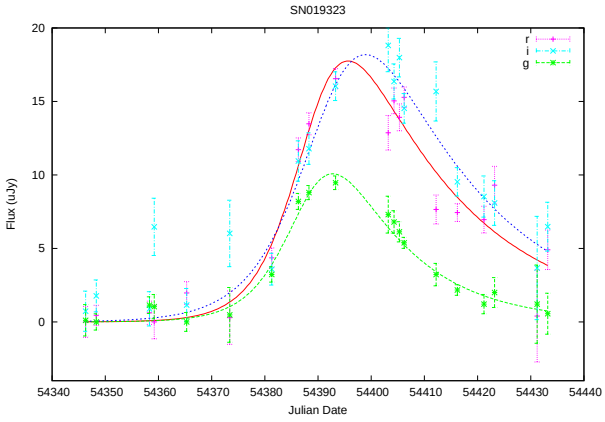
SN019323
r
i
g
Flux (uJy)
Julian Date

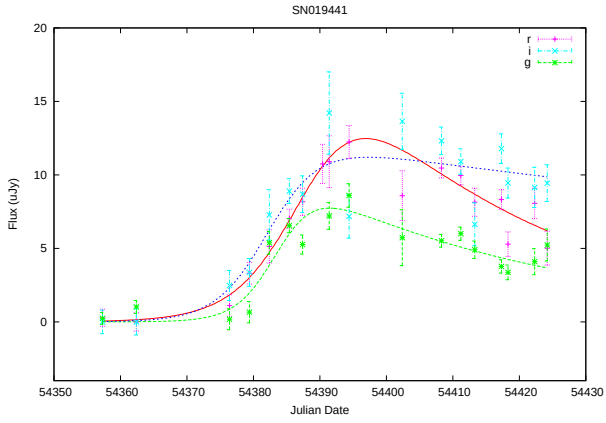
SN019441
r
i
g
Flux (uJy)
Julian Date

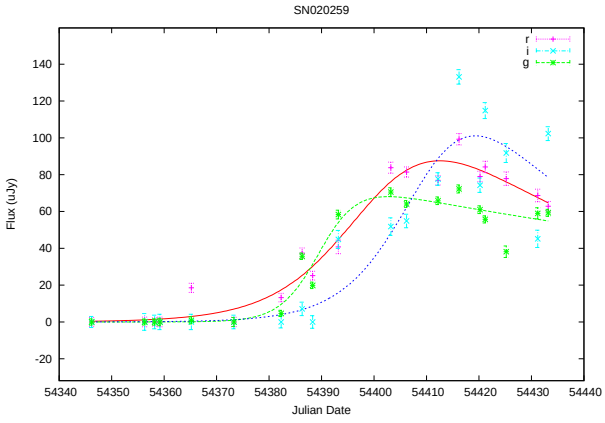
SN020259
r
i
g
Flux (uJy)
Julian Date

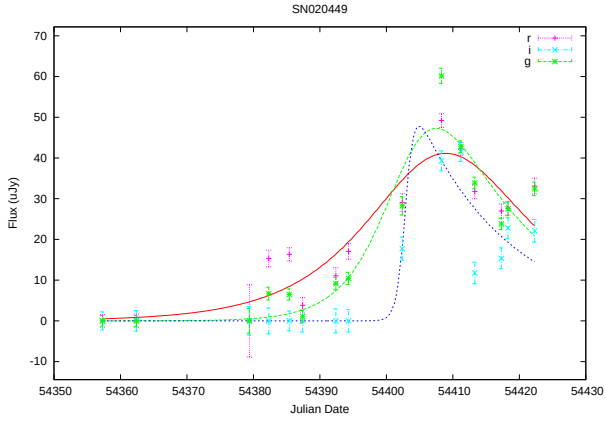
SN020449
r
i
g
Flux (uJy)
Julian Date

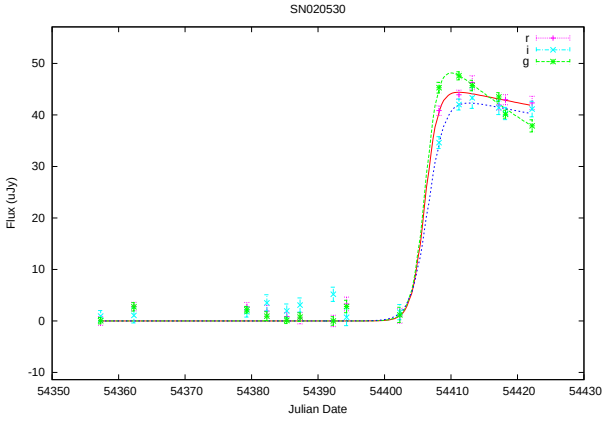
SN020530
r
i
g
Flux (uJy)
Julian Date

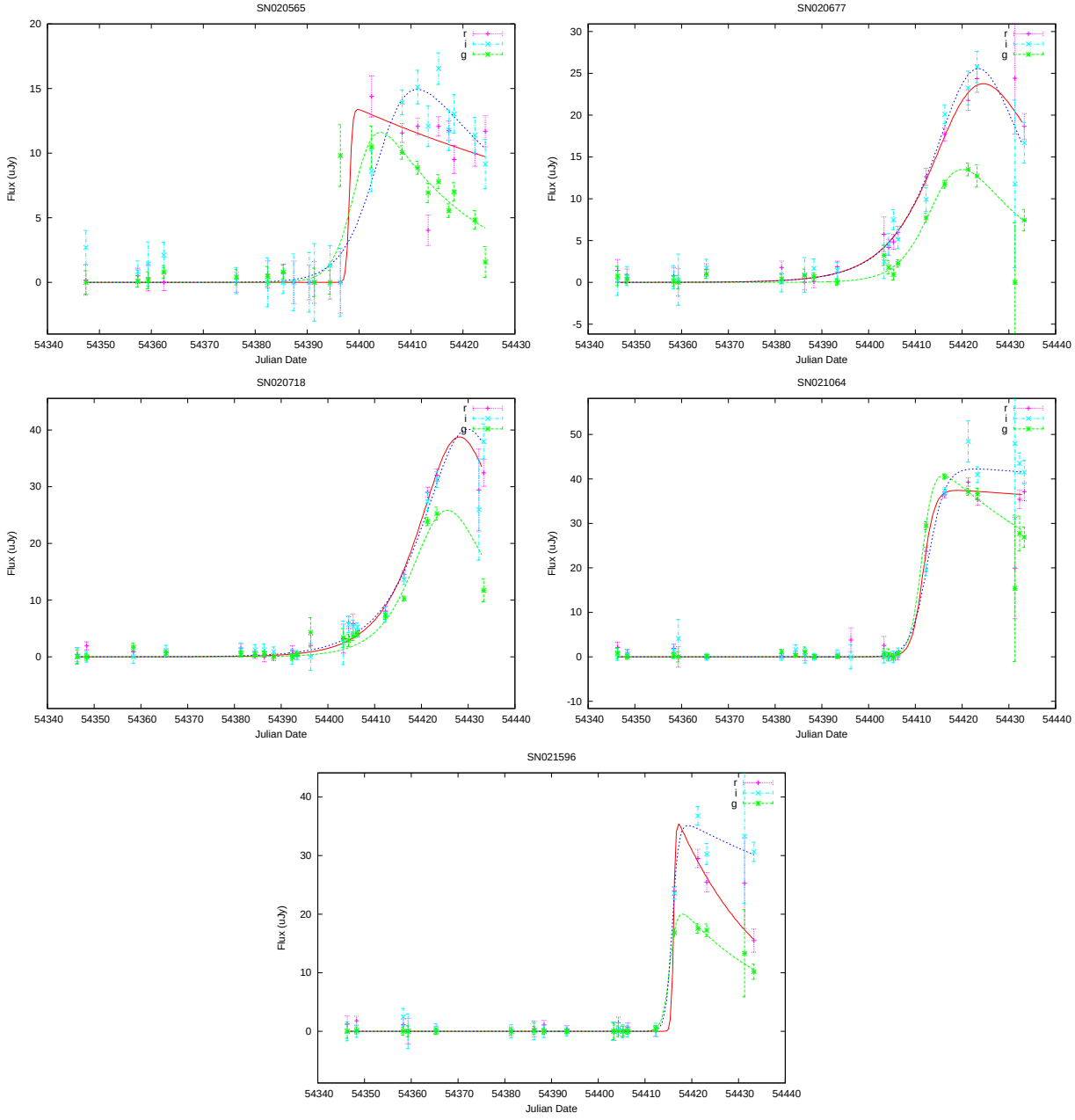
SN020565
SN020677
SN020718
SN021064
SN021596
Flux (uJy)
Julian Date
r
i
g

Appendix B: Rate Sample Candidates

SDSS-II SNID	IAUC ID	RA (deg.)	Decl. (deg.)	Redshift(z)	z Source	Peak JD
SN000768	-	20.4991	-1.04022	0.05431	Host	53629.5
SN001188	-	27.5684	0.950447	0.08474	Host	53627.9
SN001296	-	-25.3251	-1.23549	0.0501	Photo	53627.7
SN001470	-	28.5245	0.207874	0.0868	Host	53640.9
SN001514	-	43.2426	0.08581	0.04125	Host	53628.1
SN001632	-	-37.2741	-0.134036	0.0573	Host	53629.9
SN001903	-	-24.1141	-0.842701	0.08893	Host	53630.8
SN002537	-	50.9218	-0.285981	0.0871	Photo	53634.6
SN002615	-	11.8927	-1.08124	0.05542	Host	53647.2
SN002744	2005hm	-35.2474	-1.02747	0.034	SN	53646.8
SN002793	-	9.56027	0.210146	0.0444	Host	53632.9
SN002970	-	26.4898	0.465829	0.0841	Photo	53632.4
SN003757	-	-2.59897	0.431556	0.07037	Host	53645.9
SN003818	2005gi	13.9695	0.504816	0.0508	SN	53636.6
SN005039	-	-17.6739	-0.03859	0.08269	Host	53646.0
SN005920	-	24.5251	-0.357203	0.08067	Host	53652.4

SDSS-II SNID	IAUC ID	RA (deg.)	Decl. (deg.)	Redshift(z)	z Source	Peak JD
SN006244	-	10.2939	-0.967901	0.0794	Photo	53679.7
SN006465	-	46.991	-0.237424	0.08691	Host	53654.0
SN006484	-	-26.6716	0.540861	0.08741	Host	53639.5
SN007811	-	-10.0271	0.805692	0.0824	Host	53669.5
SN008196	-	-26.9572	-0.911606	0.08	Photo	53678.9
SN008569	-	28.1118	-0.171481	0.08105	Host	53676.6
SN009585	-	4.76316	0.116326	0.07256	Host	53689.9
SN010054	-	47.0405	-0.51126	0.07822	Host	53685.1
SN010777	-	17.016	-0.90612	0.06344	Host	53697.0
SN010907	2005lm	3.77034	0.355063	0.08466	Host	53691.7
SN010928	-	6.67709	-0.803935	0.08186	Host	53689.4
SN011233	-	20.0155	-0.080512	0.07924	Host	53694.2
SN011241	-	28.3116	-0.10561	0.08829	Host	53695.2
SN011532	-	19.8529	0.537479	0.04531	Host	53696.4
SN011549	-	22.3114	0.14229	0.07182	Host	53703.9
SN012842	2006ez	-36.5449	-1.01604	0.088	SN	53999.9
SN012844	2006fe	-46.9619	-0.511214	0.07	Host	53975.5
SN012896	-	3.27694	-0.138011	0.0733	Host	53996.5
SN012922	-	4.37816	0.758735	0.08926	Host	53991.2
SN013267	-	30.0201	1.03465	0.06048	Host	53997.6
SN013315	-	-15.6436	-0.55475	0.0542	Host	54003.0
SN013355	2006kh	27.2993	-0.605307	0.05969	SN	54056.0
SN013376	2006gq	26.3022	0.356372	0.06975	SN	53996.7
SN013449	2006ix	-0.19162	-0.311128	0.0757	SN	54019.2
SN013468	-	-4.95648	0.173536	0.06012	Host	53995.1
SN013722	-	-20.3901	0.498506	0.08652	Host	54029.9

SDSS-II SNID	IAUC ID	RA (deg.)	Decl. (deg.)	Redshift(z)	z Source	Peak JD
SN014030	-	-45.7695	0.0855	0.0867	Host	53999.5
SN014492	2006jo	20.8112	-0.329726	0.07673	SN	54014.9
SN015031	2006iw	-9.66895	0.259635	0.03073	SN	54013.0
SN015242	-	-3.24835	-0.447606	0.07107	Host	54036.7
SN015320	2006kv	0.777618	0.913684	0.0563	SN	54021.0
SN015358	-	-19.38	0.305077	0.08787	Host	54012.3
SN015391	-	-20.3755	-1.17099	0.08818	Host	54026.7
SN015413	-	-10.7738	0.624804	0.0871	Photo	54035.8
SN015757	-	6.40289	0.243167	0.0703	Photo	54048.0
SN015899	-	-3.24826	-0.447625	0.07107	Host	54035.2
SN016087	2006pc	26.044	-0.155957	0.05542	SN	54043.7
SN016089	-	32.1851	0.78705	0.0618	Host	54020.7
SN016179	2006nx	53.3776	-0.677397	0.05	SN	54055.7
SN016192	2006ny	9.82208	0.083836	0.07866	SN	54052.7
SN016200	-	-31.4566	1.23967	0.0893	Host	54051.7
SN016282	-	3.70538	-0.774936	0.08626	Host	54054.8
SN016556	-	23.4502	-0.679836	0.07874	Host	54057.7
SN016857	-	46.3985	0.625511	0.07532	SN	54067.2
SN017200	2007ja	-7.47723	0.725556	0.088	SN	54351.4
SN017217	-	-6.9122	-0.13945	0.06799	Host	54349.5
SN017244	2007ib	-11.0644	0.457032	0.034	SN	54397.9
SN017319	-	24.8948	-0.512923	0.05492	Host	54350.2
SN017454	-	24.9335	-0.714351	0.0631	Photo	54404.2
SN017663	-	24.0661	-0.788706	0.08448	Host	54352.9
SN017953	-	26.9352	1.01362	0.07894	Host	54366.7
SN018109	2007kw	32.57	-0.26597	0.069	SN	54382.4

SDSS-II SNID	IAUC ID	RA (deg.)	Decl. (deg.)	Redshift(z)	z Source	Peak JD
SN018297	2007ky	16.548	-0.614241	0.071	SN	54371.6
SN018397	-	53.9175	0.263178	0.0891	Photo	54380.9
SN018408	2007lj	-37.8253	-0.067404	0.04	SN	54375.2
SN018457	2007ll	29.6672	-0.249128	0.081	SN	54388.8
SN018586	-	-45.5802	-1.20825	0.0891	Photo	54416.7
SN018590	2007nw	-48.2027	-1.2573	0.0573	SN	54371.6
SN018700	2007md	20.4868	-1.01337	0.0546	SN	54381.7
SN018713	2007lz	7.84661	0.318809	0.088	SN	54385.7
SN018734	2007lx	2.91353	-0.473447	0.057	SN	54386.9
SN018898	-	3.27398	0.967083	0.0716	Host	54383.3
SN019137	-	23.4227	-0.653253	0.05536	Host	54388.9
SN019323	2007nc	0.288714	1.06835	0.0868	SN	54395.7
SN019441	-	15.8468	-1.10796	0.0895	Host	54396.9
SN020259	-	-23.853	-0.184517	0.05704	Host	54412.6
SN020449	-	9.69981	0.582582	0.08053	Host	54408.9
SN020530	-	0.917516	-0.280645	0.0613	Host	54411.2
SN020565	-	27.5966	-0.243436	0.08827	Host	54399.8
SN020677	2007qx	6.92398	1.23312	0.06	SN	54424.5
SN020718	2007rj	28.4952	-0.092745	0.08	SN	54428.2
SN021064	2007qb	14.8279	-0.947139	0.0792	SN	54419.0
SN021596	-	7.23027	-0.072207	0.069	Host	54417.2

BIBLIOGRAPHY

[1] G. Bazin *et al.*, Astronomy and Astrophysics **499**, 653 (2009).

[2] Paul Murdin and Lesley Murdin, *Supernovae*. Cambridge University Press (1985).

[3] Retrieved from `http://www.cfa.harvard.edu/iau/nova_list.html`, December 6, 2010.

[4] P. Filippenko *et al*, Annual Review of Astronomy and Astrophysics **36**, 309 (1997).

[5] L. Bildsten *et al.*, The Astrophysical Journal **662**, L95 (2007).

[6] Dina Prialnik, *An Introduction to the Theory of Stellar Structure and Evolution*. Cambridge University Press (2008).

[7] W.N. Cottingham and D.A. Greenwood, *An Introduction to Nuclear Physics*. Cambridge University Press (2004).

[8] Retrieved from `http://apod.nasa.gov/apod/ap051202.html`, December 6, 2010.

[9] A. Hewish and S.E. Okoye, Nature **207**, 59 (1965).

[10] W. Baade and F. Zwicky, The Physical Review **46**, 76 (1934).

[11] V. Trimble, Reviews of Modern Physics **54**, 1183 (1982).

[12] E. Cappellaro *et al.*, Astronomy and Astrophysics **351**, 459 (1999).

[13] T. Dahlen *et al.*, The Astrophysical Journal **613**, 189 (2004).

[14] F. Mannucci *et al.*, Astronomy and Astrophysics **433**, 807 (2005).

[15] M. Botticella *et al.*, Astronomy and Astrophysics **479**, 49 (2008).

[16] Retrieved from `http://www.sdss.org`, October 21, 2010.

[17] J. Gunn *et al.*, The Astronomical Journal **116**, 3040 (1998).

[18] D. York *et al.*, The Astrophysical Journal **120**, 1579 (2000).

[19] L. Girardi *et al.*, Astronomy and Astrophysics **391**, 195 (2002).

[20] J. Frieman *et al.*, The Astronomical Journal **135**, 338 (2008).

[21] R. Kessler *et al.*, The Astrophysical Journal Supplement Series **185**, 32 (2009).

[22] J. Guy *et al*, Astronomy and Astrophysics **466**, 11 (2007).

[23] B. Dilday *et al.*, The Astrophysical Journal **713**, 1026 (2010).

[24] D. Schlegel et al., *The Baryon Oscillation Spectroscopic Survey: Precision Measurements of the Absolute Cosmic Distance Scale*. White Paper for the Astro2010 CFP Science Frontier Panel (2009).

[25] B. Dilday *et al.*, The Astrophysical Journal **682**, 262 (2008).

[26] R. Lupton *et al*, ASP Conf. Ser. **238**, Astronomical Data Analysis Software and Systems (San Francisco:ASP), 269 (2001).

[27] G. Miknaitis *et al*, Bulletin of the American Astronomical Society **34**, 1205 (2002).

[28] B. Basset *et al*, *SDSS-II SN Super-unofficial Hand-Scanning Guide*, Retrieved from `http://sdssdp62.fnal.gov/sdsssn_data/sdsssn.html`, April 1, 2011.

[29] J. Holtzman *et al*, The Astronomical Journal **136**, 2306 (2008).

[30] Joachim Wuttke: lmfit - a C/C++ routine for Levenberg-Marquardt minimization with wrapper for least-squares curve fitting, based on work by B. S. Garbow, K. E. Hillstrom, J. J. Morand S. Moshier. Version 2.4, retrieved on 7/27/2008 from http://www.messen-und-deuten.de/lmfit/.

[31] M. Sako *et al*, The Astronomical Journal **135**, 348 (2008).

[32] C. Zheng *et al*, The Astronomical Journal **135**, 1766 (2008).

[33] S. Jha *et al*, The Astrophysical Journal **659**, 122 (2007).

[34] A. Connolly *et al*, The Astronomical Journal, **110**, 2665 (1995).

[35] L. da Costa *et al*, The Astrophysical Journal Letters **424**, L1 (1994).

[36] David W. Hogg, arXiv:9905116 [astro-ph] (2000).

[37] M. Vardanyan, *iCosmos Cosmology Calculator*, Retrieved from `http://www.icosmos.co.uk`, April 10, 2011.

[38] J. Cardelli *et al*, The Astrophysical Journal **345**, 245 (1989).

[39] K. Hatano *et al*, The Astrophysical Journal **502**, 177 (1998).

[40] Shunsaku Horiuchi *et al*, arXiv:1102.1977 [astro-ph] (2011).

[41] I. Baldry *et al*, Monthly Notices of the Royal Astronomical Society **358**, 441 (2005).

[42] R. Nave, *Stellar Lifetime Calculator*, Retrieved from `http://hyperphysics.phy-astr.gsu.edu/hbase/astro/startime.html`, May 1, 2011.

[43] J. Anthony, *Large Synoptic Survey Telescope - Overview*, Proceedings of SPIE **4836**, 10 (2002).

ABSTRACT

THE CORE COLLAPSE SUPERNOVA RATE IN THE SDSS-II SUPERNOVA SURVEY

by

MATTHEW F. TAYLOR

August 2011

Advisor: Professor David Cinabro

Major: Physics

Degree: Doctor of Philosophy

The Sloan Digital Sky Survey II Supernova Survey (SDSS-II SN), though designed as a type Ia supernova search for cosmology, also discovered a large sample of core collapse supernovae (CCSN). I use the SDSS-II SN data to measure the volumetric CCSN rate in the redshift range ($0.03 < z < 0.09$), finding a volume-averaged rate of $0.98 \pm 0.18 \times 10^{-4} \mathrm{yr}^{-1} (h_{70}^{-1} \mathrm{Mpc})^{-3}$. The CCSN luminosity function is also extracted from the data, and its implications on the cosmic star formation history are considered.

Autobiographical Statement

Name: Matthew F. Taylor

Education:
M.S. Applied Physics, Rice University, Houston, Texas, 2001
B.S. Computer Science, University of Michigan, Ann Arbor, Michigan, 1989
Professional Experience:
Software Engineer, Cray Inc., Mendota Heights, Minnesota, 2003-2005
Software Engineer, Hewlett-Packard, Houston, Texas, 2001-2003
Software Engineer, Lucent Technologies, Naperville, Illinois, 1989-1997
Publications:
"SNANA: A Public Software Package for Supernova Analysis," Publications of the Astronomical Society of the Pacific v. 121, p. 1028 (2009)
"Electron Tunneling Rates between an Atom and a Corrugated Surface," Physical Review B v. 64, p. 115422 (2001)

From a very young age I have always had a strong interest in mathematics in science. Like many people with similar interests, I was initially drawn to the field of information technology, which was relatively new in the late 1980's when I began my career. After completing my Bachelor's in computer science, I worked for several years as a software engineer for ATT (later called Lucent Technologies) in the Chicago area.

While software development is a rewarding and interesting pursuit, I came to realize that I have an especially deep interest in the physical sciences and that a deeper study of physics in particular is an essential life goal for me. Therefore, I eventually left the software developmebt field and enrolled in a graduate Applied Physics program at Rice University, in Houston, Texas. At Rice, I concentrated on the study of quantum mechanics, atomic and molecular physics, and condensed matter physics. After completing my Master's at Rice, I returned to the private sector as a software developer once again.

A few more years of work passed, this time for Compaq in Houston, Texas (now a division of Hewlett-Packard), and then for Cray Inc. in Minnesota. Though my work in information technology was interesting and rewarding, as always, I again found myself drawn to gain a deeper understanding of physics. This time I was most interested in studying topics within physics that I had only lightly touched on at Rice, namely nuclear physics, elementary particles, astrophysics and cosmology. I therefore applied to the WSU PhD physics program. At WSU, I participated in theoretical nuclear physics research with Prof. Sean Gavin., and then astrophysics and cosmology with Prof Cinabro.

Working here at WSU, I have also discovered an unexpected interest in and aptitude for education. I have found it especially rewarding to help students who find math and science difficult learn about these topics, in spite of their initial aversion and confusion. Perhaps this will lead me toward a new career path in education. I have certainly enjoyed learning about every aspect of physics throughout my studies; it would be rewarding to share that knowledge and the enjoyment of it with future students.